University of Ottawa

Real space perspective on High Harmonic Generation in Solids

GUILMOT ERNOTTE
Faculty of Science
Department of Physics

Thesis submitted to the University of Ottawa in partial fulfillment for a
Doctorate in Philosophy
degree in Physics

March 2025

ABSTRACT

High harmonic generation in solids is a burgeoning field that employs strong and ultrashort electric fields to explore electronic dynamics. While existing models have successfully explained generation mechanisms in solids, they have predominantly focused on momentum space. To enhance our comprehension of matter and facilitate the development of faster signal processing devices, this thesis introduces a position model utilizing Wannier states. Firstly, I meticulously define parameters, including the separation of interband and intraband currents in various electric field gauges. Secondly, I transform the existing models, formulated in a Bloch basis (momentum space), into a Wannier basis, unveiling dynamics in position space. Utilizing this model in a strong field approximation, I uncover novel paths contributing to interband harmonic spectra, incorporating a distinct position component. This leads to the development of a quantitatively predictive semiclassical model. Lastly, I present experimental works where a position space perspective is crucial to elucidate observed results, spanning from 2D materials to nanoantennas.

RÉSUMÉ

La génération d'harmoniques élevés dans les solides est un domaine d'étude dans lequel des champs électriques forts et ultracourts sont utilisés pour sonder la dynamique électronique. Des modèles récents expliquent le mécanisme de génération dans les solides et partagent des similitudes avec l'état gazeux. Cependant, ces modèles ont été pour la plupart limités à l'espace de quantité de mouvement. Un modèle basé sur l'espace position est nécessaire pour approfondir notre compréhension de la matière et pour aider à concevoir de nouveaux dispositifs améliorant la vitesse de traitement de signal. Dans cette thèse, je développe un tel modèle en utilisant les états de Wannier. Tout d'abord, je définis rigoureusement tous les paramètres, y compris la séparation des courants interbandes et intrabandes dans toutes les jauges de champ électrique. Deuxièmement, à partir des modèles actuels qui sont écrits dans une base de Bloch, je les transforme en une base d'état de Wannier. Celle-ci révèle la dynamique de l'espace de position. J'ai ensuite utilisé ce modèle dans une approximation de champ fort pour révéler de nouvelles trajectoires qui contribuent au spectre d'harmoniques interbandes. Ces nouvelles trajectoires ont toutes une nouvelle composante de position dans leur nature. Cela conduit à la formulation d'un modèle semi-classique quantitativement prédictif. Enfin, je montre des travaux expérimentaux où une perspective spatiale est nécessaire pour expliquer les résultats observés. L'une est dans un matériau 2D et l'autre est avec des nano-antennes.

ACKNOWLEDGEMENTS

In the end only my name appears on this thesis, but it would be a lie to say that I am the only behind this work. Science is mostly a collaborative type of endeavour. Some people contributed directly to the development of this thesis and others in indirect, yet important, ways.

I want to begin by expressing my gratitude to my supervisor, Paul Corkum, whose unwavering support has been invaluable throughout this journey. Despite the unexpected shift towards theory in my research, Paul consistently encouraged my pursuit of whichever ideas intrigued me at the time. His group provided an environment of independence, allowing me to carve my own path and dedicate time to enhancing my theoretical skills. Special thanks to Thomas Brabec for his significant contribution to the theoretical work presented in this thesis, guiding me through the application of the strong field approximation to my model. Lastly but certainly not least, I must acknowledge Andre Staudte for his moral support and willingness to lend an ear even when the material was undigestable.

A heartfelt thank you to Marco Taucer, a close collaborator throughout my thesis, who, coming from an engineering background, taught me how to think like a physicist and navigate experimental work in the labs. Gratitude also extends to Zack for providing support beyond the lab, helping me maintain a balanced perspective, whether online or over a

board game. I'd like to recognize my other colleagues with whom I've shared the lab and who patiently listened during my presentations: Aleksey, Kyle, Tian, Chandler, David (bis), TJ, Giulio, Graham, and Shima.

Deepest appreciation goes to Irina, my wife, for standing by me throughout this long and challenging journey. Your unwavering belief in me, even during moments of doubt, and your constant support made you my number one advocate. You were always supportive even when my schedule kept me far from you and locked me in the lab late a night. Finally, special thanks to my family, who witnessed and supported me throughout the longest journey, my life.

TABLE OF CONTENTS

LIST OF FIGURES

LIST OF SYMBOLS AND ACRONYMS

HHG	High Harmonic Generation
TDSE	Time Dependent Schrödinger Equation
MLWF	Maximally Localized Wannier Function
WQC	Wannier Quasi-Classical
SFA	Strong Field Approximation
FBZ	First Brillouin Zone

LIST OF APPENDICES

Part I

INTRODUCTION

CHAPTER 1 Introduction

The plurality of views is becoming more and more important in all organizations nowadays [1]. The notion of understanding an object or a situation from just a singular perspective seems limiting and incomplete. Embracing the importance of multiple perspectives is akin to unlocking a treasure trove of knowledge, enriching our comprehension.

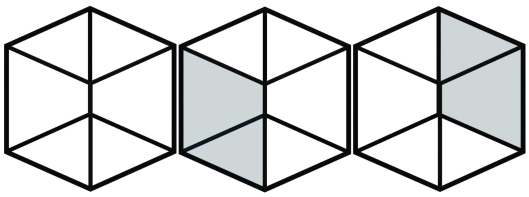

Figure 1.1 The Necker cube is an optical illusion where two orientations of the cube are valid.

The Necker cube, a visual riddle, exemplifies the significance of exploring multiple perspectives. This deceptively simple geometric construct challenges us to witness the paradoxical nature of perception. As we gaze upon the Necker cube, it defies being neatly pigeonholed into a single orientation. Instead, it oscillates between two possible interpreta-

tions, both of which are valid.

Perhaps surprisingly, the significance of adopting multiple perspectives is not confined to the realms of everyday life; it extends even to the abstract realms of theoretical physics. Physicists grapple with intricate puzzles that demand an intricate web of perspectives to be fully comprehended. To make progress in the quest for fundamental truths, they must be willing to explore multiple perspectives. By embracing various theoretical frameworks, mathematical approaches, and even contemplating seemingly contradictory interpretations, they engage in a collective dance of ideas. Just as the Necker cube oscillates between two perspectives, so too does the theoretical physicist shift their focus between different paradigms, revealing diverse facets of reality.

One aspect of our reality is the ultrafast timescale of electron motion compared to ours, making it difficult to grasp and understand. The femtosecond laser is a tool that has allowed us to bridge that gap. One of its Nobel Prize achievements was to reveal these ultrafast motions and record the equivalent of a movie for a chemical reaction [2]. Nowadays, femtosecond lasers are routinely used to probe ultrafast phenomena [3–6]. When these femtosecond lasers are also very intense, they can rival the inner forces keeping the electron bonded to its nucleus, analogous to a hammer delivering a lot of energy just to the tip of a nail for a very brief moment. One signature of this type of interaction is the generation of high-energy photons, a process we call High Harmonic Generation (HHG) [7–10].

Usually, HHG experiments were performed on atomic or molecular gas targets [7–9,11]. They were successful in probing the sub-cycle charge dynamics [11–14] as well as performing a tomography of the electron orbital wavefunction [15]. Recently, the field has been extended to solid targets [16], opening a new realm of possibilities that were not achievable with gas targets [5, 6, 17–24].

The mechanism explaining HHG in atomic gas could not be readily transferred to the solid state. A different approach was necessary to explain this new process in order to fully grasp its nature and understand how much control we could exert over it. Surprisingly, the emerging models had strong similarities with the gas phase [25–31], but they are still incomplete. Namely, they explain what the electrons do in what is called momentum space, but they lack an explanation for position space. Just like with the Necker cube, it is important to be able to oscillate from one perspective to the other. The understanding of HHG in solids can only be complete if we can readily switch between momentum and position space. Some problems are more easily tackled from the momentum space, but others, like nanoantennas [32–34], heterostructures [35], and impurities [36, 37], are best explored with a position space perspective.

This thesis will attempt to develop this real-space perspective for HHG in solids by first revisiting how HHG can be explained in gases. Then, it will revisit the nature of crystals and solids to finally explain our current models for HHG in solids, which are in momentum space. An important point will arise in the decomposition of the currents responsi-

ble for HHG and I will rigorously define this decomposition. Following this point, I will introduce the Wannier states from which I will build a real-space perspective. This new perspective will lead to the formulation of a semi-classical model capable of explaining HHG in solids quantitatively. I will then present experiments where a real-space perspective is necessary.

In this thesis, Hartree atomic units (i.e. $\hbar = m_e = e = 1$) are used throughout, unless otherwise stated.

Part II

THEORETICAL BACKGROUND

CHAPTER 2 Introduction to High Harmonic Generation in Gas

When a laser interacts with an atom, an electron might be pulled out of the atom. The probability of this event increases with the laser frequency ω_0, as described by the photoelectric effect [38] and multi-photon absorption [39, 40]. However, even at frequencies much smaller than the Ionization Potential (IP) of the atom, a laser can ionize an atom if the laser's electric field is comparable to the atomic Coulomb force. The electron can tunnel ionize out of its Coulomb barrier. These two mechanisms of ionization, multi-photon absorption and tunneling, are both described by the Keldysh parameter, γ [41]:

$$\gamma = \frac{\omega_0 t_{\text{tun}}}{2\pi} \propto \sqrt{\frac{I_p}{2U_p}}, \tag{2.1}$$

where t_{tun} is the imaginary time required for the electron to tunnel, ω_0 is the radial frequency, and U_p is the ponderomotive energy, the cycle-average energy of a free electron in the electric field. The Keldysh parameter gives an idea of which regime the interaction is in; if $\gamma \gg 1$, the tunneling time is greater than the optical period, and therefore the ionization is described by multi-photon absorption. Conversely, if $\gamma \ll 1$, the electron is in the tunneling regime. Most of this thesis will assume that we are in the tunneling regime unless stated otherwise.

The tunneling of the electron is only the first step. Once it is free from its parent ion, the electron gets accelerated by the electric field of the laser. Eventually, when the fields switch polarity, the electron is brought back into the vicinity of its parent ion, where it might recombine, releasing its kinetic energy as a high-energy photon. This is the classical or simple model of High Harmonic Generation (HHG) in atomic gas [10], depicted in Fig. 2.1.

A straightforward mathematical derivation of this model is presented in Appendix A. I would like to highlight three important results from this derivation. First, the process is symmetric for every half-cycle of the laser; the electrons are just accelerated in the opposite direction, leading to the emission of only odd harmonics of the driving laser frequency if the laser is multi-cycles. Second, for the different electrons ionized within one half-cycle, two classes of trajectories exist: short and long, which lead to the same emitted energy. In a typical experiment, the laser will ionize more than one atom, and due to phase-matching conditions and different divergence conditions for these two classes of trajectories, the short trajectories constitute the majority of the collected signal. Third, there is a delay between the emission of different harmonics, a chirp that we call attochirp.

This description so far has been purely classical, assuming that an electron can indeed break free from its parent ion's Coulomb barrier. It is possible to use a quantum framework and recover these three steps. We start by describing the electron in its ground state as $|g\rangle$, an eigenstate

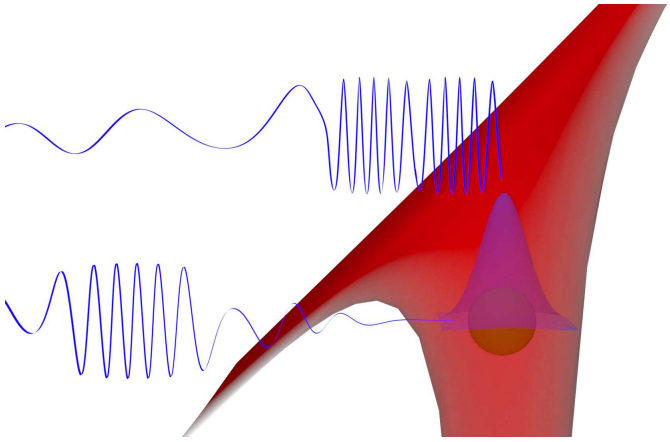

Figure 2.1 Under an intense electric field, an electron (blue) can escape the Coulomb barrier (red) of its parent ion (green). This electron is then accelerated and may recombine with its parent ion, emitting a high-energy photon.

of the atom Hamiltonian $\hat{H}_0 = \hat{p}^2/2 + V_0(\hat{x})$, where $\hat{p}$ and $\hat{x}$ are the momentum and position operators, respectively. This ground state energy will be -IP. Then, we write the full Hamiltonian with the interacting laser field $\hat{H}$ as follows:

$$\hat{H} = \frac{1}{2}\left[\hat{p} + A(t)\right]^2 + V_0(\hat{x}) - \Phi_F(\hat{x}, t), \tag{2.2}$$

where $\Phi_F(\hat{x}, t)$ and $A(t)$ are the scalar and vector potentials of the field $F(\hat{x}, t) = -\nabla\Phi_F(\hat{x}, t) - \partial A(t)/\partial t$. The length gauge is assumed for the field in the Hamiltonian: $\Phi_F(\hat{x}, t) = -F(\hat{x}, t)\cdot\hat{x}$ and $A(t) = 0$. The dipole approximation is also used, neglecting the electric field dependence on x and the effect of the magnetic field of the laser [42].

Next, we use Volkov states to describe continuum states $|\hat{p} + A(t)\rangle$,

with their energy being the kinetic energy of the electron: $\frac{1}{2}\left[\hat{p} + A(t)\right]^2$ [43]. These states cannot couple to one another under the electric field. With the ground state, they form a complete basis, and we can write the electron's total wavefunction $|\Psi(t)\rangle$ as a superposition of the ground state and all Volkov states:

$$\begin{aligned} |\Psi(t)\rangle =& b(t)\,|g\rangle \exp\left(i\int_{-\infty}^{t} dt'\,\mathrm{IP}\right) \\ &+ \int dp\, a_p(t)\,|p + A(t)\rangle \exp\left(-\frac{i}{2}\int_{-\infty}^{t} dt'(p + A(t'))^2\right), \end{aligned} \tag{2.3}$$

where the amplitudes $b(t)$ and $a_p(t)$ represent the ground state and Volkov states, respectively. Initially, only the ground state is populated, with $b(0) = 1$ and $a_p(0) = 0$.

Using the Time-Dependent Schrödinger Equation (TDSE), we can find how these amplitude coefficients evolve:

$$i\frac{\partial}{\partial t}\,|\Psi(t)\rangle = \hat{H}\,|\Psi(t)\rangle\,. \tag{2.4}$$

We assume that the laser will only ionize a small fraction of the ground state, making $\dot{b}(t) \approx 0$. This allows for an analytical solution for $a_p(t)$:

$$a_p(t) = \int_{-\infty}^{t} dt'\, F(t') d(p + A(t')) \exp\left[\int_{-\infty}^{t'} dt''\, \mathrm{IP} + \frac{(p + A(t''))^2}{2}\right]. \quad (2.5)$$

Then, we are interested in the field emitted by a recombining electron. According to Maxwell's laws, the acceleration of an electric dipole emits light. Therefore, we calculate the dipole between one Volkov state and the ground state:

$$\begin{aligned} D_p(t) =& - \langle \Psi(t) | g \rangle \langle g | \hat{x} | p + A(t) \rangle \langle p + A(t) | \Psi(t) \rangle + \text{c.c.} \\ =& b^*(t) d^*(p + A(t)) a_p(t) + \text{c.c.} \\ =& d^*(p + A(t)) \int_{-\infty}^{t} dt'\, F(t') d(p + A(t')) \\ & \times \exp\left[\int_{-\infty}^{t'} dt''\, \mathrm{IP} + \frac{(p + A(t''))^2}{2}\right] + \text{c.c.}, \end{aligned} \quad (2.6)$$

All that remains is to consider all the Volkov states and Fourier transform the total accelerated dipole to obtain a spectrum S of the emitted photons from recombination:

$$\begin{aligned} S(\omega) =& - \omega^2 \int_{-\infty}^{\infty} dt\, \mathrm{e}^{\,i\omega t} \int dp D_p(t) \\ =& - \omega^2 \int_{-\infty}^{\infty} dt \int dp\, d^*(p + A(t)) \\ & \times \int_{-\infty}^{t} dt'\, F(t') d(p + A(t')) \mathrm{e}^{-i\phi(p,t',t)} + \text{c.c.}, \end{aligned} \quad (2.7)$$

with

$$\phi(p, t', t) = -\omega t + \int_{t'}^{t} dt'' \, \mathrm{IP} + (p + A(t''))^2/2. \tag{2.8}$$

Solving these integrals analytically might seem like a lost cause, but we can use a mathematical tool called the saddle point approximation. This tool is detailed in Appendix B. It allows us to evaluate integrals when they have a fast oscillating phase, which is the case for Eq. 2.7. The approximation allows the integral to be approximated by evaluating the integrand at specific points called saddle points.

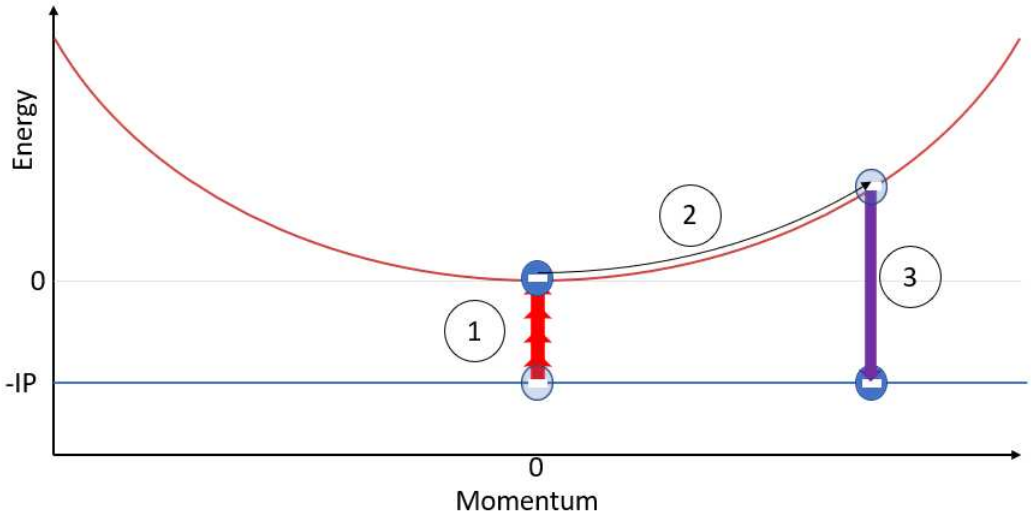

Figure 2.2 Energy vs momentum for HHG in gas. The electron (blue circle) is first tunnel ionized from its ground state (blue line) to the continuum (red parabola) thanks to the intense infrared laser (red arrows). Then it's accelerated by the laser field (black arrow) before recombining and emitting a high-energy photon (purple arrow).

After finding these saddle points, one can determine the amplitude

of the spectrum and obtain a good approximation for the process of HHG. This model, known as the Lewenstein model, provides a rigorous mathematical framework that aligns with the intuitive 3-steps model [44]. It has been successfully applied to a variety of atomic gas and molecular systems [45–47]. More recently, it has also been adapted to semiconductors and will be the topic of the next chapter.

CHAPTER 3 Introduction to High Harmonic Generation in solids

In late 2010, the first reported HHG experiment in solids was published [16]. Unlike the atomic gas phase, which predicts a maximum emitted energy that scales based on the square of the electric field strength, the maximum emitted energy from solids scaled linearly. This observation suggested that the generating mechanism in solids was fundamentally different from that in atomic gases. The authors hypothesized that this discrepancy was due to the non-parabolic nature of the crystal energy structure, which is distinct from the continuum states. To gain deeper insights on these hypotheses, let us reexamine the energy structure of a solid and the emergence of energy bands.

3.1 Crystals and Energy Bands

Crystals are typically modeled as infinitely large periodic potentials $V(\mathbf{x}) = V(\mathbf{x}+\mathbf{a_0})$, where $\mathbf{a_0}$ represents the periodicity of the crystal. This potential can also be described in momentum space through a simple Fourier Transform. The momentum potential will also exhibit periodicity in this conjugate space by a vector $\mathbf{G}$. In a 1D system, $G = 2\pi/a_0$. The eigenstates of this crystal Hamiltonian $\hat{H}_0$ are known as Bloch states $|\phi_{n,\mathbf{k}}\rangle$, and their corresponding eigenvalues are denoted as $E_n(\mathbf{k})$ [48]. These Bloch states are characterized by two quantum numbers: n (the band

index) and $\mathbf{k}$ (the crystal momentum). In position space, Bloch states are expressed as follows:

$$|\phi_{n,\mathbf{k}}\rangle = u_{n,\mathbf{k}}(\mathbf{x})\mathrm{e}^{i\mathbf{k}\cdot\mathbf{x}}, \tag{3.1}$$

where $u_{n,\mathbf{k}}(\mathbf{x}) = u_{n,\mathbf{k}}(\mathbf{x}+\mathbf{a_0})$ is referred to as the periodic part of the Bloch state. Notably, the Hamiltonian can be reformulated as a $\mathbf{k}$-dependent operator acting solely on the periodic part of the Bloch state:

$$\hat{H}_{\mathbf{k}}\,|u_{n,\mathbf{k}}(\mathbf{x})\rangle = \left[\frac{1}{2}\left(\hat{\mathbf{p}}+\mathbf{k}\right)^2 + V(\mathbf{x})\right]|u_{n,\mathbf{k}}(\mathbf{x})\rangle = E_n(\mathbf{k})\,|u_{n,\mathbf{k}}\rangle\,(\mathbf{x}). \tag{3.2}$$

When examining the crystal momentum $\mathbf{k}$ from Eq. 3.1, it appears strikingly similar to the conventional momentum of a plane wave ($\mathbf{p} = \hbar\mathbf{k}$). However, we can readily discern a distinction in Eq. 3.2, where the effective canonical momentum is given by $\hat{\mathbf{p}} + \mathbf{k}$. To substantiate this point, let us compute the expected value of the momentum operator for a Bloch state:

$$\langle\phi_{n,\mathbf{k}}|\,\hat{\mathbf{p}}\,|\phi_{n,\mathbf{k}}\rangle = \langle u_{n,\mathbf{k}}(\mathbf{x})|\,\hat{\mathbf{p}}\,|u_{n,\mathbf{k}}(\mathbf{x})\rangle + \mathbf{k}. \tag{3.3}$$

Hence, the momentum of an electron in band n with crystal momentum $\mathbf{k}$ encompasses not only its crystal momentum but also the contribution from the momentum operator acting on the periodic part of the Bloch state. A more insightful form of Eq. 3.3 can be obtained by differentiat-

ing Eq. 3.2 with respect to $\mathbf{k}$ and then multiplying by $\langle u_{n,\mathbf{k}}(\mathbf{x})|$:

$$\langle u_{n,\mathbf{k}}| \left(\hat{\mathbf{p}} + \mathbf{k}\right) + \hat{H}_{\mathbf{k}} \nabla_{\mathbf{k}} \left|u_{n,\mathbf{k}}\right\rangle = \langle u_{n,\mathbf{k}}| \nabla_{\mathbf{k}} E_n(\mathbf{k}) + E_n(\mathbf{k}) \nabla_{\mathbf{k}} \left|u_{n,\mathbf{k}}\right\rangle ; \quad (3.4)$$

$$\langle \phi_{n,\mathbf{k}}| \hat{\mathbf{p}} \left|\phi_{n,\mathbf{k}}\right\rangle = \langle u_{n,\mathbf{k}}(\mathbf{x})| \hat{\mathbf{p}} + \mathbf{k} \left|u_{n,\mathbf{k}}(\mathbf{x})\right\rangle = \nabla_{\mathbf{k}} E_n(\mathbf{k}). \quad (3.5)$$

As the expected value of momentum is linked to the expected velocity through the Ehrenfest's theorem [49], Eq. 3.5 demonstrates that the velocity of an electron in band n with crystal momentum $\mathbf{k}$ is equal to the derivative of the band energy with respect to $\mathbf{k}$.

If $\mathbf{k}$ is not an eigenvalue of the momentum operator, can we expect it to be a conserved quantity of motion? Noether's theorem informs us that whenever a symmetry exists, there is a corresponding conserved quantity [50]. The conservation of momentum, for instance, arises from the symmetry under translations, meaning that the physical laws remain unchanged regardless of the shift in position. However, within a crystal, the continuous translation symmetry is lost, replaced by a discrete one. As a result, we should anticipate a novel conserved quantity that arises discretely, reflecting the fact that an electron should not distinguish between different lattice positions. To identify this conserved quantity, we employ Bloch's theorem, which asserts that a translated eigenstate only differs by a phase factor for equivalent lattice positions: $\phi_{n,\mathbf{k}}(\mathbf{x}+\mathbf{a_0}) = \exp(i\mathbf{k}\cdot\mathbf{a_0})\phi_{n,\mathbf{k}}(\mathbf{x})$. Notably, the $\mathbf{k}$ within the phase factor is not uniquely defined; any $\mathbf{k}' = \mathbf{k}+\mathbf{G}$ would yield the same solution due to $\exp(i\mathbf{G}\cdot\mathbf{a_0}) = 1$. Consequently, $\phi_{n,\mathbf{k}}(\mathbf{x}) = \phi_{n,\mathbf{k}+\mathbf{G}}(\mathbf{x})$, implying that $\mathbf{k}$ is conserved only up to a reciprocal (momentum) lattice vector $\mathbf{G}$. To

avoid ambiguity between equivalent $\mathbf{k}$ values, it is customary to constrain its range to the first reciprocal lattice, known as the First Brillouin Zone (FBZ).

Shifting our focus to the eigenvalues of Bloch states, the energy bands, we may wonder why energy bands arise in crystals, in contrast to the discrete energy levels seen in atoms or molecules. This can be succinctly explained. In a classic finite potential well, distinct energy levels emerge, similar to the atomic scenario, as depicted in Fig. 3.1(a). In the case of a double well system, when the two wells are well-separated, as shown in Fig. 3.1(b), they behave independently and possess identical energy levels. However, as the separation between the wells is reduced, as seen in Fig. 3.1(c), energy level splitting into bonding and anti-bonding states occurs, akin to a diatomic molecule. Introducing additional identical wells leads to further energy level splitting with the eventual emergence of a continuous energy band becoming more suitable than an abundance of minimally split discrete levels, exemplified in Fig. 3.1(d). The distinct energy levels within a band are optimally described by the crystal momentum $\mathbf{k}$. As a result, a crystal's energy structure $E_n(\mathbf{k})$ is often depicted as a function of $\mathbf{k}$, as illustrated in Fig. 3.2.

All band structures exhibit several common characteristics. First, the band structure is invariably periodic with respect to $\mathbf{G}$, i.e., $E_n(\mathbf{k} + \mathbf{G}) = E_n(\mathbf{k})$, as we previously observed with the conservation of crystal momentum. Second, bands are symmetric with respect to $\mathbf{k}$, such that $E_n(\mathbf{k}) = E_n(-\mathbf{k})$. This symmetry persists even in the absence of

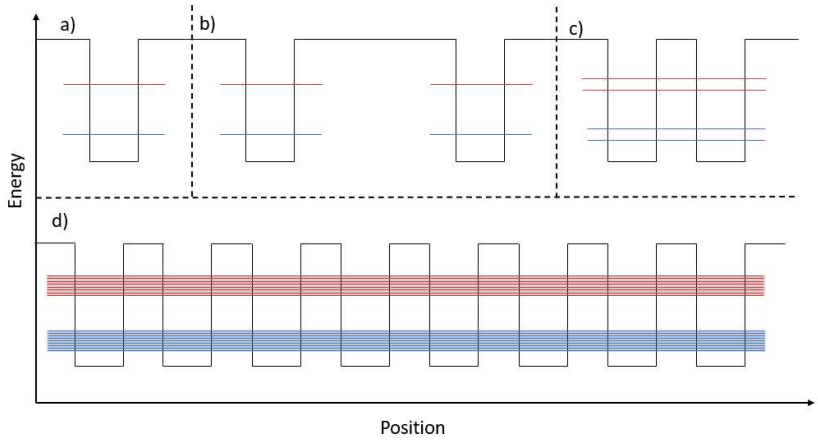

Figure 3.1 Lowest energy levels of different quantum wells (blue and red lines) for a) a single well, b) two independent wells, c) two dependent wells, and d) a large number of dependent wells. The splitting of energy levels leads to the formation of energy bands.

inversion symmetry in the crystal lattice. In the presence of spin-orbit coupling, the bands will exhibit symmetry when both $\mathbf{k}$ and spin are reversed. This can be established by demonstrating that $\hat{H}_{-\mathbf{k}} = \hat{H}^*_{\mathbf{k}}$. Third, the width of a band invariably increases with higher band indices, reflecting the fact that electrons at higher energies are less confined by the periodic potential. Fourth, zones of forbidden energy known as bandgaps emerge between bands, and these gaps become smaller at higher energies. Fifth, all bands feature inflection points along the high symmetry points of the crystal, including the Brillouin zone edges. As indicated in Eq. 3.5, an electron's velocity is tied to the derivative of the band. At these inflection points, the electron changes direction because its wavelength matches an integer multiple of half the crystal periodicity, resulting in Bragg reflection. Finally, higher bands progressively resemble parabolic

behavior with diminishing bandgaps, signifying that high-energy electrons exhibit behavior increasingly akin to that of free electrons and are less influenced by the crystal potential. In contrast, the lower bands are less accurately described by a parabolic model. These distinctions hold important implications for HHG in solids.

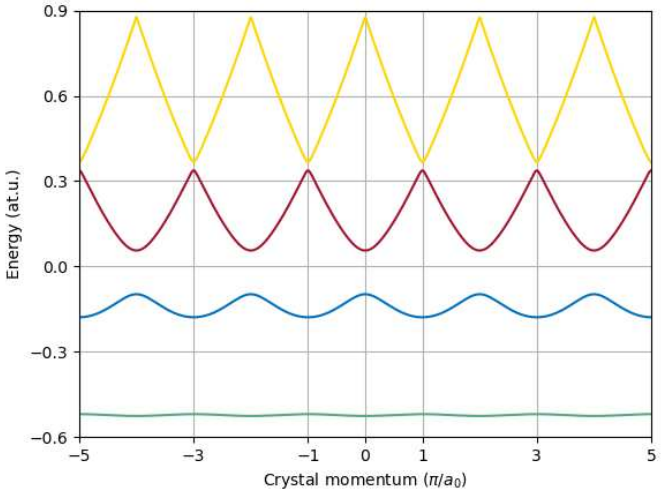

Figure 3.2 Energy structure as a function of crystal momentum for a 1D potential. The major grid lines in crystal momentum, excluding $k = 0$, indicate the various Brillouin zone edges.

3.2 Crystals Under an Electric Field

To comprehend the behavior of HHG in solids, we must introduce the influence of an electric field into our analysis. In terms of the Hamiltonian, the impact of an electric field is analogous to the description provided in Eq. 2.2. We can readily adapt this concept to the **k**-dependent Hamil-

tonian of Eq. 3.2:

$$\hat{H}_{\mathbf{k}}^{(v)} = \frac{1}{2}\left(\hat{\mathbf{p}} + \mathbf{k} + \mathbf{A}(t)\right)^2 + V(\mathbf{x}); \tag{3.6a}$$

$$\hat{H}_{\mathbf{k}}^{(l)} = \frac{1}{2}\left(\hat{\mathbf{p}} + \mathbf{k}\right)^2 + V(\mathbf{x}) + \mathbf{F}(t) \cdot \hat{\mathbf{x}}, \tag{3.6b}$$

In Eq. 3.6, Eq. 3.6a and Eq. 3.6b correspond to the velocity gauge and length gauge versions of the **k**-dependent Hamiltonian, respectively. Velocity gauge means that the electric field is fully described by the vector potential and not the scalar potential ($\Phi_F(\hat{x}, t) = 0$). From the velocity gauge version, it is evident that the crystal momentum will be influenced by the vector potential:

$$\mathbf{k}(\mathbf{t}) = \mathbf{k_0} + \mathbf{A}(t), \tag{3.7}$$

where $\mathbf{k}(\mathbf{t})$ represents the streaked crystal momentum and $\mathbf{k_0}$ denotes the crystal momentum in the absence of an electric field. As previously mentioned, we will predominantly utilize the length gauge version of this Hamiltonian and employ the vector potential solely to streak the momentum.

3.3 Electron Motion Under an Electric Field in a Crystal

When considering the behavior of an electron in a crystal under the influence of an electric field, we should anticipate coupling between different bands as Bloch states are non-eigenstates of this new Hamiltonian. To simplify our analysis, we will initially disregard this coupling and focus on a single band, as depicted in Fig. 3.3a). To begin with, let us consider the case of a static electric field $\mathbf{F_0}$ which is equivalent to a linear vector potential. Consequently, the electron will streak the whole bandstructure, as illustrated in Fig. 3.3b). Given that the bandstructure is periodic in $\mathbf{k}$, the electron's velocity, as per Eq. 3.5, will also exhibit periodic oscillations, demonstrated in Fig. 3.3c). We can define a period during which the electron revisits an equivalent $\mathbf{k}$ point. The corresponding frequency to this period is referred to as the Bloch frequency:

$$\omega_b = F_0 a_0. \tag{3.8}$$

The Fourier transform of this oscillatory velocity is displayed in Fig. 3.3d). The spectrum reveals peaks at multiples of the Bloch frequency. Surprisingly, even a static field gives rise to oscillating electric fields! This phenomenon arises due to the inflection points in the bandstructure, where the electron's velocity changes direction. In an experimental context, such a distinct spectrum might not be observable, as collisions with other electrons or lattice vibrations could reset the electron's crystal momentum. However, an ultrashort laser pulse can achieve momentum

streaking before collisions interfere, though it's important to note that an ultrashort pulse, by definition, is not a static field. Thus, let's explore the impact of an AC field.

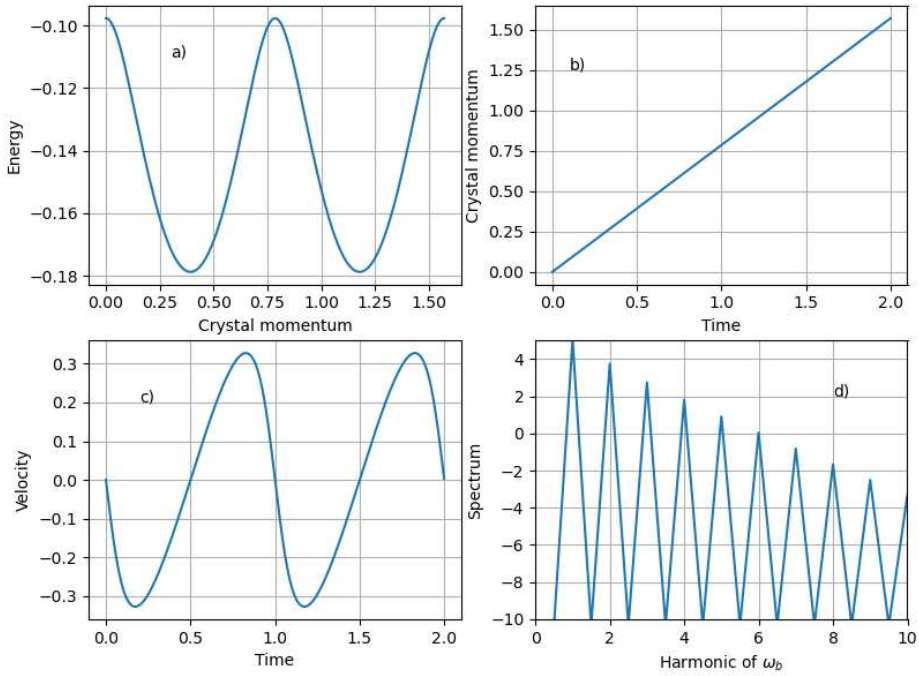

Figure 3.3 In a single band (a), an electron under a static field will have a linearly increasing crystal momentum (b). Its velocity will oscillate (c) with a frequency related to the Bloch frequency ω_b (d). The spectrum shown in (d) is on a logarithmic scale.

Fig. 3.4 illustrates an electron confined within a single band, subjected to an oscillating field at frequency ω_0. As shown in Figs. 3.4a)-b), the crystal momentum no longer streaks along the entire band, but rather explores only a portion of the bandstructure in a periodic manner. The corresponding velocity, depicted in Fig. 3.4c), exhibits oscillations, but

with a distinct pattern from the driving electric field. Spectral analysis of this velocity unveils clear harmonic peaks, as presented in Fig. 3.4d).

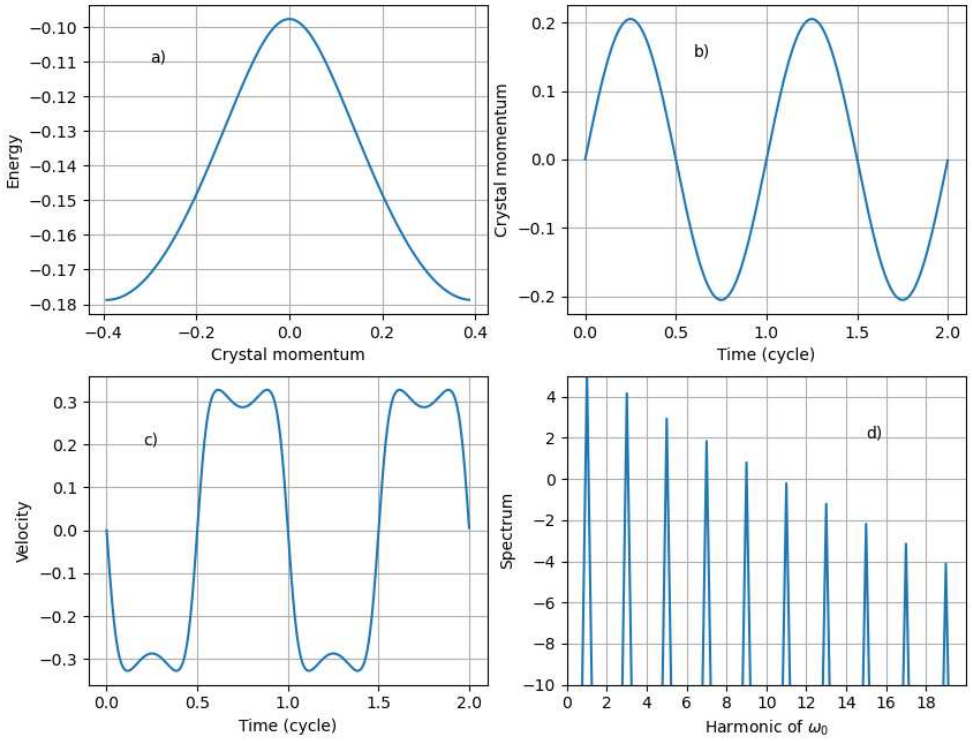

Figure 3.4 In a single band (a), an electron under an oscillating field will exhibit oscillatory behavior in its crystal momentum (b). Its velocity will oscillate (c) with pronounced modulation. The emitted frequencies will be harmonics of the driving field frequency ω_0 (d). The spectrum shown in (d) is on a logarithmic scale.

The deviation from a parabolic band structure is the primary factor behind the generation of harmonics. In cases where the bands are parabolic, the electron's velocity would linearly correlate with the vector

potential, resulting in oscillations at the electric field frequency. However, due to the non-linear relationship between vector potential and velocity within a crystal, spectra featuring harmonic peaks can arise. Only odd harmonics are observable, as each half-cycle of the driving field leads to the same velocity profile but in the opposite direction.

This mechanism was initially proposed to explain the first observation of high harmonics in a semiconductor [16]. However, this model was limited to a single band and a single electron within that band. A completely filled band would not yield any harmonics due to the presence of an electron with opposing velocity, in accordance with the inversion symmetry of the bands. To generate high harmonics, an ionization mechanism is needed to elevate electrons from the filled valence band to the vacant conduction band. High harmonics can then be produced through electrons and holes in the conduction and valence bands, respectively.

As previously mentioned, Bloch states are not eigenstates of Eq. 3.6b, allowing for coupling through the position operator. Therefore, it is essential to define the dipole matrix element between different Bloch states [51]:

$$\langle \phi_{n',\mathbf{k}'} |\, \hat{\mathbf{x}} \,| \phi_{n,\mathbf{k}} \rangle = -i\delta_{n,n'} \nabla_{\mathbf{x}} \delta(\mathbf{k} - \mathbf{k}') + \delta(\mathbf{k} - \mathbf{k}') \Xi_{n',n}(\mathbf{k}), \tag{3.9}$$

Here, $\delta(\mathbf{k} - \mathbf{k}')$ represents the Dirac delta function, $\delta_{n',n}$ is the Kronecker

delta, and $\Xi_{n',n}(\mathbf{k})$ is defined as:

$$\Xi_{n',n}(\mathbf{k}) = i \int\limits_{\text{Unit cell}} d\mathbf{x}\, u^*_{n',\mathbf{k}}(\mathbf{x}) \nabla_{\mathbf{k}} u_{n,\mathbf{k}}(\mathbf{x}). \tag{3.10}$$

The first term on the right-hand side of Eq. 3.9 couples Bloch states within the same band that are neighboring in k value. In other words, this term represents the streaking of the crystal momentum by the vector potential, as previously defined in Eq. 3.7. The second term couples Bloch states with the same crystal momentum and is usually categorized as another intraband ($n' = n$) and a new interband ($n' \neq n$). The new intraband term is known as the Berry connection and contributes to anomalous velocity. Although significant, we will not focus on this term in this thesis, as it is often negligible for inversion-symmetric materials. The interband term allows transitions between bands while conserving crystal momentum. As with the atomic gas case, we can define this ionization process to be in either the tunneling or the multiphoton regime using the Keldysh parameter. In the context of solids, the Keldysh parameter takes the following form [41]:

$$\gamma \propto \frac{\omega_0 \sqrt{m_e E_g}}{F_0}, \tag{3.11}$$

where m_e represents the effective reduced mass of electrons and holes, associated with the curvature of the bands, and E_g is the energy bandgap. Throughout the remainder of this thesis, we will assume that ionization

occurs in the tunneling regime ($\gamma \ll 1$).

3.4 The Lewenstein Model in Solids

Having explored the behavior of Bloch states under an electric field, we can derive the differential equation describing the evolution of their coefficients by employing the Hamiltonian from Eq. 3.6b [26]. We define the total wavefunction as:

$$|\Psi(t)\rangle = \sum_n c_{n,k_0}(t) \exp\left(i \int_{-\infty}^{t} E_n(k(\tau))d\tau\right) \left|\phi_{n,k(t)}\right\rangle . \tag{3.12}$$

In this formulation, we have included the energy integral to cancel the effect of H_0, and we have defined the Bloch function in terms of $k(t)$, similar to Eq. 3.7, to eliminate the first term of Eq. 3.9 when using this total wavefunction in the TDSE.

$$\dot{c}_{n,k_0}(t) = -iF(t) \sum_{n'} c_{n',k_0}(t) \Xi_{n,n'}(k(t)) \exp\left(-i \int_{-\infty}^{t} E_{n',n}(k(\tau))d\tau\right), \tag{3.13}$$

where, $E_{n',n}(k(\tau)) = E'_n((k(\tau)) - E_n((k(\tau))$. In other words, the change in the population of a Bloch state is mostly related to the dipole moment between different bands.

Assuming that only two relevant bands exist, namely the valence band and the first conduction band ($n = \{v, c\}$), and that the population of the valence band remains nearly unchanged by the electric field ($c_v(t) \approx 1$), we can derive an expression for the population of the conduction band:

$$c_{c,k_0}(t) = -i \int_{-\infty}^{t} dt' F(t') \Xi_{c,v}(k(t')) \, \mathrm{e}^{i \int_{-\infty}^{t'} E_g(k(\tau)) d\tau}. \tag{3.14}$$

Here, $E_g = E_{c,v}$. With this expression, we can determine the velocity of electrons in the bands:

$$\begin{aligned} v(t) &= \frac{d}{dt} \langle \Psi(t) | \, \hat{x} \, | \Psi(t) \rangle \\ &= \frac{d}{dt} \left[\sum_{n,n'} c^*_{n,k_0}(t) c_{n,k_0}(t) \, \mathrm{e}^{-i \int_{-\infty}^{t'} E_g(k(\tau)) d\tau} \left\langle \phi_{n,k(t)} \right| \hat{x} \left| \phi_{n',k(t)} \right\rangle \right] \\ &= \frac{d}{dt} \left[-i \Xi_{v,c}(k(t)) \int_{-\infty}^{t} dt' F(t') \Xi_{c,v}(k(t')) \, \mathrm{e}^{i \int_{t'}^{t} E_g(k(\tau)) d\tau} \; + c.c \right] \\ &\quad + |c_{c,k_0}(t)|^2 \nabla_{k(t)} E_c(k(t)), \end{aligned} \tag{3.15}$$

where we have utilized the Ehrenfest Theorem for the intraband terms ($c^*_{c,k_0}(t) c_{c,k_0}(t)$) to transform the position operator into the momentum operator and applied the result from Eq. 3.5. In this velocity equation, two terms are evident: an interband term and an intraband term. The intraband term aligns with the initial hypothesis proposed to explain the harmonic emission in semiconductors. The crucial question at this point

is to determine which of these terms dominates the harmonic generation process. To address this, we can examine the phase of the emitted harmonics. The intraband term is closely linked to the population of the conduction band $|c_{c,k_0}(t)|^2$, which experiences spikes during the ionization process—a highly nonlinear phenomenon that peaks with the extrema of the electric field. We therefore expect the same time of emission for all the harmonics produced by the intraband term; they are all in phase. On the other hand, the interband term exhibits a more complex relationship in terms of when specific harmonics are emitted. To unveil this relationship, we can apply the saddle point approximation to solve the integrals of the spectrum, similar to what was done for the Lewenstein model in Eq. 2.7:

$$S(\omega) = i\omega^2 \int_{-\infty}^{\infty} dt \int_{1^{\text{st}}BZ} dk_0 \Xi_{v,c}(k(t)) \int_{-\infty}^{t} dt' F(t') \Xi_{c,v}(k(t')) \, \mathrm{e}^{i\zeta(k_0,t',t)} + c.c, \tag{3.16}$$

Here, $\zeta(k_0, t', t) = \omega t + \int_{t'}^{t} E_g(k(\tau))d\tau$ represents the fast oscillating part of the spectrum on which we can apply the saddle point approximation at $(k_0, t', t) = (k_s, t_i, t_r)$, similar to the gas phase:

$$\frac{\partial \zeta(k_s, t_i, t_r)}{\partial t'} = E_g(k_s(t_i)) = 0; \tag{3.17a}$$

$$\frac{\partial \zeta(k_s, t_i, t_r)}{\partial k_0} = \int_{t_i}^{t_r} \nabla_{k_0} E_g(k_s(\tau))d\tau = \Delta x_c - \Delta x_v = 0; \tag{3.17b}$$

$$\frac{\partial \zeta(k_s, t_i, t_r)}{\partial t} = E_g(k_s(t_r)) = \omega. \tag{3.17c}$$

These three saddle points describe a similar picture as in the gas phase. First, the electron must tunnel ionize from the valence band to the conduction band. Then, the electron and the parent hole must find each other before they can recombine and emit their instantaneous energy difference. Two key differences are that the parent ion is now a hole that gets accelerated in the opposite direction to the electron, and the instantaneous energy is determined by the energy difference between the conduction and valence bands. Consequently, a similar relationship between the time an harmonic is emitted and the driving electric field can be established. The existence of an attochirp would be indicative of the dominance of the interband pathway for harmonic generation.

This can be seen in numerical results of Eq. 3.13 [21]. A small important technicality needs to be mentioned with the modeling of these interband harmonics. When solving numerically Eq. 3.13, no sharp harmonics can be found. The reason for it is that electron and hole may have more than one recombination event leading to destructive interference. To suppress later recombinations, the equations are changed from a wavefunction approach to a density matrix which are called the Semiconductor Bloch Equations (SBE). The SBE have the degree of freedom to slowly kill the coherence (off-diagonal elements) between the electron and the hole. This is done by adding by hand on the off-diagonal elements of the Hamiltonian a term of the form $-i/T_2$, where T_2 is called

the dephasing term and is usually smaller than the period of the driving laser. The dephasing of electron and the hole might not be that fast in the real world (collisions, impurities, etc.) but T_2 helps capture the phasematching problem that would arise if we were to do the simulation on few lattice cells in the direction of the propagation of the laser [52].

The results of these simulations are that interband harmonics dominates a plateau region above the bandgap and that intraband is the dominant path for harmonics below the bandgap. Since we cannot separate the intraband and interband contribution easily in a laboratory, the phase of the harmonics can be used to infer the pathway. The model predicts that above bandgap harmonic should have an attochirp while the ones below should not.

To test this hypothesis, a two-color experiment was performed in a semiconductor and an attochirp was revealed for the harmonics above the bandgap energy confirming the interband hypothesis [53]. For the harmonics below the bandgap, intraband seems to be dominant pathway. However, shortly after an experiment done in quartz, a dielectric, found that intraband was the dominant path for all harmonics [18].

3.5 Unresolved questions

The question of interband versus intraband was a hot topic in the community. Since, the division is dependant on a model (no direct way to separate these contributions in the lab), we started to see some incon-

sistency in the literature with respect to separation of these two terms especially when another gauge was used for the electric field [54]. One of the first question I answered for my thesis was how to properly separate the intraband and interband terms in both length and velocity gauge and his the subject of the next chapter 4.

While the model for interband was very successful to explain the attochirp, it still was incomplete. One of them was the impossibility to explain the presence of even and odd harmonics in non-centrosymmetric material. It was also limited for materials that were spatially uniform. The model relies on Bloch functions which assumes an infinite periodic material and made the approximation that the dipole was uniform along $\mathbf{k}$. It did not have the degree of freedom to include impurities, heterostructure or nonuniform electric field spatially like when a nanoantenna is present. All of these systems are degrees of freedom that a solid material provides that were not possible with gas phase experiment. For the gas phase, the current model has a clear picture both in the real and momentum space. The model described above for solids only has a momentum picture and a hint of real space perspective in the sense that electron and hole travels in opposite direction but must meet again spatially before recombining. This incompleteness is pictured in Fig. 3.5. The question of a real space model for harmonics in solids will be the heart of this thesis and start to be addressed in chapter 5.

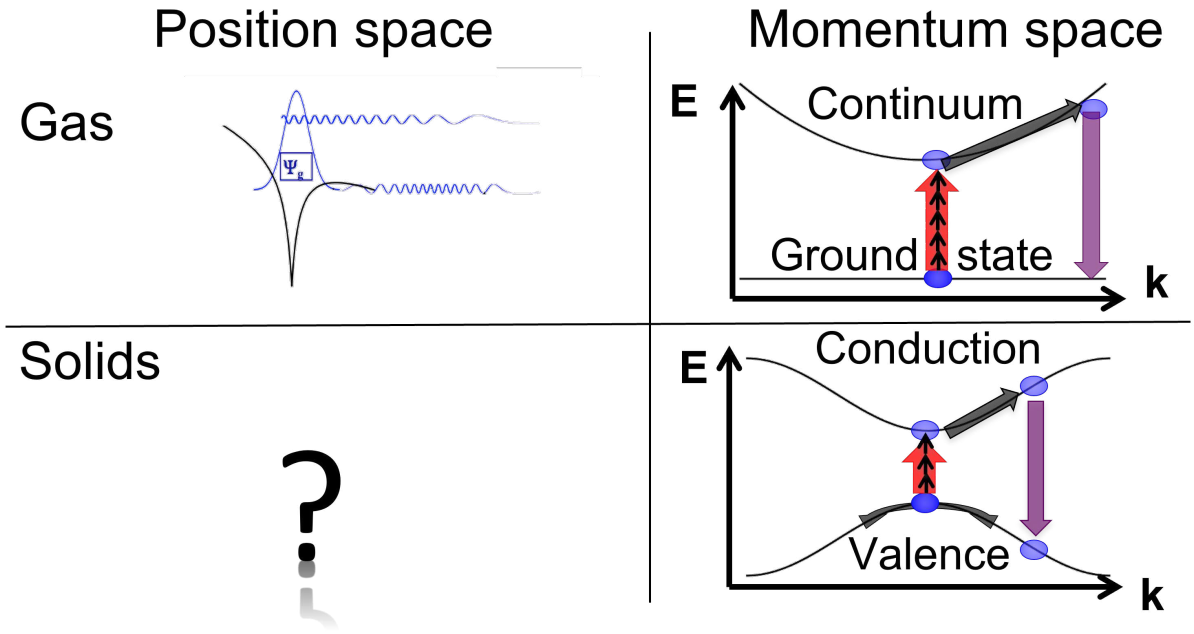

Figure 3.5 The current theory for high harmonic generation (HHG) in gases provides a clear understanding in both real space and momentum space. In this process, an electron is initially tunnel-ionized from its parent ion, gains acceleration in the continuum, and subsequently, when the electric field polarity changes, it has the opportunity to recombine with its parent ion, releasing its accumulated momentum as a high-energy photon. In contrast, the model for HHG in solids primarily operates within momentum space. Here, electrons can engage in either a three-step process akin to the gas phase, but this time transitioning between the valence and conduction bands (interband), or they can emit harmonics of the driving field due to non-parabolic characteristics of the bands (intraband).

Part III

Results

CHAPTER 4 A Gauge-Invariant Formulation of Interband and Intraband Currents in Solids

4.1 Introduction

When I embarked on my thesis, the pivotal question of whether intraband or interband harmonics play a more significant role in high harmonic generation (HHG) in solids, and the types of materials where this distinction is most relevant, was a central concern. While the separation between these two types seems straightforward—labeling it intraband if the transition starts and ends within the same band, and interband if it spans different bands—the seemingly simple task is complicated by the choice of electromagnetic gauge. Moreover, the gauge choice leads to discrepancies in the total population of a band. In the length gauge calculation for a single electron, information about the bands across all streaked $\mathbf{k}$ values in the first Brillouin zone is needed. However, the velocity gauge calculation for a single electron only requires information about the bands at $\mathbf{k_0}$, albeit involving a larger number of bands. In essence, the bands become dressed by the field, and the choice of field description affects this dressing.

As the initial separation of Bloch states was derived in the length gauge [21], as in Eq. 3.15, we endeavored to rigorously extend a similar separation to the velocity gauge. This entailed gauge-transforming the

projection operator Π_{n,k_0} for one band and its total population Π_n:

$$\Pi_n^{(l)} = \int\limits_{1^{\text{st}}BZ} dk_0 \Pi_{n,k_0}^{(l)} = \int\limits_{1^{\text{st}}BZ} dk_0 \left|\phi_{n,k_0}\right\rangle \left\langle\phi_{n',k_0}\right| . \tag{4.1}$$

To achieve this, we needed to determine the overlap of different periodic parts of Bloch states:

$$\Delta_{n,m}(k_0, k_1) = \left\langle u_{n,k_0} | u_{m,k_1} \right\rangle . \tag{4.2}$$

Essentially, we required insight into which bands n are relevant to describe the same situation in velocity gauge (electron still at $\mathbf{k_0}$) as the one in length gauge (electron streaked from $\mathbf{k_0}$ to $\mathbf{k_1}$). This allowed us to derive the transformed projection operator in the velocity gauge:

$$\Pi_n^{(v)} = \sum_{m,m'} \int\limits_{1^{\text{st}}BZ} dk_0 \Delta_{n,m}^*(k_0 + A, k_0) \Delta_{n,m'}(k_0 + A, k_0). \tag{4.3}$$

With this novel expression, we were able to consistently describe the total population and achieve an accurate intra/interband current separation. Our findings are detailed in the following PRB article.

4.2 Article

For the subsequent paper, I contributed to every phase of its development: generating ideas, conducting mathematical derivations, performing numerical testing, and participating in the writing process.

PHYSICAL REVIEW B **98**, 235202 (2018)

A gauge-invariant formulation of interband and intraband currents in solids

Guilmot Ernotte,[1] T. J. Hammond,[2] and Marco Taucer[1,*]

[1]*Joint Attosecond Science Laboratory, National Research Council of Canada and University of Ottawa, Ottawa, Ontario K1A 0R6, Canada*

[2]*Department of Physics, University of Windsor, Windsor, Ontario N9B 3P4, Canada*

(Received 28 August 2018; revised manuscript received 27 October 2018; published 4 December 2018)

Experiments and simulations in solid-state high harmonic generation often make use of the distinction between interband and intraband currents. These two contributions to the total current have been associated with qualitatively different processes as well as physically measurable signatures, for example, in the spectral phase of harmonic emission. However, it was recently argued [P. Földi, Phys. Rev. B **96**, 035112 (2017)] that these quantities can depend on the gauge employed in calculations. Since physical quantities are expected to have gauge-independent values, this raises the question of whether the decomposition of the total current into interband and intraband contributions is physically meaningful or merely a feature of a particular mathematical representation of nature. In this article, we explore this apparent ambiguity. We show that a closely related issue arises when calculating instantaneous band populations. In both the case of inter/intraband currents and the case of instantaneous band populations, we propose definitions that are gauge invariant and thus allow these quantities to be calculated consistently in any gauge.

DOI: 10.1103/PhysRevB.98.235202

I. INTRODUCTION

The strong field of a pulsed laser can drive extremely nonlinear currents in a solid, leading to the emission of high-order harmonics of the fundamental frequency that can span the visible spectrum and extend into the extreme ultraviolet [1]. The process can take place in a wide range of materials from dielectrics to semiconductors to semimetals and can leave the material undamaged [2–7]. Strong field and attosecond science in condensed matter is an extension of the long-standing field of high harmonic generation, which was for many years confined to gas-phase atoms and molecules [8]. Solids remain a new area of this field in which some basic questions remain unanswered, whereas others may not even be precisely defined.

In that respect, as part of the search for an underlying physical picture of the harmonic generation process, experimentalists and theorists alike have focused much attention on the division of the total current into interband and intraband processes. This conceptual separation is appealing in part because the interband picture bears a strong similarity to the well-understood gas-phase model [7,9,10], whereas the intraband picture is qualitatively different and, for the most part, unique to the solid state [6,11]. Experiments have access to the complex amplitude of the emitted harmonics, which reflects the coherent sum of the interband and intraband contributions, whatever their relative weight may be. For now, a clean separation is only possible in calculations; any conclusions about the dominance of one mechanism or the other relies on a comparison with theoretical predictions of the interband and intraband spectra [2,6,7,10–16]. Recently, however, Földi showed that this separation may be gauge dependent [17]. That is, a different choice of the gauge, which should leave all physical quantities unchanged, leads to different values for the interband and intraband currents. However, the total current, which relates to the experimentally observed harmonic spectrum, is not gauge dependent. This raises the question of whether this conceptual decomposition of the current is physically meaningful. Is the interband current an observable?

Other quantities may also be easy to calculate but hard to access in experiments. An example is the instantaneous band population. In the strong-field physics of solids, simulations often show a transient conduction-band population that oscillates with the applied field but mostly returns to the valence band at the end of the pulse. The fraction of the population remaining in the conduction band at the end of the pulse depends on the band structure and the pulse shape as well as the dephasing time constant [18]. Although this final population is gauge independent, the transient population dynamics during the laser pulse's illumination can be subject to a gauge dependence that is analogous to that of the inter- and intraband currents as we will show below. This raises the question of the significance of the instantaneous band populations. Can such a quantity be precisely defined, particularly given that in the presence of a strong driving field the instantaneous eigenstates are the dressed states, which are not the same as the field-free eigenstates? The question is all the more compelling given that some attosecond-probe experiments appear to measure precisely this quantity [19].

The aim of the present article is to create gauge-invariant definitions of these quantities of interest. We start by identifying the Hermitian operators corresponding to the instantaneous band populations and to the interband and intraband currents. Once defined, we derive their gauge-dependent transformations, which ensures gauge-invariant physical predictions. Although we primarily focus on the commonly used

*Marco.Taucer@nrc-cnrc.gc.ca

velocity and length gauges, our definition is equally valid in any other gauge.

This paper is organized as follows. In Sec. II, we introduce the theoretical formalism and the details of our numerical calculations. Section III discusses an intuitive, but problematic, approach to defining interband and intraband currents as well as band populations. In Sec. IV, we provide a more rigorous definition of the instantaneous band population as a Hermitian operator. We then calculate the gauge transformation of its matrix elements. Section V similarly describes the interband and intraband currents in terms of Hermitian operators with corresponding gauge transformations. The improved definitions of these quantities yield gauge-invariant predictions. Finally, in Sec. VI, we show that our definitions give reasonable physical descriptions, and we discuss the choices made in coming to this formulation.

II. THEORETICAL APPROACH

For a single particle in a one-dimensional periodic potential $V_0(x + a_0) = V_0(x)$ with a lattice constant of a_0, the Hamiltonian in the absence of the laser field is

$$\hat{H}_0 = \frac{\hat{p}^2}{2} + V_0(\hat{x}). \tag{1}$$

Here and throughout this paper we use atomic units except where other units are specified. The eigenstates of this Hamiltonian can be labeled by a band index n and the crystal momentum k,

$$\hat{H}_0|\phi_{nk}\rangle = \varepsilon_n(k)|\phi_{nk}\rangle. \tag{2}$$

The energies $\varepsilon_n(k)$ trace out the band structure, and the Bloch functions, expressed in the position basis, have the property $\langle x|\phi_{nk}\rangle \equiv \phi_{nk}(x) = \sqrt{\frac{a_0}{2\pi}} e^{ikx} u_{nk}(x)$, where $u_{nk}(x + a_0) = u_{nk}(x)$ is periodic and normalized over one unit cell.

As a model system, we use the previously studied Mathieu potential $V_0(x) = -V_0[1 + \cos(2\pi x/a_0)]$ with $V_0 = 0.37$ and $a_0 = 8$ atomic units [20–24]. We solve the time-independent Schrödinger equation in the position basis with periodic boundary conditions to find the field-free eigenstates (Bloch states). These are then used as the basis for calculations of the time dynamics in a driving laser field. Figure 1 shows the band structure as a function of crystal momentum for the first five bands. The black circle in the center of the band with index $n = 1$ represents the initial condition for simulations: $|\phi_{1,k=0}\rangle$, a single electron at the Γ point in band 1. Roughly speaking, bands 1 and 2 can be thought of as the valence band and the first conduction band, respectively. However, our calculation considers band 0 to be unoccupied as well as all other k points in band 1. Although this simplification does not represent the reality of valence bands, it allows a comparison with previous reports and has no effect on the conclusions of this paper.

The effect of a laser field, which we treat here within the dipole approximation, leaves freedom with respect to the gauge chosen since the field can be divided nonuniquely between a scalar potential Φ and a vector potential A. In the length gauge, the field is incorporated exclusively through the

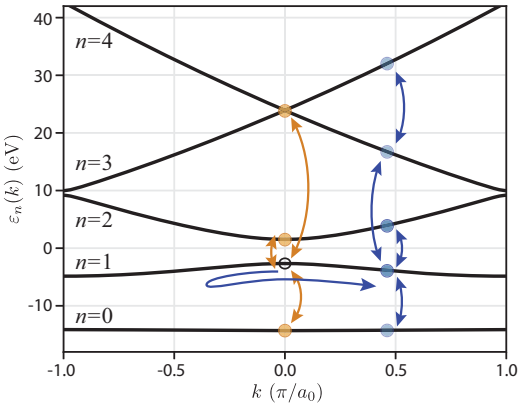

FIG. 1. Band structure for the Mathieu potential, showing the lowest five bands, labeled with their band indices, as a function of crystal momentum in the first Brillouin zone (BZ). The black circle in band 1 shows the initial condition for our simulation. Orange and blue arrows/circles illustrate the dynamics as described in the velocity and length gauges, respectively. Both gauges describe the time-dependent wave function as a superposition of Bloch states at a particular crystal momentum, but in the velocity gauge the crystal momentum is fixed, whereas, in the length gauge, it oscillates with the vector potential.

scalar potential,

$$\begin{aligned} \Phi^{(l)}(x,t) &= -F(t)x, \\ A^{(l)}(t) &= 0, \end{aligned} \tag{3}$$

where $F(t)$ represents the electric field. In the velocity gauge, the situation is reversed

$$\begin{aligned} \Phi^{(v)}(x,t) &= 0, \\ A^{(v)}(t) &= -\int_{-\infty}^{t} F(t')dt'. \end{aligned} \tag{4}$$

The Hamiltonian, including the interaction with the light field, under the dipole approximation, can be written in any gauge, labeled with superscript (g), as

$$\hat{H}^{(g)} = \frac{1}{2}[\hat{p} + A^{(g)}(t)]^2 + V_0(\hat{x}) - \Phi^{(g)}(\hat{x}, t). \tag{5}$$

Note that when the field and the (velocity-gauge) vector potential are both zero (that is, before or after the pulse), the Hamiltonian reduces to $\hat{H}_0$ in both the velocity and the length gauge.

Hermitian operators corresponding to observables transform between the two gauges according to [25–27]

$$\hat{O}^{(v)} = e^{-iA^{(v)}\hat{x}} \hat{O}^{(l)} e^{iA^{(v)}\hat{x}}, \tag{6}$$

and the wave functions are related by

$$|\psi^{(v)}\rangle = e^{-iA^{(v)}\hat{x}}|\psi^{(l)}\rangle. \tag{7}$$

More generally, wave functions and operators are transformed from gauge (g_1) to gauge (g_2) by the unitary operator,

$$\hat{U}_{(g_1)\to(g_2)} \equiv e^{i[A^{(g_2)} - A^{(g_1)}]\hat{x}}. \tag{8}$$

In this article, we choose to equate the field-free operator for our quantities of interest with the operator's representation in the length gauge. Although this is not the only possible choice, we will provide a justification below and show that this definition gives reasonable physical predictions. Starting from the length gauge, then, the transformation to any other gauge (g) is described by

$$\hat{U} \equiv \hat{U}_{(l)\to(g)} = e^{iA^{(g)}\hat{x}}. \tag{9}$$

In each gauge, the vector potential dictates a time-dependent transformation. As long as wave functions and Hermitian operators transform via the unitary operator of Eq. (9), expectation values remain unchanged by the gauge transformation. In other words, the different gauges all represent the same physics.

We solve the time-dependent Schrödinger equation (TDSE) in the field-free basis numerically. We write wave functions in gauge g as

$$|\psi^{(g)}(t)\rangle = \sum_n \int_{BZ} dk\, c_{nk}^{(g)}(t)|\phi_{nk}\rangle. \tag{10}$$

The amplitudes $c_{nk}^{(g)}(t)$ depend on the gauge. For numerical simulations, the laser field is defined by $A^{(v)}(t) = A_0 \cos^4(\omega_0 t/2n_c)\cos(\omega_0 t)$, where $A_0 = 0.3$ is the peak vector potential, $n_c = 11$ is the number of cycles in the pulse, a fundamental frequency of $\omega_0 = 2\pi c/\lambda$ with c as the speed of light, and $\lambda = 3.2\ \mu$m as the wavelength. Our parameters are identical to those used by Wu *et al.* [20,21]. Although several other approaches, notably that of Földi [17], use density matrices rather than wave functions, the underlying physics is identical aside from the ability to treat mixed states and decoherence. Our treatment of gauge dependence in coherent calculations applies to both types of calculation, and the operator definitions that we propose are valid for either. The gauge dependence of specific decoherence models is another matter and was the subject of a recent article [28].

In the presence of the laser field, the Hamiltonian expressed in the field-free basis acquires off-diagonal elements that couple the Bloch states. This coupling is determined by the matrix elements of the momentum operator in the velocity gauge or by the matrix elements of the position operator in the length gauge. The resulting set of coupled differential equations for the coefficients $c_{nk}^{(g)}(t)$ takes a different form in each gauge. In the velocity gauge,

$$i\frac{\partial}{\partial t}c_{nk}^{(v)} = \left[\varepsilon_n(k) + \frac{1}{2}A^{(v)2}\right]c_{nk}^{(v)} + A^{(v)}\sum_{n'} p_{nn'}(k)c_{n'k}^{(v)}. \tag{11}$$

The momentum operator only couples states with the same k value, $\langle\phi_{nk}|\hat{p}|\phi_{n'k'}\rangle \equiv p_{nn'}(k)\delta(k-k')$, meaning that the initial crystal momentum, in the velocity-gauge description, remains constant even under the influence of the laser field.

In the length gauge,

$$i\frac{\partial}{\partial t}c_{nk}^{(l)} = \varepsilon_n(k)c_{nk}^{(l)} + iF\frac{\partial}{\partial k}c_{nk}^{(l)} + F\sum_{n'}\xi_{nn'}(k)c_{n'k}^{(l)}. \tag{12}$$

The position matrix elements likewise contain a part that mixes states of the same k value, denoted $\xi_{nn'}(k)$, which, for nondegenerate states, is given by $\xi_{nn'}(k) = -ip_{nn'}(k)/[\varepsilon_n(k) - \varepsilon_{n'}(k)]$. However, the position operator additionally contains a differential term that couples neighboring k values and leads to the acceleration theorem: A state initially having $k = k_0$ evolves into states with $k(t) = k_0 + A^{(v)}(t)$. The acceleration theorem illustrates an important difference between these two gauges: In the velocity gauge, the crystal momentum remains fixed, whereas in the length gauge, the evolution of the wave function in the laser field leads to an oscillation of the electron's crystal momentum. This is illustrated by the colored circles and arrows in Fig. 1. We will show that these two pictures are connected by the functions $\Delta_{nm}(k_1, k_2)$, defined below, which make a precise connection between states spanning several bands at a given point in the Brillouin zone and states of a single band with a different k value.

III. DEFINITIONS BASED ON BAND INDICES

In this section, we discuss an intuitive yet problematic procedure for defining band populations and inter/intraband currents in which the band indices of coefficients are used to identify band-dependent quantities. This procedure is known to give gauge-dependent results [17]. In subsequent sections, we will attempt to improve upon these definitions.

Solving the Schrödinger equation in either gauge gives the time-dependent coefficients of the basis states and thereby the wave function. In particular, the coefficients $c_{nk}^{(g)}(t)$ are associated with state $|\phi_{nk}\rangle$, and, according to the Born rule, their modulus squared seems to represent the probability of finding an electron in that particular state. This reasoning implies that the instantaneous band population in band n is $\int dk|c_{nk}^{(g)}|^2$. Although this seems reasonable, we now show an example where interpreting this quantity as an instantaneous band population is problematic, particularly since its value is gauge dependent. The problem here is identical to the well-known issue of using the squared moduli of the amplitudes of field-free eigenstates to denote their probabilities [29]. Nonetheless, applying this definition to the conduction-band population, we find the time-dependent results shown in Fig. 2(a) for the velocity gauge (orange) and length gauge (blue).

Both gauges describe a transient population that oscillates and nearly completely returns to the valence band at the end of the pulse. Both calculations agree on the final population that remains in the conduction band at the end of the pulse. However, in the velocity gauge, the transient conduction-band population is much larger, as much as 40%, and it is peaked at the (velocity-gauge) vector potential maxima, whereas, in the length gauge, the apparent conduction-band population is peaked at the vector potential zeros. Also, whenever the vector potential [Fig. 2(c)] is zero, indicated by vertical dashed lines, the two gauges agree. This is to be expected since the unitary transformation [Eq. (9)] is the identity in that case. But, in general, the two calculations provide very different pictures of the transient conduction-band population, and whenever the vector potential is nonzero, it is not clear which one to trust. In the recent literature, it appears that both quantities have been reported [19,30–33]. It would be desirable to find

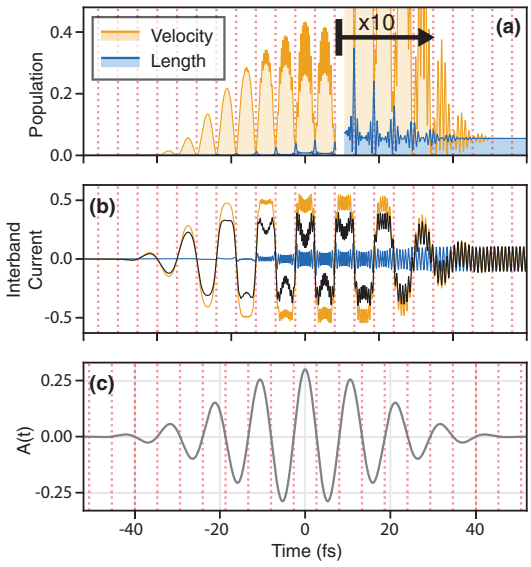

FIG. 2. Dynamics calculated using definitions based on band indices, illustrating the problematic gauge dependence that arises from this formulation. (a) Conduction-band population, defined as the squared modulus of the time-dependent coefficients, calculated in the velocity and length gauges. The region on the right side is magnified in the vertical dimension by a factor of 10. (b) Interband current, defined as the second summation in Eq. (13), calculated in the velocity gauge and length gauge. The total current, which is gauge independent provided one makes the transformation $\hat{p}^{(g)} = \hat{p} + A^{(g)}$, is shown in black for reference. (c) Velocity-gauge vector potential as a function of time. Vertical dashed lines in all plots indicate the zeros of this vector potential.

a gauge-independent formulation of the instantaneous band population.

Turning now to the current, we can express it simply in terms of the kinematical momentum and expand its expectation value in terms of Bloch states,

$$\begin{aligned} j(t) &= -\langle\psi^{(g)}(t)|\hat{p}^{(g)}_{kin}|\psi^{(g)}(t)\rangle \\ &= -\sum_n \int_{BZ} dk \left|c^{(g)}_{nk}\right|^2 \langle\phi_{nk}|\hat{p}^{(g)}_{kin}|\phi_{nk}\rangle \\ &\quad - \sum_{n,n'\neq n} \int_{BZ} dk c^{*(g)}_{nk} c^{(g)}_{n'k} \langle\phi_{nk}|\hat{p}^{(g)}_{kin}|\phi_{n'k}\rangle, \end{aligned} \tag{13}$$

noting that in the velocity gauge the kinematical momentum is $\hat{p}^{(g)}_{kin} = \hat{p} + A^{(g)}$, where $\hat{p}$ refers to the *canonical* momentum. The summation over all basis states has been split into a summation over terms involving the same band indices (intraband) and a summation over terms involving different band indices (interband). Figure 2(b) shows the interband current, so defined, as calculated in the velocity (orange) and length (blue) gauges. Although it seems reasonable to use this decomposition as a definition of interband and intraband currents, this formulation again proves to be problematic in close analogy to the above treatment of band populations.

Figure 2(b) shows the interband current, defined as the second summation in Eq. (13), as calculated in the velocity (orange) and length (blue) gauges. As in the case of the instantaneous conduction-band population, the two calculations give very different results. We note that the corresponding intraband term in the velocity gauge (not shown) is nothing but the vector potential with its sign flipped since the initial crystal momentum is $k_0 = 0$ where the group velocity in each band vanishes. However, for nonzero initial crystal momenta or in the length gauge where crystal momentum is time dependent, this first summation of Eq. (13) is a more complex function of time and can contribute to high-order harmonics. Of course, the intraband current, defined this way, is also gauge dependent.

Importantly, the total current, shown in black, is gauge independent as long as the kinematical momentum is used. Since the total current is what gives rise to the measured harmonic spectrum, there is no question that it is a physically meaningful quantity, and its gauge invariance is expected. However, as long as the treatment of interband and intraband currents depends on the gauge, it is not clear that these are physical quantities. In the next two sections, we will provide improved formulations that give reasonable and gauge-invariant predictions.

IV. BAND POPULATIONS

In this section, we propose a gauge-invariant definition for the instantaneous band populations. Our approach is to identify its corresponding Hermitian operator. We then transform it with the proper unitary operators to make it gauge independent. Before proceeding, we consider the general question of the population of *any* quantum state $|S\rangle$. The probability to find a system in this state is evidently the squared modulus of the projection of the system's state onto $|S\rangle$. Another way to say this is that it is the expectation value of a Hermitian operator (an observable), namely, the projection operator $\hat{\Pi}_S \equiv |S\rangle\langle S|$.

Likewise the operator representing band population is an operator that projects onto all the states within a given band m,

$$\hat{\Pi}_m = \int_{BZ} dq\, \hat{\Pi}_{mq} \equiv \int_{BZ} dq |\phi_{mq}\rangle\langle\phi_{mq}|, \tag{14}$$

where Π_{mq} is the projection onto a single eigenstate $|\phi_{mq}\rangle$ of the field-free Hamiltonian. Since this operator was defined without reference to a gauge or a field, we refer to it as a field-free operator. The expectation value of $\hat{\Pi}_m$ represents the band population, and Eq. (9) provides its transformation. In a gauge (g), the operator transforms as

$$\hat{\Pi}^{(g)}_{mq} = e^{-iA^{(g)}\hat{x}} \hat{\Pi}_{mq} e^{iA^{(g)}\hat{x}}, \tag{15}$$

and its matrix elements, needed to compute the expectation value, in the field-free basis are

$$\begin{aligned} \langle\phi_{nk}|\hat{\Pi}^{(g)}_{mq}|\phi_{n'k'}\rangle &= \langle\phi_{nk}|e^{-iA^{(g)}\hat{x}}|\phi_{mq}\rangle\langle\phi_{mq}|e^{iA^{(g)}\hat{x}}|\phi_{n'k'}\rangle \\ &= U^{\dagger}_{mn}(q,k) U_{mn'}(q,k'). \end{aligned} \tag{16}$$

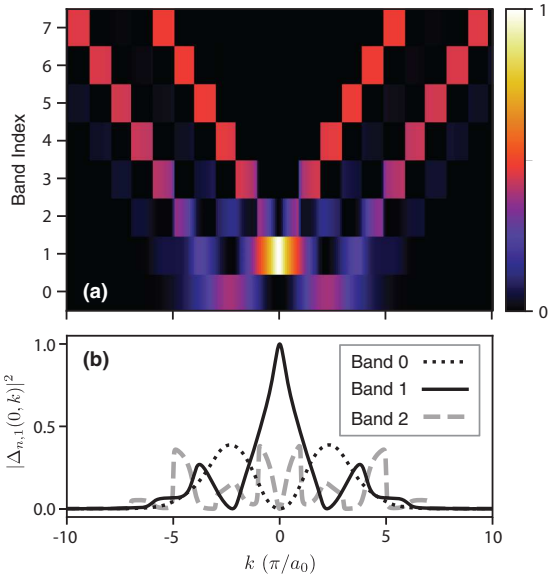

FIG. 3. Squared modulus of the functions $\Delta_{n,1}(0,k)$, plotted over ten Brillouin zones of reciprocal space for (a) the lowest seven bands and (b) for the lowest three bands. These indicate the degree to which each periodic function at $k=0$ is required to represent a wave function with crystal momentum k in band 1.

The matrix elements of the transformation operator can be shown to be

$$U_{mn}(q,k) = \delta(k + A^{(g)} - q)\Delta_{mn}(k + A^{(g)}, k), \tag{17}$$

where we have introduced the function,

$$\Delta_{nm}(k_1,k_2) \equiv \langle u_{nk_1} | u_{mk_2} \rangle, \tag{18}$$

which is the overlap integral of the periodic parts of the Bloch wave functions within one unit cell. Although the total wave-functions $|\phi_{nk}\rangle$ are all mutually orthogonal, this is not true for the periodic parts $|u_{nk}\rangle$. Whenever $k_1 = k_2$, the function $\Delta_{nm}(k_1,k_2)$ reduces to a Kronecker δ function δ_{nm} but not otherwise. This is a statement of the fact that, at a particular value of the crystal momentum $k = k_0$, the periodic functions form a complete orthonormal set $u_{nk_0}(x)$ within the Hilbert space of a single unit cell. But a different choice of k leads to a different set of functions, which will be mutually orthogonal but need not be orthogonal to the functions of the first set. This can be seen in Fig. 3, which shows $|\Delta_{n,1}(0,k)|^2$ as a function of k for different bands n. At $k=0$, $\Delta_{11}(0,0)=1$, whereas all other matrix elements are zero. However, as k departs from zero, neighboring bands become important [Fig. 3(b)], and as k increases (over several Brillouin zones), higher-lying bands have the largest contributions [Fig. 3(a)].

The Δ functions of Eq. (18), pictorially represented in Fig. 3, have been used previously in the solid-state literature [34]. They give a sense of how many bands are required at one k point (e.g., the Γ point) to express the periodic part of the wave function at a different point in reciprocal space. In this sense, they provide a connection between the two gauges: The many occupied bands at a single fixed k in the velocity-gauge map onto a smaller number of bands at a different $k + A(t)$ in the length gauge. Even in the case of adiabatic evolution in the length gauge where population is not transferred between bands, the motion of the charge in k space maps onto increasingly high-lying bands in the velocity gauge (see Appendix B).

From the Dirac δ function of Eq. (17), we immediately see that in the velocity gauge the operator that reports the population of the state with crystal momentum q in band m involves matrix elements with a different crystal momentum $q - A^{(g)}$ and may involve matrix elements in all bands. This is why band populations *appear* to be very different when calculated in the two gauges.

Finally, the matrix elements of the band projection operator, found by integrating the wave-vector q over one Brillouin zone, are

$$\left[\hat{\Pi}_m^{(g)}\right]_{nn',kk'} = \Delta^*_{mn}(k + A^{(g)}, k)\Delta_{mn'}(k + A^{(g)}, k)\delta(k - k'). \tag{19}$$

The expectation value of this projection operator represents our proposed formulation of instantaneous band populations. Whenever $A^{(g)} = 0$, as is always the case in the length gauge, this expression is simple since $\Delta^*_{mn} \to \delta_{mn}$ and $\Delta_{mn'} \to \delta_{mn'}$, making the operator diagonal with nonzero elements only in the subspace with band-index m. For nonzero vector potentials, however, the operator is nontrivial, and it mixes different bands.

Figure 4(a) shows the conduction-band population calculated using Eq. (19) in the velocity gauge (dashed orange) and length gauge (filled blue). The two calculations overlap exactly, showing that this definition indeed gives a gauge-invariant value of the instantaneous band population. The conduction-band population exhibits sharp peaks at the vector potential zeros (near the peaks of the electric field), shown more clearly in Fig. 4(b). The sharpness of these peaks is in part due to the fact that the valence band is only occupied at a single value of k. A filled valence band will lead to broader transient peaks in the conduction-band population. The maximum transient population transfer is about 5%, much lower than the 40% described by the previous velocity-gauge calculation of Fig. 2(a). We also note that, since the transformation operator for the length gauge is the identity operator, the length-gauge calculations of Figs. 4(a) and 2(a) are identical. We will revisit this fact in Sec. VI.

V. INTERBAND AND INTRABAND CURRENTS

Having considered the band populations during the pulse and the closely related projection operators, we are in a position to revisit the question of interband and intraband currents. As before, we start by identifying a Hermitian operator and then determine its gauge-dependent transformation. To do this, we again make use of projection operators to define the field-free operators,

$$\hat{j}_{ra} = -\sum_n \hat{\Pi}_n \hat{p}_{\rm kin} \hat{\Pi}_n, \tag{20}$$

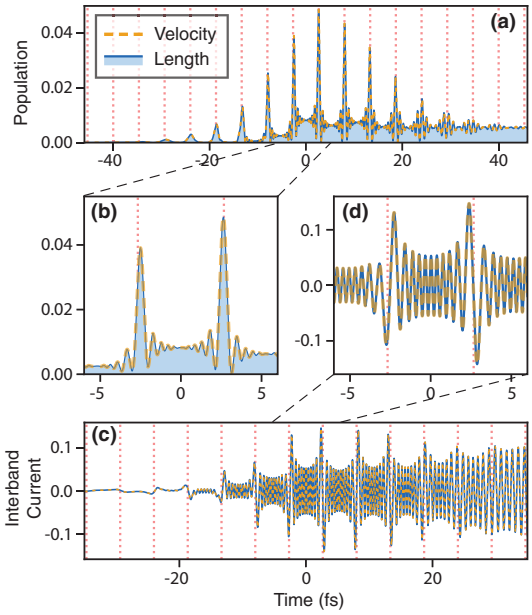

FIG. 4. Gauge-invariant dynamics. (a) Conduction-band population, defined using Eq. (19), as a function of time for velocity and length gauge, which overlap. (b) Magnified view of the conduction-band population, showing transient peaks at the vector potential zeros, as well as high-frequency oscillations. (c) Interband current, defined using Eq. (25), as a function of time for velocity and length gauge. (d) Magnified view of interband current showing that the two gauges agree within numerical accuracy.

and

$$\hat{j}_{er} = -\sum_{n,n'\neq n} \hat{\Pi}_n \hat{p}_{\rm kin} \hat{\Pi}_{n'}. \tag{21}$$

The expectation values of these operators, in the absence of any applied fields, reproduce precisely the two summations shown in Eq. (13). However, when a field is applied, a gauge must be chosen and the operators transformed appropriately. The transformation to the length gauge is, again, trivial and leaves the decomposition unchanged. However, when transforming the operator to the velocity gauge, we must transform not only the momentum operator, but also the projection operators. By simply dividing the current according to the terms shown in Eq. (13), we perform the required transformations on the momentum operator ($\hat{p}^{(g)} = \hat{p} + A^{(g)}$) and the wave functions [Eq. (7)], but we fail to take into account the transformation of the projection operators.

The gauge-transformed intraband current operator is

$$\hat{j}^{(g)}_{ra} = -\sum_{m} \iint_{BZ} dq\, dq' \hat{\Pi}^{(g)}_{mq}(\hat{p} + A^{(g)})\hat{\Pi}^{(g)}_{mq'}. \tag{22}$$

Its matrix elements are

$$\left[\hat{j}^{(g)}_{ra}\right]_{nn',kk'} = -\sum_{mll'} \Delta^*_{mn}\Delta_{ml}\Delta^*_{ml'}\Delta_{mn'} \times [p_{ll'}(k) + \delta_{ll'}A^{(g)}]\delta(k-k'), \tag{23}$$

where the arguments of the functions Δ are understood to be $\Delta_{ab} \equiv \Delta_{ab}(k + A^{(g)}, k)$. As before, the Δ functions come from the gauge-transformed projection operators and mix the bands whenever the vector potential is nonzero.

Likewise, for the interband current, we have

$$\hat{j}^{(g)}_{er} = -\sum_{m,m'\neq m} \iint_{BZ} dq\, dq' \hat{\Pi}^{(g)}_{mq}(\hat{p} + A^{(g)})\hat{\Pi}^{(g)}_{m'q'}, \tag{24}$$

whose matrix elements are

$$\left[\hat{j}^{(g)}_{er}\right]_{nn',kk'} = -\sum_{\substack{mm'\\ ll'}} \Delta^*_{mn}\Delta_{ml}\Delta^*_{m'l'}\Delta_{m'n'} \times [p_{ll'}(k) + \delta_{ll'}A^{(g)}]\delta(k-k'), \tag{25}$$

where the summation omits terms with $m = m'$. Figures 4(c) and 4(d) show the interband current calculated using Eq. (25) in the velocity gauge (dashed orange) and length gauge (solid blue). Here again, the agreement between the two calculations shows that our definition is gauge invariant.

VI. DISCUSSION

We have proposed new formulations for the interband and intraband currents as well as the instantaneous band populations. This was done by identifying Hermitian operators corresponding to each of these and then applying a gauge-dependent unitary transformation. We have shown that the resulting operators give gauge-invariant predictions for these quantities, providing a possible resolution to the issue of gauge dependence. In addition to this, our formulation allows all of these quantities to be computed from any gauge. In particular, the velocity gauge may present advantages regarding computation in some cases [25].

The harmonic spectrum for the strongly driven Mathieu potential, calculated entirely in the velocity gauge, is shown in Fig. 4. The total current (black line) displays the previously discussed double-plateau. The difficulty in retrieving interband and intraband information was noted by Wu *et al.* [20], who suggested an approach involving projection onto Houston states. We agree with their approach and conclusions, however, since they project onto a time-dependent basis, they effectively change gauges and derive a new equation of motion for the wave function. We discuss this further in Appendix A. Our approach allows us to consider the separation into interband (not shown) and intraband (red line) contributions entirely in the velocity gauge. Furthermore, it is possible to make finer divisions of the current. For instance, we may define the interband current between bands one and two as $\hat{j}_{12} = \hat{\Pi}_1 \hat{p}_{\rm kin} \hat{\Pi}_2 + \text{h.c.}$, whose spectrum is shown as the blue shaded region. This current accounts for the first plateau. Likewise, the summed interband currents from band one to bands three and four, $\hat{j}_{13} + \hat{j}_{14}$, shown as the pink shaded region, account for the second plateau. The relation of these plateaus to interband dynamics was previously argued based on the energy ranges at play and the intensity scaling [21,22], but here we can compute the interband dynamics directly even though our calculation is in the velocity gauge.

It is worth noting that the gauge-invariant quantities that we defined coincide with the earlier problematic definitions

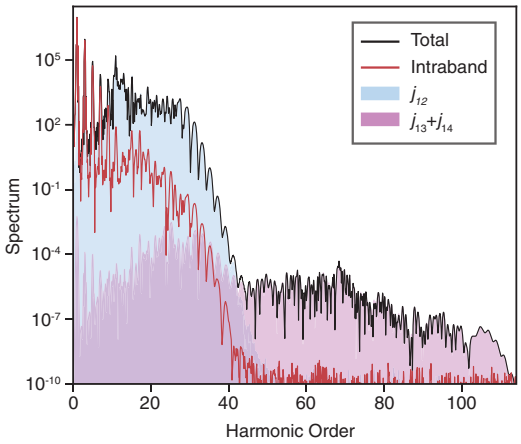

FIG. 5. Harmonic spectrum for the strongly driven Mathieu potential. The black line shows the spectrum of the total current. The red line shows that of the intraband current, which makes a negligible contribution for harmonics above the seventh order. The blue shaded region shows the spectrum of the interband current due to transitions between bands one and two. Likewise, the pink shaded region shows the spectrum of the combined interband currents due to transitions between bands one and three and bands one and four. All quantities shown are calculated in the velocity gauge.

in the length gauge (those of Sec. III). In our definitions, the field-free operators are transformed by the unitary operator $e^{iA^{(g)}x}$. However, in the length gauge, since $A^{(l)} = 0$, our approach leaves the field-free operator unchanged. But could a different choice have been made? In particular, could we not have chosen a definition such that the *velocity*-gauge operator corresponds to the field-free operator? Yes, such a choice could have been made, and the transformations of Eq. (8) would ensure gauge invariance. The resulting population operator in gauge (g) would be

$$e^{-i[A^{(g)}-A^{(v)}]x}\hat{\Pi}_{mq}e^{i[A^{(g)}-A^{(v)}]x}, \tag{26}$$

to be compared with our proposed definition Eq. (15). What, then, justifies the choice to associate the length-gauge operator with the field-free operator? Although we are not aware of any hard and fast justification for our choice, we suggest two possible arguments here, the first esthetic and the second an appeal to reasonableness.

Esthetically, the alternate definition of Eq. (26) defines the operator in gauge (g) by making reference to the vector potential in that gauge and in gauge (v) as well as referencing the field-free operator. Thus, in any gauge, this alternate definition must always refer back to the velocity gauge. In contrast, our proposed definition Eq. (15) describes the operator in gauge (g) only in terms of the field-free operator and the vector potential in that gauge. Perhaps more importantly, our definitions give reasonable answers, matching the understanding described in the literature. Figure 5 shows that our gauge-invariant formulation explains the two plateaus in the harmonic spectrum as arising from different interband currents, consistent with previous arguments. A more straightforward example is the response of the system to a constant electric field. For a sufficiently weak field, one expects an adiabatic evolution of the wave function within a single band together with Bloch oscillations in the intraband current. Appendix B shows that this behavior is captured by our definitions but not by alternative formulations, such as Eq. (26).

The questions we addressed in this article attempt to define instantaneous band-dependent quantities in the presence of a driving field. Yet the bands themselves are, in some sense, a field-free concept. A consideration of laser-dressed states is therefore an important part of this discussion. Laser-dressed states can be defined in various ways, either as instantaneous eigenstates of a Hamiltonian, which will depend on the chosen gauge, in a cycle-averaged (Floquet) way, or otherwise [18,35–37]. Here, we have not touched on these issues, aside from the Houston states, which are the instantaneous eigenstates of the velocity-gauge Hamiltonian. In atomic and molecular systems, the dressed states have played an important role in resolving unphysical anomalies in calculations, which are often gauge dependent [36,37]. We may then expect such considerations to shed further light on questions of, for example, instantaneous state populations in a laser field. We leave a detailed consideration of dressed states as they relate to gauge dependence for future study.

To conclude, we have proposed a formulation of instantaneous band populations and interband and intraband currents, which gives gauge-invariant predictions. Our approach was to define Hermitian operators corresponding to these quantities, which can be done without making reference to a field or a gauge. These field-free operators are then transformed by the well-known unitary operator that connects gauges and ensures gauge invariance. We have demonstrated numerically that this gives identical results in the velocity and length gauges and that these results are consistent with the community's use of these terms. The results give these important quantities a more rigorous definition, which, by removing the gauge dependence, establishes that these are physically meaningful.

ACKNOWLEDGMENTS

For helpful discussions and comments, we would like to thank our colleagues, M. Spanner, T. Brabec, C. McDonald, A. Staudte, D. M. Villeneuve, and P. B. Corkum. This work was supported by the Vanier Canada Graduate Scholarship program (G.E.) and by the Air Force Office of Scientific Research Multidisciplinary University Research Initiative Grant No. FA9550-15-1-0037.

APPENDIX A: RELATION TO HOUSTON STATES

Houston states have played an important role in the development of solid-state physics. They were originally proposed as approximate solutions of the length-gauge Hamiltonian in a constant electric field [38]. Later, they were employed by Krieger and Iafrate to find an analytical formulation of the TDSE in the velocity gauge [39]. This latter approach, starting from the velocity gauge, was used by Wu *et al.* to make the separation between interband and intraband currents [20]. They showed that, when the TDSE in the velocity gauge is solved in the basis of Houston states, the simple

decomposition according to band indices gives sensible results. Indeed, it has long been noted that there is a close connection between the Houston state basis and gauge transformations. In this appendix, we address this connection.

In velocity-gauge calculations, the Houston states are defined as

$$|\widetilde{\phi}_{nk_0}\rangle = e^{-iA^{(v)}x}|\phi_{nk(t)}\rangle, \tag{A1}$$

where $k(t) = k_0 + A^{(v)}$ and the vector potential is understood to be that of the velocity gauge. We make two important remarks on these states. First, we note that the crystal momentum (on the right side of the equation) acquires a time dependence, which is a consequence of the acceleration theorem. Thus, the states $|\phi_{nk(t)}\rangle$ can be thought of as "accelerated Bloch states." They are eigenstates of H_0, albeit with a time-dependent crystal momentum. Second, the phase factor that multiplies this state is precisely the unitary transformation that describes a gauge transformation $U^\dagger$. Thus, the Houston states defined by Eq. (A1) can be thought of as the velocity-gauge representation of accelerated Bloch states. Indeed, the original treatment by Houston did not include the transformation operator $e^{-iA^{(v)}x}$ since it employed the length gauge.

Considering the TDSE in the Houston-state basis, numerically, one solves for the complex amplitudes of the basis states,

$$\begin{aligned}\langle\widetilde{\phi}_{nk_0}|\psi^{(v)}\rangle &= \{\langle\phi_{nk(t)}|e^{iA^{(v)}x}\}\{e^{-iA^{(v)}x}|\psi^{(l)}\rangle\}\\ &= \langle\phi_{nk(t)}|\psi^{(l)}\rangle.\end{aligned} \tag{A2}$$

That is to say the coefficients describing the Houston states in the velocity gauge are identical to those describing accelerated Bloch states in the length gauge. It is thus not surprising that the coupled differential equations describing these coefficients end up being essentially identical to the length-gauge Schrödinger equation. Indeed, one arrives at the same differential equations in the length gauge by using an accelerated frame [12].

The approach of using a Houston-state basis does allow a decomposition into interband and intraband currents, however it involves a change in the differential equations employed, effectively requiring a return to the length gauge. In this sense, it does not directly address the issue of gauge dependence. Also, it does not take advantage of the potential computational benefits of the velocity gauge. Our approach allows the TDSE to be solved entirely in the velocity gauge using the field-free basis and still allows an unambiguous determination of interband and intraband currents. Furthermore, by defining quantities as Hermitian operators, we provide a more rigorous formulation, which is equally valid in any gauge.

APPENDIX B: DESCRIPTION OF BLOCH OSCILLATIONS IN THE VELOCITY GAUGE

The gauge-invariant definitions that we have proposed are chosen by first identifying the Hermitian operators corresponding to the observables of interest. This does not require us to think about a gauge or even a field for that matter: Currents or band populations are quantities that can be associated with the state of a system even in the absence of a field. Once these Hermitian operators are defined, gauge invariance comes from the unitary transformation of Eq. (9). This is the thought process that leads to the definitions in Eqs. (15), (22), and (24). However, as noted above, the choice of a gauge-invariant definition based on a field-free operator is not unique. In this appendix, we use the simple case of Bloch oscillations to argue that our proposed definitions coincide with the commonly accepted and discussed behaviors of band populations and currents.

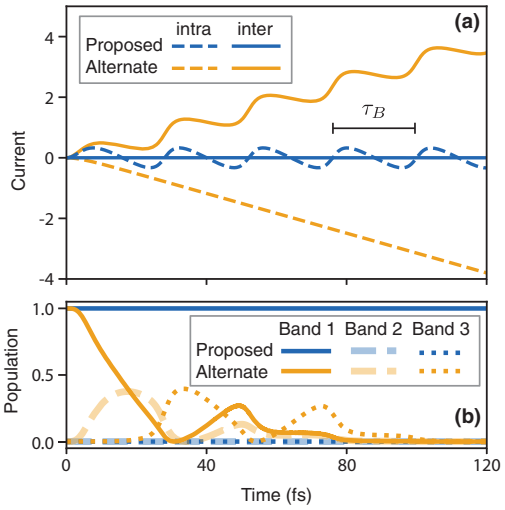

FIG. 6. Dynamics of the Mathieu potential in a static electric field, comparing our proposed definitions (in blue) with the alternate definitions of Eqs. (26), (B1), and (B2) (in orange). (a) Interband and intraband currents. Bloch oscillations can be seen, and the Bloch period is shown. (b) Band populations as a function of time. In the proposed definition, the population remains in band 1 throughout, reflecting the adiabatic evolution of the state.

The definitions that we propose cause the length-gauge operator to be equal to the field-free operator. An alternate definition for the instantaneous band population is described by Eq. (26), which instead causes the velocity-gauge operator to coincide with the field-free operator. One can likewise put forward an alternate definition for the intraband current,

$$e^{-i(A^{(g)}-A^{(v)})\hat{x}}\,\hat{j}_{ra}\,e^{i(A^{(g)}-A^{(v)})\hat{x}}, \tag{B1}$$

and for the interband current,

$$e^{-i(A^{(g)}-A^{(v)})\hat{x}}\,\hat{j}_{er}\,e^{i(A^{(g)}-A^{(v)})\hat{x}}. \tag{B2}$$

All of these alternate definitions also give gauge-invariant answers. However, the dynamics they describe do not match common expectations for an electron in a constant electric field. In a constant electric field, one expects an electron to evolve adiabatically within a single band (for a sufficiently low field), undergoing Bloch oscillations.

Figure 6 shows the dynamics of the Mathieu potential in a constant field, comparing our proposed definitions to the alternate definitions of Eqs. (26), (B1), and (B2). The constant field of -7.93×10^{-4} turns on exponentially with a time constant of 4.1 fs in order to avoid nonadiabatic excitation

of higher bands. The initial condition is the same as in the previous calculations, a single electron in band 1 at $k = 0$.

In Fig. 6(a), the proposed definition of the intraband (dashed blue) clearly exhibits Bloch oscillations, whereas the interband (solid blue) current is zero as expected. The current described by the alternate definitions (in orange) is noticeably different. Most importantly, the alternate definitions describe Bloch oscillations as an interband current, contrary to the community's understanding. The band populations described by our proposed definitions also match the common understanding. In Fig. 6(b), we see that the proposed definitions (blue) describe a population that remains entirely in band 1 with the other band populations remaining zero. This describes the adiabatic evolution of the electron within a single band. On the other hand, the alternate definition shows that the population moves from band 1 to bands 2 and 3 and eventually to higher-lying bands (not shown). The numerical results of Fig. 6 show that our proposed definitions give the correct results in a simple case where there is a consensus on the expected physical behavior.

[1] S. Ghimire, A. D. DiChiara, E. Sistrunk, P. Agostini, L. F. DiMauro, and D. A. Reis, Nat. Phys. **7**, 138 (2011).
[2] O. Schubert, M. Hohenleutner, F. Langer, B. Urbanek, C. Lange, U. Huttner, D. Golde, T. Meier, M. Kira, S. W. Koch, and R. Huber, Nat. Photonics **8**, 119 (2014).
[3] H. Liu, Y. Li, Y. S. You, S. Ghimire, T. F. Heinz, and D. A. Reis, Nat. Phys. **13**, 262 (2017).
[4] M. Sivis, M. Taucer, G. Vampa, K. Johnston, A. Staudte, A. Y. Naumov, D. M. Villeneuve, C. Ropers, and P. B. Corkum, Science **357**, 303 (2017).
[5] N. Yoshikawa, T. Tamaya, and K. Tanaka, Science **356**, 736 (2017).
[6] T. T. Luu, M. Garg, S. Yu. Kruchinin, A. Moulet, M. T. Hassan, and E. Goulielmakis, Nature (London) **521**, 498 (2015).
[7] G. Vampa, T. J. Hammond, N. Thiré, B. E. Schmidt, F. Légaré, C. R. McDonald, T. Brabec, and P. B. Corkum, Nature (London) **522**, 462 (2015).
[8] F. Krausz and M. Ivanov, Rev. Mod. Phys. **81**, 163 (2009).
[9] P. B. Corkum, Phys. Rev. Lett. **71**, 1994 (1993).
[10] G. Vampa, C. R. McDonald, G. Orlando, P. B. Corkum, and T. Brabec, Phys. Rev. B **91**, 064302 (2015).
[11] M. Garg, M. Zhan, T. T. Luu, H. Lakhotia, T. Klostermann, A. Guggenmos, and E. Goulielmakis, Nature (London) **538**, 359 (2016).
[12] G. Vampa, C. R. McDonald, G. Orlando, D. D. Klug, P. B. Corkum, and T. Brabec, Phys. Rev. Lett. **113**, 073901 (2014).
[13] T. J. Hammond, S. Monchocé, C. Zhang, G. Vampa, D. Klug, A. Yu. Naumov, D. M. Villeneuve, and P. B. Corkum, Nat. Photonics **11**, 594 (2017).
[14] M. Hohenleutner, F. Langer, O. Schubert, M. Knorr, U. Huttner, S. W. Koch, M. Kira, and R. Huber, Nature (London) **523**, 572 (2015).
[15] M. Taucer, T. J. Hammond, P. B. Corkum, G. Vampa, C. Couture, N. Thiré, B. E. Schmidt, F. Légaré, H. Selvi, N. Unsuree, B. Hamilton, T. J. Echtermeyer, and M. A. Denecke, Phys. Rev. B **96**, 195420 (2017).
[16] Z. Wang, H. Park, Y. H. Lai, J. Xu, C. I. Blaga, F. Yang, P. Agostini, and L. F. DiMauro, Nat. Commun. **8**, 1686 (2017).
[17] P. Földi, Phys. Rev. B **96**, 035112 (2017).
[18] C. R. McDonald, G. Vampa, P. B. Corkum, and T. Brabec, Phys. Rev. Lett. **118**, 173601 (2017).
[19] A. Sommer, E. M. Bothschafter, S. A. Sato, C. Jakubeit, T. Latka, O. Razskazovskaya, H. Fattahi, M. Jobst, M. Schweinberger, V. Shirvanyan, V. S. Yakovlev, R. Kienberger, K. Yabana, N. Karpowicz, M. Schultze, and F. Krausz, Nature (London) **534**, 86 (2016).
[20] M. Wu, S. Ghimire, D. A. Reis, K. J. Schafer, and M. B. Gaarde, Phys. Rev. A **91**, 043839 (2015).
[21] M. Wu, D. A. Browne, K. J. Schafer, and M. B. Gaarde, Phys. Rev. A **94**, 063403 (2016).
[22] L. Liu, J. Zhao, W. Dong, J. Liu, Y. Huang, and Z. Zhao, Phys. Rev. A **96**, 053403 (2017).
[23] T. Ikemachi, Y. Shinohara, T. Sato, J. Yumoto, M. Kuwata-Gonokami, and K. L. Ishikawa, Phys. Rev. A **95**, 043416 (2017).
[24] X. Liu, X. Zhu, P. Lan, X. Zhang, D. Wang, Q. Zhang, and P. Lu, Phys. Rev. A **95**, 063419 (2017).
[25] Y. C. Han and L. B. Madsen, Phys. Rev. A **81**, 063430 (2010).
[26] A. D. Bandrauk, F. Fillion-Gourdeau, and E. Lorin, J. Phys. B: At., Mol. Opt. Phys. **46**, 153001 (2013).
[27] We note that the Hamiltonian operator does not transform like the operators of other Hermitian observables. Its transformation is found by substituting the transformed wave function into the TDSE.
[28] M. S. Wismer and V. S. Yakovlev, Phys. Rev. B **97**, 144302 (2018).
[29] W. E. Lamb, R. R. Schlicher, and M. O. Scully, Phys. Rev. A **36**, 2763 (1987).
[30] K. S. Virk and J. E. Sipe, Phys. Rev. B **76**, 035213 (2007).
[31] N. Tancogne-Dejean, O. D. Mücke, F. X. Kärtner, and A. Rubio, Nat. Commun. **8**, 745 (2017).
[32] M. Schultze, E. M. Bothschafter, A. Sommer, S. Holzner, W. Schweinberger, M. Fiess, M. Hofstetter, R. Kienberger, V. Apalkov, V. S. Yakovlev, M. I. Stockman, and F. Krausz, Nature (London) **493**, 75 (2013).
[33] F. Schlaepfer, M. Lucchini, S. A. Sato, M. Volkov, L. Kasmi, N. Hartmann, A. Rubio, L. Gallmann, and U. Keller, Nat. Phys. **14**, 560 (2018).
[34] N. Marzari, A. A. Mostofi, J. R. Yates, I. Souza, and D. Vanderbilt, Rev. Mod. Phys. **84**, 1419 (2012).
[35] T. Higuchi, M. I. Stockman, and P. Hommelhoff, Phys. Rev. Lett. **113**, 213901 (2014).
[36] O. Smirnova, M. Spanner, and M. Ivanov, J. Phys. B: At., Mol. Opt. Phys. **39**, S307 (2006).
[37] O. Smirnova, M. Spanner, and M. Ivanov, J. Mod. Opt. **54**, 1019 (2007).
[38] W. V. Houston, Phys. Rev. **57**, 184 (1940).
[39] J. B. Krieger and G. J. Iafrate, Phys. Rev. B **33**, 5494 (1986).

4.3 Conclusion

One significant criticism that can be made about the article presented in the previous section is the arbitrariness of using the length gauge definition as a starting point. We lack a concrete physical argument to prefer this definition over others, aside from cultural and historical preferences. High harmonic generation was initially described in gases using the length gauge, and the three-step model emerged from it. The choice of the length gauge definition is primarily driven by the ease of drawing parallels between the mechanisms in solids and gases.

The equivalence of velocity and length gauge calculations implies that the information provided for a velocity calculation should be transformable into the information required for a length calculation. In the literature, it is generally easier to find information about the bands and their models than to obtain details about the dipole. A comprehensive length gauge calculation necessitates knowledge of the full dipole function across all $\mathbf{k}$ values. In contrast, in the velocity gauge, the momentum matrix element is needed, which can be well approximated at the high-symmetry points of the bands, thanks to $\mathbf{k} \cdot \mathbf{p}$ perturbation (assuming no degeneracy). Consequently, it should theoretically be possible to construct the dipole for all $\mathbf{k}$ using only the bands' information, which is more readily available in existing literature. However, despite attempts, I was unable to derive such a result, and this question remains an open topic for investigation.

CHAPTER 5 Wannier Picture

5.1 Introduction

To gain real-space insight into the process of high harmonic generation in solids, we need to change the tool we use to describe electrons. So far, only Bloch states have been used. Bloch states are convenient because they are the eigenstates of the crystal without an electric field. However, they are, by definition, infinite and delocalized. To gain a real-space insight, we need to use a wavefunction that is much more localized. This new wavefunction is called the Wannier state [55]. They are built from the superposition of Bloch states:

$$|\psi_{n,l}\rangle = \sqrt{\frac{a_0}{2\pi}} \int_{1^{\text{st}}\text{BZ}} \mathrm{e}^{-ikla_0} |\phi_{n,k}\rangle \,. \tag{5.1}$$

They have two quantum numbers: n for the band index and l representing the lattice index. They are essentially a simple Fourier transform of all the Bloch states. A parallel can be drawn with ultrashort pulses. To create an ultrashort laser pulse, multiple frequencies must be temporally aligned (phase-locked). The broader the range of spectral frequencies involved, the shorter the pulse can be. With Wannier states, it is similar. We need a broad range of spatial frequencies, so we take all the Bloch states in the first Brillouin zone and add them up coherently.

Phase-locking of Bloch states is a bit more complex than the ultrashort pulse counterpart. Bloch states are eigenstates of $\hat{H}_0$, and therefore, we can define them up to any phase factor without loss of generality. There exists a phase choice, a structural gauge [56], that minimizes the spread of the Wannier states. For ease of notation, I will assume that this phase choice has already been made when constructing the Bloch states. Another type of Wannier function exists, called the Maximally Localized Wannier Function (MLWF) [57, 58]. These functions don't simply add up all the Bloch states for one band; they pick up a few Bloch states from multiple bands if necessary. The appropriate Bloch states are found through a minimization procedure. This procedure can reveal complex wavefunctions like d-orbitals, which tend to split into multiple bands. In this thesis, to facilitate a parallel with the Bloch model that describes each band independently, we will only consider the Wannier functions built from one band.

Since the Bloch wavefunction respects the Bloch theorem, the Wannier functions have this translation property:

$$\psi_{n,l}(x - a_0) = \psi_{n,l+1}(x). \tag{5.2}$$

Under this definition of the Wannier state, Bloch quantities (band, dipole, etc.) can be easily re-expressed in terms of Wannier functions:

$$\langle \phi_{n,k} | \hat{O} | \phi_{n',k} \rangle = O_{n,n'}(k) = \sum_{\Delta l} o_{n,n'}^{(\Delta l)} \, \mathrm{e}^{ik\Delta l a_0}; \tag{5.3a}$$

$$\langle \psi_{n,l} | \hat{O} | \psi_{n',l+\Delta l} \rangle = o_{n,n'}^{(\Delta l)} = \frac{a_0}{2\pi} \int_{1^{\text{st}}\text{BZ}} O_{n,n'}(k) \, \mathrm{e}^{-ik\Delta l a_0}. \tag{5.3b}$$

Since Wannier states are nothing more than a Fourier transform of the Bloch states, Bloch quantities can be decomposed into Fourier series, and the coefficients of the series are the matrix elements of the same operator but projected onto a Wannier basis. With these equations, we can project the results of TDSE onto a Wannier basis and decompose the oscillating current in terms of spatial transitions. An important insight is to take Eq. 3.16 and rewrite the dipole transition moment in terms of their Fourier series: $\Xi_{c,v}(k) \to \sum_{\Delta l_i} \xi_{c,v}^{(\Delta l_i)} \, \mathrm{e}^{-ik\Delta l_i a_0}$, $\Xi_{v,c}(k) \to \sum_{\Delta l_r} \xi_{c,v}^{(\Delta l_r)} \, \mathrm{e}^{ik\Delta l_r a_0}$. This allows us to take into consideration the variability of the dipole over k into the saddle point approximation by adding the Fourier exponential into the fast oscillating phase:

$$\zeta^{(\Delta l_i, \Delta l_r)}(k_s, t_i, t_r) = \int_{t'}^{t} E_g(k(\tau)) d\tau + [k(t)\Delta l_r - k(t')\Delta l_i] a_0 + \omega t. \tag{5.4}$$

The three saddle points (t_i, t_r, k_s) become a function of $(\omega, \Delta l_i, \Delta l_r)$:

$$\frac{\partial \zeta^{(\Delta l_i, \Delta l_r)}(k_s, t_i, t_r)}{\partial t'} = E_g(k_s(ti)) + F(t_i)\Delta l_i a_0 = 0; \tag{5.5a}$$

$$\frac{\partial \zeta^{(\Delta l_i, \Delta l_r)}(k_s, t_i, t_r)}{\partial k_0} = \Delta x_c - \Delta x_v + (\Delta l_i - \Delta l_r) a_0 = 0; \tag{5.5b}$$

$$\frac{\partial \zeta^{(\Delta l_i, \Delta l_r)}(k_s, t_i, t_r)}{\partial t} = E_g(k_s(tr)) + F(t_r)\Delta l_r a_0 = \omega. \tag{5.5c}$$

The physical interpretation is the same as previously described with the

subtle difference that the electron and hole are born $\Delta l_i a_0$ away and recombine when they are $\Delta l_r a_0$ away. This has some consequence on the energy needed to cross the gap and the emitted energy because of the Stark effect.

5.2 Wannier Quasi-Classical Approach to High Harmonic Generation in Semiconductors

After presenting our work on the Wannier decomposition to Prof. Brabec and his team, they further developed the idea by solving the integrals of the harmonic spectrum, Eq. 3.16, using the saddle point approximation. Prior to their contribution, we had focused on the analysis of the saddle points themselves and their physical significance. Prof. Brabec's team had the insight to create a semi-classical model that turned out to be highly successful. Since then, I have been able to apply this model myself, as will be seen in the subsequent sections.

The semi-classical model is expressed by the following equations:

$$S(\omega) = \sum_{\Delta l_i, \Delta l_r} \xi_{v,c}^{(\Delta l_r)} \xi_{v,c}^{(\Delta l_i)} T_{i,r}(\omega) + c.c \tag{5.6a}$$

$$T_{i,r}(\omega) = \sum_{[t_i,t_r](\omega,\Delta l_i,\Delta l_r)} g(t_i + i\delta_i, t_r)\, \mathrm{e}^{-t_x}\, \mathrm{e}^{i\zeta^{(\Delta l_i,\Delta l_r)}(k_s,t_i,t_r)+i\pi/4} \tag{5.6b}$$

$$t_x = \mathrm{Im}\left[\zeta^{(\Delta l_i,\Delta l_r)}(k_s, t_i + i\delta_i, t_r)\right] \approx \sqrt{\frac{2\left(E_g(0) + F(t_i)\Delta l_i\right)^3}{\frac{d^2E_g}{dk^2}(0)F(t_i)^2}} \tag{5.6c}$$

The semi-classical model calculates the trajectory amplitude, $T_{i,r}(\omega)$, for a fixed ionization distance $\Delta l_i a_0$ and recombination distance $\Delta l_r a_0$, and weights it by the dipole at ionization and recombination for these distances. Then, all possible trajectory amplitudes are added coherently if they lead to the same harmonic. At the ionization step, the electron must tunnel ionize, captured by t_x, the tunneling rate. $g(t_i + i\delta_i)$ represents the amplitude after saddle point evaluation of the integrals. Its value for a 3D model is $g = \omega F(t_i + i\delta_i)(2\pi)^{5/2}/\sqrt{\mathbf{H}}$. $\mathbf{H}$ is the Hessian matrix; $H_{ij} = \partial^2\zeta/\partial_i\partial_j$. The semi-classical model turns out to be not only qualitatively interesting but also quantitatively successful!

In the following paper, we used a different definition for the mathematical variables. The symbols used in this thesis should be changed this way:

$$
\begin{aligned}
c_{n,k_0}(t) &\rightarrow a_n(k_0, t) \\
\Xi_{v,c}(k) &\rightarrow d_{v,c}(k) = d(k) \\
\xi_{v,c}^{\Delta l} &\rightarrow d_{\Delta l}(k) \\
\psi_{n,l}(x) &\rightarrow w_n(x - x_l)
\end{aligned}
$$

1764 Vol. 7, No. 12 / December 2020 / Optica Research Article

optica

Wannier quasi-classical approach to high harmonic generation in semiconductors

A. M. Parks,[1,2] G. Ernotte,[1,3] A. Thorpe,[1] C. R. McDonald,[1] P. B. Corkum,[1] M. Taucer,[1] and T. Brabec[1]

[1]Department of Physics, University of Ottawa, Ottawa, Ontario K1N 6N5, Canada
[2]e-mail: andrew.parks@uottawa.ca
[3]e-mail: gerno013@uottawa.ca

Received 14 July 2020; revised 27 October 2020; accepted 9 November 2020 (Doc. ID 402393); published 14 December 2020

An intuitive and complete understanding of the underlying processes in high harmonic generation (HHG) in solids will enable the development and optimization of experimental techniques for attosecond measurement of dynamical and structural properties of solids. Here we introduce the Wannier quasi-classical (WQC) theory, which allows the characterization of HHG in terms of classical trajectories. The WQC approach completes the single-body picture for HHG in semiconductors, as it is in quantitative agreement with quantum calculations. The importance of WQC theory extends beyond HHG; it enables modeling of dynamic processes in solids with classical trajectories, such as for coherent control and transport processes, potentially providing better scalability and a more intuitive understanding.

https://doi.org/10.1364/OPTICA.402393

1. INTRODUCTION

High harmonic generation (HHG) in solids was first examined theoretically [1–5] and has since been demonstrated in a wide range of materials [6–19]. This has laid the foundation for the rapid advancement of attosecond science in condensed matter [20–28], for which HHG is a fundamental process. HHG in solids has also caught attention as a source for ultrashort XUV radiation [10,28] and as a tool to measure ultrafast dynamics and structural properties, such as band structure [12] and the Berry curvature [16,17]. HHG in solids is driven by interband and intraband currents [29,30]. While the interband current is more dominant in wideband materials such as semiconductors [12], HHG in narrow-band dielectrics is driven more by the intraband current [10]. This work focuses on interband HHG in wideband materials.

Although some experimental features can be reasonably well reproduced by numerical models [31–39], a thorough understanding of all the components shaping harmonic spectra is still missing. This inhibits progress in optimizing HHG as a radiation source and in further developing HHG as a diagnostic tool.

The principal mechanism of interband HHG has been clarified by generalizing the saddle-point approach for atomic HHG [40,41] to integrate the interband current derived in the Bloch basis [30,42–45]. Electron and hole are born at the same lattice site in real space by tunnel ionization and quiver in the laser field. When they recollide at some lattice site, a harmonic photon is emitted. Its energy is equal to the bandgap at the crystal momentum of the electron–hole pair at recollision. Despite its merits, the Bloch quasi-classical model falls short of accounting for the lattice structure; quantum mechanics allows recombination of electrons and holes at different lattice sites, as was clearly demonstrated in recent work [15,43,46].

Here we develop a generalized quasi-classical approach that accounts for the lattice structure; this is achieved by transforming the interband current from Bloch to Wannier basis followed by saddle-point integration. The basis change has a substantial effect. The resulting Wannier quasi-classical (WQC) model is found to be in quantitative agreement with quantum calculations. So far, quasi-classical k-space analysis has been used to qualitatively investigate strong field effects in gases and in the condensed matter phase; quantitative agreement has not yet been demonstrated. Whether quantitative agreement can be obtained in the Bloch basis remains to be seen; however, the richer physics revealed by the WQC picture indicates that this might not be the case. The more refined WQC picture arises from the fact that the transition dipole moment enters the classical action in the exponent, and therewith, the saddle-point equations. Previously, the Wannier basis has been used in the numerical analysis of HHG [46,47]; a maximally localized Wannier basis [48] also has the advantage of providing a smooth k-space gauge for calculating the transition dipole matrix elements [47]. This is of particular importance for treating noncentrosymmetric materials that exhibit complex transition dipoles [36,44,49].

In this work, WQC and quantum calculations are compared for a 1D delta function two-band model solid in the single particle approximation (noninteracting electron–hole pair); parameters are chosen such that the dipole moment and bandgap are representative for semiconductors. The quantitative agreement with quantum calculations suggests that the WQC approach completes the single-body picture for HHG in semiconductors.

An electron and hole can ionize and recombine at different lattice sites with a probability determined by the tunneling exponent and Wannier dipole moments; birth and recombination sites are connected by classical trajectories; quantum effects are included by a quadratic expansion of the classical action about the classical trajectories. Beyond that, WQC analysis allows unprecedented insight into the real-space aspects of tunnel ionization in solids; it gives access to the tunnel ionized wave function in real space and therewith, to the birth location of the electron–hole pair. While Bloch quasi-classical analysis describes an electron–hole pair by a single trajectory, WQC analysis describes it by a swarm of weighted trajectories. The increased accuracy comes at the cost of higher computational load.

With a complete understanding of the single electron picture of HHG in two-band semiconductors, it is possible to begin looking at more complex dynamics. On a fundamental level, the WQC approach presents a novel platform from which alternative pathways can be developed for modeling noise and few electron–hole dynamics in solids; classical stochastic equations are easier to handle than quantum systems coupled to stochastic heat baths; as propagation from initial to final Wannier wave packet is done by classical trajectories, the space in between does not need to be resolved, in contrast to a full quantum approach. Thus, WQC analysis holds the promise to provide better scalability and a more intuitive understanding of quantum dynamics in semiconductors. Finally, multiband dynamics can be introduced into WQC analysis by adapting the approach developed in Ref. [18], which also showed that higher conduction bands mostly dominate higher plateaus, and to a lesser extent influence the first plateau of the harmonic spectrum.

One of the ultimate goals of HHG spectroscopy of solids is to extract structural and dynamic data from harmonic spectra. This will be very difficult without simple models. WQC analysis establishes the capacity to capture quantum dynamics in terms of classical trajectories in a reasonably quantitative fashion; this makes it suitable as a diagnostic tool for HHG spectra obtained from experiments and numerical quantum analysis.

More generally, our analysis opens an avenue for modeling quantum dynamics of wave packets by propagating classical trajectories. This is potentially relevant for a wide spectrum of applications, ranging from strong-field physics to transport phenomena [50,51] and coherent control [52,53].

2. THEORY

A. Two-Band WQC Model

Our formalism is developed for a 3D, two-band model. We first summarize the derivation of HHG in the Bloch basis [30]; it starts from the time-dependent Hamiltonian $H(t) = H_0 + \mathbf{x}\cdot\mathbf{F}(t)$; $\mathbf{F}(t)$ represents the laser field; H_0 is the unperturbed lattice Hamiltonian with Bloch eigenstates $\Phi_{m,\mathbf{k}}(\mathbf{x}) = 1/\sqrt{V}u_{m,\mathbf{k}}(\mathbf{x})\exp(i\mathbf{k}\cdot\mathbf{x})$ and with energies $E_m(\mathbf{k})$ in band m with crystal momentum $\mathbf{k}$; the band index $m = v, c$ refers to the valence and the conduction band, respectively; $u_{m,\mathbf{k}}$ is the periodic part of the Bloch function, $\langle\Phi_{m,\mathbf{k}}|\Phi_{m,\mathbf{k}}\rangle = 1$, and $\langle u_{m,\mathbf{k}}|u_{m,\mathbf{k}}\rangle = \upsilon$. Finally, $V = N\upsilon$ is the volume of the solid, with N and υ the number and volume of primitive unit cells. Hartree atomic units are used, unless otherwise noted.

In the presence of the laser field the wave function becomes time-dependent. In the length gauge it is represented as

$$\Psi(\mathbf{x}, t) = \sum_{m=v,c}\int_{\mathrm{BZ}} a_m(\mathbf{k}, t)\Phi_{m,\mathbf{k}}(\mathbf{x})d^3\mathbf{k}, \tag{1}$$

where $a_m(\mathbf{k}, t)$ are the probability amplitudes and integration is over the first Brillouin zone (BZ). As initial conditions, we choose an empty conduction band, $a_c(\mathbf{k}, t = 0) = 0$, and a filled valence band, $a_v(\mathbf{k}, t = 0) = 1/\sqrt{V_{BZ}}$, where V_{BZ} is the BZ volume. The ansatz (1) is substituted into the time-dependent Schrödinger equation, and the interband polarization and current are found to be [30]

$$\mathbf{p}_{cv}(t) = -i\int_{\mathrm{BZ}}\mathrm{d}\mathbf{k}\mathbf{d}(\mathbf{k})\int_{-\infty}^{t}\mathrm{d}t'\mathbf{F}(t')\cdot\mathbf{d}^*[\mathbf{k}(t', t)]e^{-iS(\mathbf{k},t',t)} + \mathrm{c.c.}, \tag{2a}$$

$$\tilde{\boldsymbol{j}}_{cv}(\omega) = i\omega\int_{-\infty}^{\infty}\mathrm{d}t e^{-i\omega t}\mathbf{p}_{cv}(t), \tag{2b}$$

with $S(\mathbf{k}, t', t) = \int_{t'}^{t}\varepsilon(\mathbf{k}(t'', t))\mathrm{d}t'' - i(t - t')/T_2$, T_2 the dephasing time, $\mathbf{k}(t', t) = \mathbf{k} + \mathbf{A}(t) - \mathbf{A}(t')$, with $\mathbf{A}(t)$ the vector potential satisfying $\mathbf{F} = -\partial_t\mathbf{A}$, and $\varepsilon = E_c - E_v$. Here, we have used the relation [54] $\langle\Phi_{m,\mathbf{k}}|\mathbf{x}|\Phi_{m',\mathbf{k}'}\rangle = \delta(\mathbf{k} - \mathbf{k}')[i\delta_{m,m'}\nabla_{\mathbf{k}} + \mathbf{d}_{mm'}(\mathbf{k})]$, with $\mathbf{d}_{mm'}(\mathbf{k}) = i\langle u_{m,\mathbf{k}}|\nabla_{\mathbf{k}}|u_{m,\mathbf{k}}\rangle$ the transition dipole moment. For a two-band system, we denote

$$\mathbf{d}(\mathbf{k}) = \mathbf{d}_{vc}(\mathbf{k}) = i\langle u_{v,\mathbf{k}}|\nabla_{\mathbf{k}}|u_{c,\mathbf{k}}\rangle, \tag{3}$$

and we assume a centrosymmetric system for which the diagonal elements $\mathbf{d}_{mm}(\mathbf{k})$ can be set to zero [44].

In the following, we will translate HHG, as described by the interband current of Eq. (2), from k space to real space by using Wannier functions. The Bloch and Wannier basis functions are connected by a Fourier transform according to [55]

$$u_{m,\mathbf{k}}(\mathbf{x}) = \sum_j w_m(\mathbf{x} - \mathbf{x}_j)e^{-i\mathbf{k}\cdot(\mathbf{x}-\mathbf{x}_j)}, \tag{4a}$$

$$w_m(\mathbf{x} - \mathbf{x}_j) = \frac{1}{\upsilon}\int_{\mathrm{BZ}} u_{m,\mathbf{k}}(\mathbf{x})e^{i\mathbf{k}\cdot(\mathbf{x}-\mathbf{x}_j)}\mathrm{d}\mathbf{k}. \tag{4b}$$

Here, $w_m(\mathbf{x} - \mathbf{x}_j)$ is the Wannier function of band m corresponding to the primitive unit cell at position $\mathbf{x}_j$. By virtue of Eq. (4b), the initial wave function,

$$\Psi(\mathbf{x}, 0) = \int_{\mathrm{BZ}}\mathrm{d}\mathbf{k}\Phi_{v,\mathbf{k}}(\mathbf{x})a_v(\mathbf{k}, t = 0) = w_m(\mathbf{x}), \tag{5}$$

corresponds to the Wannier function at position $\mathbf{x}_j = 0$. HHG can start from any other site $\mathbf{x}_j$. The initial Wannier function can be shifted to $\mathbf{x}_j$ by setting $a_v(\mathbf{k}, t = 0) = \exp(-i\mathbf{k}\cdot\mathbf{x}_j)$. As all lattice sites are identical, it is sufficient to investigate $\mathbf{x}_j = 0$.

In order to translate the interband current [Eq. (2)] into real space, the Bloch functions in the transition dipole moment [Eq. (3)] are replaced by the Wannier functions with the help of relation (4a). This leads to

$$\begin{aligned}\mathbf{d}(\mathbf{k}) &= \sum_{j,k}\int_{\upsilon} w_v^*(\mathbf{x} - \mathbf{x}_k)[\mathbf{x} - \mathbf{x}_j]w_c(\mathbf{x} - \mathbf{x}_j)e^{i\mathbf{k}\cdot(\mathbf{x}_j-\mathbf{x}_k)}\mathrm{d}\mathbf{x}\\ &= \sum_{j,l}\int_{\upsilon} w_v^*(\mathbf{x} - (\mathbf{x}_j + \mathbf{x}_l))[\mathbf{x} - \mathbf{x}_j]w_c(\mathbf{x} - \mathbf{x}_j)e^{-i\mathbf{k}\cdot\mathbf{x}_l}\mathrm{d}\mathbf{x}\\ &= \sum_l e^{-i\mathbf{k}\cdot\mathbf{x}_l}\int_V w_v^*(\mathbf{x} - \mathbf{x}_l)\mathbf{x}w_c(\mathbf{x})\mathrm{d}\mathbf{x} = \sum_l \mathbf{d}_l e^{-i\mathbf{k}\cdot\mathbf{x}_l},\end{aligned} \tag{6}$$

where the second line was obtained by setting $\mathbf{x}_k = \mathbf{x}_j + \mathbf{x}_l$ and by replacing summation index k with l in the first line. Also, note that performing $\sum_j$ in the second line changes the integration volume from a unit cell to the whole crystal volume. The Wannier dipole moments are equivalent to the Fourier series expansion coefficients of the Bloch dipole moment $\mathbf{d}(\mathbf{k})$. Interpreted in real space, the Wannier dipole moment $\mathbf{d}_l$ describes a transition where an electron is born l lattice cells away from the hole. Bloch and Wannier dipole moments are not unique; $\Phi_{m,\mathbf{k}} \to \Phi_{m,\mathbf{k}} \exp[i\alpha(\mathbf{k})]$ is also an eigenfunction for any real function α that is periodic in k space. Although the full equations, including the diagonal dipole elements $\mathbf{d}_{mm}$, are gauge-invariant [44,54], it is computationally advantageous to choose strongly confined Wannier basis functions [56,57] in order to keep the number of relevant lattice sites small. In the 1D examples discussed below we chose maximally localized Wannier basis functions [56] for which $\mathbf{d}_{mm} = 0$.

Inserting Eq. (6) into Eq. (2), the interband current follows as

$$\tilde{\boldsymbol{j}}_{er}(\omega) = \sum_{j,l} \left\{ \mathbf{d}_j [\mathbf{d}_l^* \cdot \mathbf{T}_{jl}(\omega)] - \mathbf{d}_j^* [\mathbf{d}_l \cdot \mathbf{T}_{jl}^*(-\omega)] \right\}$$

$$= \sum_{j,l} \left[\mathbf{P}_{jl}(\omega) - \mathbf{P}_{jl}^*(-\omega) \right], \tag{7a}$$

$$\mathbf{T}_{jl}(\omega) = \omega \int_{\mathrm{BZ}} \mathrm{d}\mathbf{k} \int_{-\infty}^{\infty} \mathrm{d}t \int_{-\infty}^{t} \mathrm{d}t' \mathbf{F}(t') e^{i\varphi(\mathbf{k},t',t,\mathbf{x}_l,\mathbf{x}_j)}. \tag{7b}$$

Here, $\varphi = -S(\mathbf{k}, t', t) - \omega t + \mathbf{k} \cdot (\mathbf{x}_l - \mathbf{x}_j) + [\mathbf{A}(t) - \mathbf{A}(t')] \cdot \mathbf{x}_l$; $\mathbf{P}_{jl}(\omega)$ represents the probability amplitude that the harmonic ω is generated by an electron–hole pair that is born with a relative distance $|\mathbf{x}_l|$ between electron and hole and later recombines with relative distance $|\mathbf{x}_j|$, and the propagator $\mathbf{T}_{jl}$ describes the evolution between $\mathbf{d}_l^*$ and $\mathbf{d}_j$.

B. Saddle-Point Integration

The integrals in Eq. (7b) are solved by saddle-point integration. The saddle-point equations,

$$\varepsilon[\mathbf{k}(t', t)] + \mathbf{F}(t') \cdot \mathbf{x}_l = 0, \tag{8a}$$

$$\varepsilon(\mathbf{k}) - \mathbf{F}(t) \cdot [\boldsymbol{\xi}(t', t) - \mathbf{x}_l] = \varepsilon(\mathbf{k}) + \mathbf{F}(t) \cdot \mathbf{x}_j = \mp\omega, \tag{8b}$$

$$\boldsymbol{\xi}(t', t) = \mathbf{x}_l - \mathbf{x}_j, \tag{8c}$$

result from $\partial\varphi/\partial\mu = 0$ with $\mu = t', t, \mathbf{k}$, respectively. The field quiver motion between times t' and t is given by the distance $\boldsymbol{\xi}(\mathbf{k}, t', t) = \int_{t'}^{t} \mathbf{v}(\mathbf{k}(t'', t))\mathrm{d}t''$, where $\mathbf{v}(\mathbf{k}) = \nabla_{\mathbf{k}}\varepsilon$ is the band velocity. Note that the classical action depends on the difference between conduction and valence band. As a result, the above quantities represent the difference between electron and hole band velocity and excursion distance. Finally, the $\mp$ in Eq. (8b) accounts for the complex conjugate term in Eq. (2b).

The set of Eq. (8) is solved for a linearly polarized laser field $\mathbf{F} = F\hat{\boldsymbol{x}}$; further, $\mathbf{A} = A\hat{\boldsymbol{x}}$ and $k_x = k$. The solutions of the saddle-point equations are denoted by $t' = t_b + i\delta$, $t = t_r$, $\mathbf{k}_s$. For $\delta \ll 1$, Eq. (8a) can be solved analytically; it determines the saddle-point momentum $\mathbf{k}_s = (k_s, k_{ys}, k_{zs}) = (A(t_b) - A(t_r), 0, 0)$, as well as

$$\delta = \sqrt{\frac{2(E_g + F(t_b)x_l)}{\beta_{xx}(0)F^2(t_b)}}, \tag{9}$$

where we have approximated the bandgap as

$$\varepsilon(\mathbf{k}) \approx E_g + \frac{1}{2}\sum_{i,j} k_i k_j \beta_{ij}(0), \tag{10}$$

with $i, j = x, y, z$; $\beta_{ij}(\mathbf{k}) = \partial^2\varepsilon/\partial k_i \partial k_j$ the inverse mass tensor; and E_g the minimum bandgap. The positive sign in Eq. (9) is chosen to obtain an exponentially decaying tunneling rate.

The two remaining saddle-point equations, (8b) and (8c), determine t_b and t_r. They have to be solved numerically for each possible birth site $\mathbf{x}_l$ and recombination site $\mathbf{x}_j$; for instance, by running through t_b and finding all $t_r(t_b)$s that fulfill Eq. (8c). From those, the pairs $[t_b, t_r](\omega)$ are selected that produce a given harmonic ω via Eq. (8b). The physical implications of the saddle-point equations are discussed at the end of this subsection.

Next, the integrand of Eq. (7b) is evaluated at the saddle point, where the small imaginary birth time determines the tunneling exponent. Further, the phase φ is expanded to second order, which gives the multivariate Gaussian integral,

$$\int_{-\infty}^{\infty} \mathrm{d}\mathbf{q} \exp((i/2)\mathbf{q}^T\mathcal{H}\mathbf{q}) = (2\pi)^{5/2}/\sqrt{-i|\mathcal{H}|}, \tag{11}$$

where $\mathbf{q} = (t', t, \mathbf{k})$, and $\mathcal{H}$ is the Hessian $\mathcal{H}_{ij} = \partial^2\varphi/\partial_i\partial_j$ with $i, j \in \mathbf{q}$. The full expression for the determinant of the Hessian is provided in Appendix A. Putting everything together, we obtain the WQC propagator,

$$\mathbf{T}_{jl} = \sum_{[t_b,t_r](\omega,\mathbf{x}_l,\mathbf{x}_j)} \mathbf{g}(t_b + i\delta, t_r) e^{-t_x} e^{-i\chi(t_b,t_r)+i\pi/4}, \tag{12a}$$

$$t_x = \mathrm{Im}[\varphi(t_b + i\delta)] \approx \frac{\sqrt{2}[E_g + F(t_b)x_l]^{3/2}}{[\beta_{xx}(0)F^2(t_b)]^{1/2}}, \tag{12b}$$

$$\chi = \int_{t_b}^{t_r} \varepsilon(A(t_b) - A(\tau))d\tau + \omega t_r + \mathbf{k}_s \cdot \mathbf{x}_j, \tag{12c}$$

where $\mathbf{g} = \omega\mathbf{F}(t_b + i\delta)(2\pi)^{5/2}/\sqrt{|\mathcal{H}|}$ and to leading order the determinant from the Gaussian integral $|\mathcal{H}| \approx v_x(\mathbf{k}_s) f(t_b + i\delta, t, \mathbf{k}_s)$ [18]; see Appendix A. Further, it is convenient to split the phase in Eq. (12c) into $\chi = \chi_1 + \chi_2$, where $\chi_1 = \int_{t_b}^{t_r} \varepsilon[A(t_b) - A(\tau)]d\tau + \omega t_r$ contains the classical action and the harmonic frequency Fourier term. The second term is the Fourier term of the recombination dipole moment, $\chi_2 = \mathbf{k}_s \cdot \mathbf{x}_j$. The total probability amplitude,

$$\mathbf{P}_{jl} = e^{i\pi/4} \sum_{[t_b,t_r](\omega,\mathbf{x}_l,\mathbf{x}_j)} \left[\mathbf{g}(t_b + i\delta)\mathbf{d}_l^* e^{-t_x} e^{-i\chi_1(t_b,t_r)} \mathbf{d}_j e^{-i\chi_2(t_b,t_r)} \right], \tag{13}$$

is governed by the prefactor $\mathbf{g}$, the ionization amplitude $\mathbf{d}_l^* e^{-t_x}$, the quantum mechanical (QM) phase factor $e^{-i\chi_1}$ acquired along the classical trajectory, and the recombination amplitude $\mathbf{d}_j e^{-i\chi_2}$. For each possible birth site $\mathbf{x}_l$ and recombination site $\mathbf{x}_j$ in the lattice, the summation runs over all birth and recombination times t_r, t_b that satisfy the saddle-point conditions for a particular harmonic frequency ω.

The propagator [Eq. (12)], together with the saddle point [Eq. (8)], and the interband current [Eq. (7a)] represent the WQC description of HHG in semiconductors. They reveal a complete and detailed picture of the physical mechanisms driving HHG in real and reciprocal space, summarized in Figs. 1(a) and 1(b), respectively. The empty circles in Fig. 1(a) represent the centers

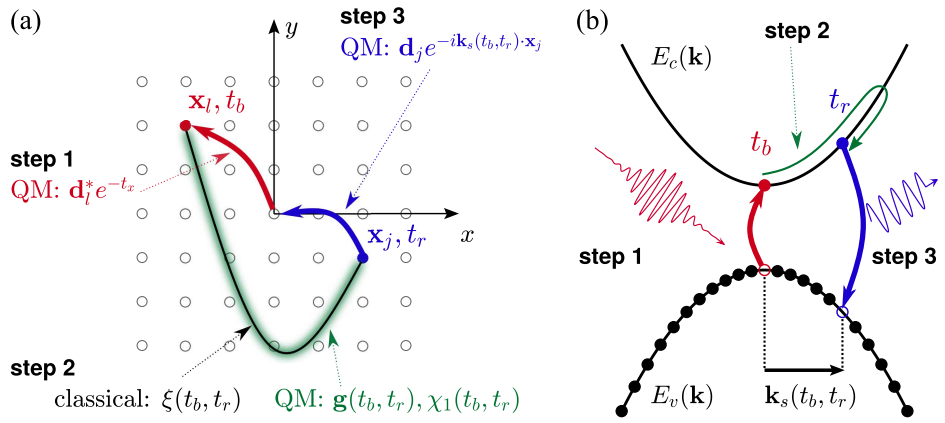

Fig. 1. Schematic of the WQC picture of interband HHG. (a) Real space picture for a model 2D lattice; empty circles denote centers of atomic unit cells at which Wannier basis functions are located. Distances shown refer to relative distance between each electron–hole pair. Classical and QM processes are indicated. The dotted arrows point to the probability amplitudes of the individual processes. In addition, the phase χ_1 picked up along the classical trajectory is indicated. HHG takes place in three steps. (1) An electron initially at the valence Wannier site $\mathbf{x}_0$ is born at $\mathbf{x}_0+\mathbf{x}_l$, creating an electron–hole pair l lattice sites apart (red arrow), with ionization amplitude $\propto \mathbf{d}_l^* \exp[-t_x]$. (2) Then it propagates in the laser field along the classical trajectory $\boldsymbol{\xi}(t_b, t_r)$; the green shaded area indicates the quasi-classical contribution $\mathbf{g}(t_b, t_r)$ that comes from the Gaussian expansion of the propagator about the classical trajectory $\boldsymbol{\xi}$. (3) Electron and hole revisit each other and recombine j lattice sites apart with $\mathbf{d}_j$ the recombination dipole (blue arrow). (b) $\mathbf{k}$-space picture, full and empty circles in valence band indicate filled states and empty states (holes), respectively; (1) electron–hole pairs are born at the Γ point ($\mathbf{k}=0$); (2) the laser field drives them in reciprocal space (green arrow); (3) they recombine at some different $\mathbf{k}_s$.

of the atomic unit cells $\mathbf{x}_l$, where $l=(l_x, l_y)$ in the 2D schematic. A Wannier basis function is located at each center. Initially, all Wannier sites of the valence band are filled. As all lattice sites are identical, it is sufficient to investigate $\mathbf{x}_l=0$; see Eq. (5) above. Following the notation of our calculation, we chose indices l, j to represent birth and recombination sites, respectively. HHG proceeds in three steps:

Step 1–creation of electron–hole pair by ionization. At birth time t_b, a valence band electron localized at lattice site $\mathbf{x}_0$ transitions to the conduction band and is localized at lattice site $\mathbf{x}_0+\mathbf{x}_l$. The tunneling probability is determined by the tunneling exponent t_x and by the Wannier dipole moment $\mathbf{d}_l^*$; see Fig. 1(a). The potential energy experienced by the created electron–hole dipole in the laser field makes the effective ionization potential $E_g+F(t_b)x_l$ birth-site-dependent; see Eqs. (8a) and (12b). In reciprocal space, the electron transitions from valence to conduction band at the Γ-point at time t_b; see Fig. 1(b). Step 1 is of a QM nature.

Step 2–electron–hole evolution in laser field. The electron–hole pair quivers in the laser field. In real space it follows the classical trajectory $\boldsymbol{\xi}(t_b, t_r)$ in Fig. 1(a) until electron and hole revisit each other and are separated by $|\mathbf{x}_j|$ at time t_r; see Eq. (8c). The propagation step is dominantly classical; of QM nature are the phase $\chi_1(t_b, t_r)$ picked up between birth and recombination time, and the quasi-classical factor $\mathbf{g}$ coming from the quadratic expansion of the classical action S about the classical trajectory. The shaded green area about the classical trajectory in Fig. 1(a) indicates the quantum correction up to the second order. In reciprocal space in Fig. 1(b), the electron–hole pair evolves from initial crystal momentum zero to saddle-point crystal momentum $\mathbf{k}_s(t_b, t_r)$, defined in Eq. (8) above.

Step 3–recombination. At time t_r, electron and hole recombine with probability amplitude $\mathbf{d}_j e^{-i\mathbf{k}_s(t_b,t_r)\cdot\mathbf{x}_j}$; see Fig. 1(a). The harmonic energy is given by the bandgap energy at $\mathbf{k}_s(t_b, t_r)$ [see Fig. 1(b)], plus the energy of the electron–hole dipole in the field $F(t_r)$; see Eq. (8b). Due to the second term, harmonics with energies somewhat larger than the maximum bandgap can be generated.

3. RESULTS

For the remainder of the paper, the WQC approach and its physical significance are explored within a 1D model system. In this case the interband current, WQC propagator, and probability amplitude reduce to scalars, namely, $\tilde{j}_{er}$, T_{jl}, and P_{jl}. Specifically, we use a 1D delta function model potential, $V(x)=\Omega\sum_{n=-\infty}^{\infty}\delta[x-(n+1/2)a]$ with unit cell size a and barrier penetration parameter Ω. This model solid represents inversion symmetric semiconductors, for which the intraband dipole moment (Berry connection) is zero in a maximally localized Wannier basis. Details of the delta function model are given in Appendix B. For the investigated parameters, the bandgap is well approximated by the nearest neighbor dispersion $\varepsilon(k)=E_g+\Delta[1-\cos(ka)]$, where E_g is the minimum bandgap and 2Δ represents the bandwidth. We chose $a=7$ and considered two values $\Omega=0.5,\ 1.5$ to model a weakly and tightly bound semiconductor, respectively. The corresponding bandgap parameters are $E_g=0.141,\ 0.269$ and $\Delta=0.269,\ 0.17$. Finally, for all runs we use a dephasing time $T_2=T_0/2$ so that only returns within a single cycle are relevant.

In Fig. 2 the exact (QM) harmonic spectrum, as obtained from numerical integration of Eq. (2), is compared with the Wannier quasi-classical solution: Eqs. (7a), (8), (9), and (12a). For the exact approach, we use $F(t)=F_0\sin(\omega_0 t)\exp(-(t/\tau)^2)$, where F_0 is the maximum field strength, and the pulse duration, $\tau=40\,T_0$, is long enough to approach the continuous wave (cw) limit; ω_0 is the laser center frequency, and $T_0=2\pi/\omega_0$ denotes the optical

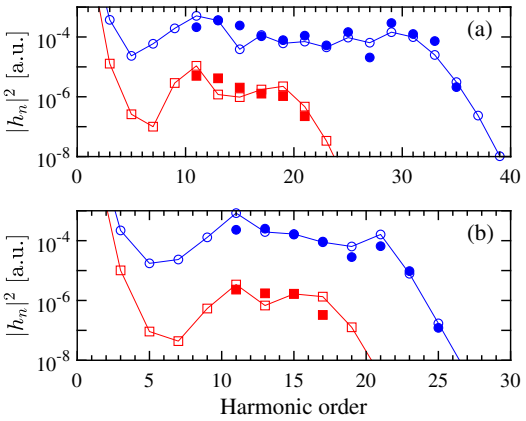

Fig. 2. Harmonic yield $|h_n|^2$ versus harmonic order n; $a = 7$, $T_2 = T_0/2$. (a)–(b) Empty blue circles with lines (exact) and filled blue circles (WQC) refer to $\Omega = 0.5$, $\omega_0 = 0.01425$ ($\lambda = 3.2$ μm), and $F_0 = 0.0025$ in (a) and $F_0 = 0.0015$ in (b); empty red squares connected by lines (exact) and filled red squares (WQC) refer to $\Omega = 1.5$, $\omega_0 = 0.0285$ ($\lambda = 1.6$ μm), and $F_0 = 0.008$ in (a) and $F_0 = 0.005$ in (b); lines are used to guide the eye.

cycle. For the highest field strength considered, an electron born at the Γ point explores only ∼60% of the BZ and does not reach the next bandgap at the edge of the BZ to transition to the second conduction band; this justifies the approximation to include only two bands. We plot the harmonic intensity $|h_n|^2 = \int_{\omega_-}^{\omega_+} d\omega |\tilde{j}_{er}(\omega)|^2$ integrated over the frequency interval $\omega_\pm = (n \pm 1/2)\omega_0$.

For the WQC calculation, we assume the cw limit, $F(t) = F_0 \sin(\omega_0 t)$, in order to facilitate interpretation of the results. Equation (12a) has been derived for finite pulses employing the Fourier transform. For a transition to the cw limit, the Fourier transform has to be replaced by a Fourier series; as a result, $\omega \to n\omega_0$, prefactor $g \to g/(2\pi T_0)$, where the $1/(2\pi)$ comes from the 1D nature of our model. The harmonic yield becomes $|h_n|^2 = |\tilde{j}_{er}(n\omega_0)|^2$ with T_{jl} given by the WQC propagator [Eq. (12a)].

In Fig. 2, the blue empty circles (exact) and blue filled circles (WQC) refer to results for the weakly bound model semiconductor, with $\Omega = 0.5$, and $\omega_0 = 0.01425$. Red empty squares (exact) and red filled squares (WQC) refer to the tightly bound semiconductor, with $\Omega = 1.5$, and $\omega_0 = 0.0285$. Plots with the same symbols in Figs. 2(a) and 2(b) correspond to the same values of Ω and ω_0, but differ in F_0.

The WQC results are only plotted above the minimum bandgap, as the quasi-classical analysis is limited to processes for which an electron is actually born in the conduction band. Below the minimum bandgap, virtual processes dominate; in this range, the intraband current can have a substantial contribution that is not shown here.

The WQC approach agrees well with the exact solution, with most data points being off by less than a factor of 2. Even the first 1–2 cutoff harmonics are described fairly well, which demonstrates that they are of quasi-classical origin. The good agreement allows us to interpret semiconductor quantum dynamics such as ionization, electron/hole transport, and HHG in terms of classical trajectories. The quantum contributions to HHG are captured

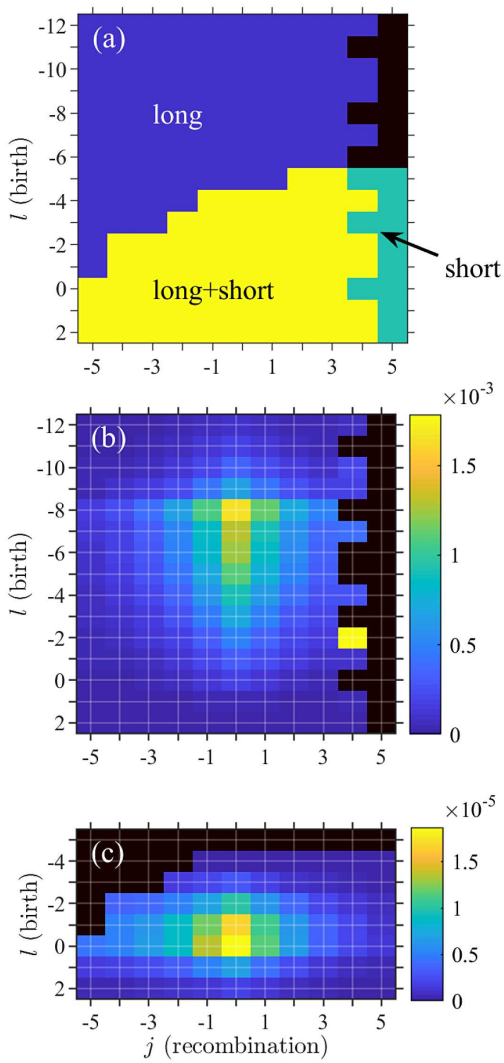

Fig. 3. Contribution of the long and short classical trajectories to the probability amplitude $|P_{jl}|$ for harmonic order $n = 15$ in a wide-band semiconductor; parameters $a = 7$, $\Omega = 0.5$, $\omega = 0.01425$, and $F_0 = 0.0025$ corresponding to filled blue circles in Fig. 2(a). (a) depicts the combinations of birth (l) and recombination (j) site indices for which each trajectory exists and contributes to P_{jl}; black regions indicate no solution. (b) shows the contribution of the long trajectory to $|P_{jl}|$, while (c) shows the contribution from the short trajectory. Note that the values of the color scale differ by 2 orders of magnitude in (b) and (c).

by the tunneling exponent t_x, by the pre-exponential factor g in Eq. (12a), and by the Wannier dipole moments in Eq. (7).

A few points disagree by a larger factor of up to 6. In particular, Fig. 2(a) shows that the WQC result for harmonic $n = 15$ exhibits larger discrepancy for the weakly bound semiconductor ($\Omega = 0.5$) compared to the more tightly bound semiconductor ($\Omega = 1.5$). The reason for this behavior is identified in Fig. 3 and will be discussed later.

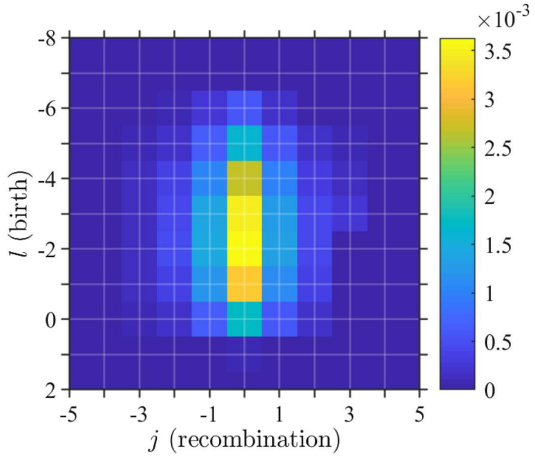

Fig. 4. Probability amplitude $|P_{jl}|$ versus birth (l) and recombination (j) site indices for harmonic order $n = 15$ in a narrowband semiconductor; parameters $a = 7$, $\Omega = 1.5$, $\omega = 0.0285$, and $F_0 = 0.008$ corresponding to filled red circles in Fig. 2(a). Here we plot the total probability amplitude $|P_{jl}|$, but note that the long trajectory is dominant; the individual contributions are similar to the behavior depicted for the wideband semiconductor in Fig. 3(b).

Numerical solution of the full saddle-point equations reveals two distinct classical trajectories that contribute to the probability amplitude P_{jl}: one long trajectory and one short. Moreover, each solution exists for only certain combinations of birth (l) and recombination (j) lattice sites. Figure 3 shows the contributions arising from the different classical trajectories for the 15th harmonic ($n = 15$) with $\Omega = 0.5$, $F_0 = 0.0025$, corresponding to the filled blue circles in Fig. 2(a). Figure 3(a) depicts the regions in the $j - l$ plane, where each trajectory contributes to $|P_{jl}(n = 15)|$. No solution exists for the dark region in the top-right, and the probability amplitude here is zero. Figures 3(b) and 3(c) show the individual contributions to the probability amplitude from the long and short trajectories, respectively. The long trajectory is dominant, as the electron–hole pair is born close to the field peak, whereas the short trajectory is born closer to the nodal point. This outweighs the effect of the short dephasing time, which favors the short trajectory. As a result, the contribution of each data point to the WQC propagator is dominantly determined by a factor $\sim g e^{-t_x}$ of a single (long) trajectory. The full probability amplitude $|P_{jl}(n = 15)|$ is essentially identical to that of Fig. 3(b).

In Fig. 4, the total probability amplitude for the 15th harmonic $|P_{jl}(n = 15)|$ is plotted as a function of birth and recombination site indices l, j for $\Omega = 1.5$, and $F_0 = 0.008$, which corresponds to the filled red squares in Fig. 2(a). For this system, the long trajectory is also dominant, and analysis of the individual contributions would reveal a picture qualitatively similar to Fig. 3.

In both Figs. 3 and 4, harmonic $n = 15$ has been selected, as the WQC result for the weakly bound semiconductor exhibits a more pronounced difference, while it agrees well for the tightly bound semiconductor. For both systems, the maximum probability is shifted towards negative birth-site indices; it is more likely for electron and hole to be born apart than at the same site. Tunnel ionization probability is determined by e^{-t_x} and by birth dipole moment d_l^*. The tunnel exponent t_x depends on the ionization potential $E_g + F(t_b)x_l$; see Eq. (12a). Thus, for the positive field, the electron–hole pair gains energy when born at increasingly negative distances, which reduces t_x. When $-x_l = E_g/F(t_b)$, t_x vanishes; in other words, the valence and conduction band levels separated by $-l$ sites align, and the electron hops from the valence to the conduction band site. The penalty to be paid is a rapidly dropping dipole moment d_l. As such, the birth-site index at which ionization is maximum is determined by a trade-off between tunnel exponent and Wannier dipole moment. The dipole elements for the parameters of Fig. 3(a) drop more slowly with increasing $|l|$ than for (b); see Appendix B. Therefore, the site of highest ionization probability is shifted more strongly towards negative l. Recombination is most probable for $j = 0$ in Figs. 3(a) and 3(b), which is consistent with previous findings [46]. The drop in probability for increasing j is due to d_j, which is why $|P_{jl}|$ extends to larger j in Fig. 3(b).

The results in Figs. 3 and 4 are displayed for birth times in the positive field cycle $0 \le t_b \le T_0/2$; the negative half-cycle would show the same picture, but mirrored about the $x-$ and $y-$ axis $(j, l \to -j, -l)$.

Recall that exact and quasi-classical results do not agree well for harmonic $n = 15$ in Fig. 2(a) ($\Omega = 0.5$). The reason is found in Fig. 3(b); disagreement is due to the point $(j, l) = (4, -2)$, which exhibits unusually high probability. We find that at this point k_s is approximately zero, and therewith $|\mathcal{H}| \approx 0$. Since $g \propto 1/\sqrt{|\mathcal{H}|}$, this leads to a large value of the prefactor g. This behavior indicates that the quadratic saddle-point expansion is no longer sufficient, and the next higher order term(s) must be included. The rules of saddle-point integration require expanding the exponent up to the first nonvanishing term. In contrast, agreement for harmonic $n = 15$ in Fig. 2(a) for $\Omega = 1.5$ is good. This is consistent with the fact that in Fig. 4, $k_s \approx 0$ does not occur in areas of high probability.

Finally, the WQC method hinges on saddle-point integration, which works well when the exponent is rapidly oscillating. This is fulfilled for wideband semiconductors with large bandwidth (Δ) and in the long wavelength limit. When transitioning to smaller Δ (dielectrics) and shorter wavelengths, saddle-point integration is expected to fail at some point. This will be subject to further research. Also, it is generally possible for transitions involving higher conduction bands to contribute to the harmonic spectrum, but this is beyond the scope of the two-band model considered here.

4. CONCLUSION

In summary, we have shown that the full single-body quantum dynamics driving HHG in wideband materials, such as semiconductors, can be quantitatively explained in terms of quasi-classical trajectory propagation. The physical insight offered by trajectory analysis will prove useful for optimization and the design of strong field and attosecond experiments and for the development of novel diagnostic applications of HHG, such as reconstruction of the dipole moment [58]. We believe that our approach presents a versatile tool for investigating open issues in strong-field solid-state physics, such as the role of noise and many-body effects in strong-field processes. Beyond that, quantitatively accurate quasi-classical analysis should be of interest for a wider range of topics in material science.

While our work is limited here to centrosymmetric materials and two-band model solids, we believe that the WQC method can contribute to understanding HHG in more complex materials. Multiband dynamics can be incorporated following the approach

outlined in Ref. [18]. Noncentrosymmetric materials exhibit an interband transition dipole phase as well as an intraband Berry phase, which lead to additional terms in the classical action. The anomalous velocity arising from the Berry phase will offset the electron–hole trajectory in the plane perpendicular to the laser polarization axis. The Bloch quasi-classical model requires the electron–hole pair to recombine at the same lattice site, thus missing important trajectories where it could recombine from nearby lattice sites.

APPENDIX A: HESSIAN

Here we provide expressions for the determinant of the Hessian $\mathcal{H}_{ij}=\partial^2\varphi/\partial_i\partial_j$ appearing in Eq. (12). Evaluation of the second derivatives yields

$$|\mathcal{H}|=\begin{vmatrix} \mathbf{F}(t')\cdot\mathbf{v}(\mathbf{k}(t',t)) & -\mathbf{F}(t)\cdot\mathbf{v}(\mathbf{k}(t',t)) & v_x(\mathbf{k}(t',t)) & v_y(\mathbf{k}(t',t)) & v_z(\mathbf{k}(t',t)) \\ +\dot{\boldsymbol{F}}(t')\cdot\mathbf{x}_l & & & & \\ -\mathbf{F}(t)\cdot\mathbf{v}(\mathbf{k}(t',t)) & \mathbf{F}(t)\cdot\mathbf{v}(\mathbf{k})-\dot{\boldsymbol{F}}(t)\cdot\mathbf{x}_j- & -v_x(\mathbf{k})+ & -v_y(\mathbf{k})+ & -v_z(\mathbf{k})+ \\ & F_i(t)D_{ij}(t',t)F_j(t) & F_i(t)D_{ix}(t',t) & F_i(t)D_{iy}(t',t) & F_i(t)D_{iz}(t',t) \\ v_x(\mathbf{k}(t',t)) & -v_x(\mathbf{k})+F_i(t)D_{xi}(t',t) & -D_{xx}(t',t) & -D_{xy}(t',t) & -D_{xz}(t',t) \\ v_y(\mathbf{k}(t',t)) & -v_y(\mathbf{k})+F_i(t)D_{yi}(t',t) & -D_{yx}(t',t) & -D_{yy}(t',t) & -D_{yz}(t',t) \\ v_z(\mathbf{k}(t',t)) & -v_z(\mathbf{k})+F_i(t)D_{zi}(t',t) & -D_{zx}(t',t) & -D_{zy}(t',t) & -D_{zz}(t',t) \end{vmatrix}, \tag{A1}$$

where the determinant is evaluated at the saddle point defined by $t'=t_b+i\delta$, $t=t_r$, $\mathbf{k}=\mathbf{k}_s$. Using linear dependence between column 2 and columns 3, 4, and 5 (see the supplement of [18]), the determinant can be simplified to

$$|\mathcal{H}|=\begin{vmatrix} \mathbf{F}(t')\cdot\mathbf{v}(\mathbf{k}(t',t))+\dot{\boldsymbol{F}}(t')\cdot\mathbf{x}_l & 0 & v_x(\mathbf{k}(t',t)) & v_y(\mathbf{k}(t',t)) & v_z(\mathbf{k}(t',t)) \\ -\mathbf{F}(t)\cdot\mathbf{v}(\mathbf{k}(t',t)) & -\dot{\boldsymbol{F}}(t)\cdot\mathbf{x}_j & -v_x(\mathbf{k})+ & -v_y(\mathbf{k})+ & -v_z(\mathbf{k})+ \\ & & F_i(t)D_{ix}(t',t) & F_i(t)D_{iy}(t',t) & F_i(t)D_{iz}(t',t) \\ v_x(\mathbf{k}(t',t)) & -v_x(\mathbf{k}) & -D_{xx}(t',t) & -D_{xy}(t',t) & -D_{xz}(t',t) \\ v_y(\mathbf{k}(t',t)) & -v_y(\mathbf{k}) & -D_{yx}(t',t) & -D_{yy}(t',t) & -D_{yz}(t',t) \\ v_z(\mathbf{k}(t',t)) & -v_z(\mathbf{k}) & -D_{zx}(t',t) & -D_{zy}(t',t) & -D_{zz}(t',t) \end{vmatrix}. \tag{A2}$$

Here, $i,j\in\{x,y,z\}$, summation is implied when indices i or j are repeated, $D_{ij}=\int_{t'}^{t}d\tau\beta_{ij}(\mathbf{k}(t'',t))$, $\beta_{ij}=\partial_{k_i}v_j(\mathbf{k})$, and $\dot{\boldsymbol{F}}(t)=\partial_t\mathbf{F}(t)$. For completeness, $|\mathcal{H}|$ is given for a general field $\mathbf{F}(t)$; for the case treated here, set $F_y=F_z=0$. To leading order $|\mathcal{H}|=v_x(\mathbf{k})\mathbf{f}(t',t,\mathbf{k})+\dot{\boldsymbol{F}}(t)\cdot\mathbf{x}_l b(t',t,\mathbf{k})$, where b, $\mathbf{f}$ are minors of $|\mathcal{H}|$. For completeness, we have included time derivatives of the laser field, which are, however, small in the long wavelength limit. As a result, the leading order term is $|\mathcal{H}|=v_x(\mathbf{k})\mathbf{f}(t',t,\mathbf{k})$.

APPENDIX B: DELTA FUNCTION POTENTIAL

The WQC approach and its physical significance are explored by means of a 1D delta-function model potential, $V(x)=\Omega\sum_{n=-\infty}^{\infty}\delta[x-(n+1/2)a]$ with unit cell size a and barrier penetration parameter Ω. For the investigated parameters, the bandgap is well approximated by the nearest neighbor approximation, $\varepsilon=E_g+\Delta[1-\cos(ka)]$, where E_g is the minimum bandgap and 2Δ represents the bandwidth.

The binding energy is determined by $2E_m=K_m^2$, where $m=v,c$ and K_m is determined by

$$\cos(ka)=\cos(K_m a)+\frac{\Omega}{K_m}\sin(K_m a). \tag{B1}$$

The wave function is given by

$$\Phi_{m,k}(x)=\sqrt{\frac{1}{a}}u_{m,k}(x)\exp(ikx)$$
$$u_{m,k}(x)=A_m(k)\left[e^{i(K_m-k)x}+r_m e^{-i(K_m+k)x}\right],$$
$$A_m(k)=1/\sqrt{1+r_m^2+2r_m\sin(K_m a)/(K_m a)},$$
$$r_m(k)=\frac{\sin[(K_m-k)a/2]}{\sin[(K_m+k)a/2]}. \tag{B2}$$

From the wave function, the Bloch dipole moment is found to be

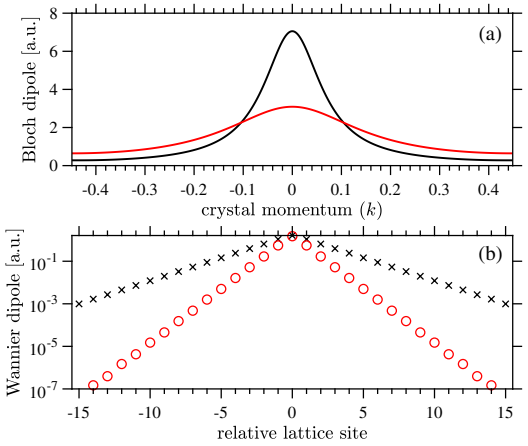

Fig. 5. (a) Bloch dipole transition elements $\mathrm{Im}[d^*(k)]$ versus k; (b) Wannier dipole transition elements d_j versus j, which represents the difference in lattice sites at which electron and hole are born. 1D model parameters, $a=7$; $\Omega=0.5$ (black); $\Omega=1.5$ (red).

$$d_{cv}(k) = d^*(k) = i\frac{2A_cA_v}{E_c - E_v} \times \left\{[(K_v - k)r_c - (K_v + k)r_v]\frac{\sin[(K_v + K_c)a/2]}{(K_v + K_c)a} + [(K_v - k) - (K_v + k)r_vr_c]\frac{\sin[(K_v - K_c)a/2]}{(K_v - K_c)a}\right\}. \tag{B3}$$

We chose $a = 7$ and $\Omega = 0.5$, 1.5 to model a weakly and more tightly bound semiconductor, respectively. The corresponding bandgap parameters are $E_g = 0.141$, 0.269 and $\Delta = 0.269$, 0.17. The Bloch dipole elements $d(k)$ and Wannier dipole elements d_j are plotted in Fig. 5. As expected, d_j drops faster for the more tightly bound model. Finally, we have chosen the coordinate center at the point of inversion symmetry that corresponds with choosing a maximally localized Wannier basis [56]. For this choice, the diagonal (intraband) dipole moments are zero, and the phase of the interband dipole moment is constant.

Funding. Air Force Office of Scientific Research (FA9550-16-1-0109).

Acknowledgment. G. Ernotte was supported by the Vanier Canada Graduate Scholarship program. T. Brabec acknowledges the support of the NSERC DG and CRC programs.

Disclosures. The authors declare no conflicts of interest.

REFERENCES

1. L. Plaja and L. Roso-Franco, "High-order harmonic generation in a crystalline solid," Phys. Rev. B **45**, 8334–8341 (1992).
2. K. A. Pronin, A. D. Bandrauk, and A. A. Ovchinnikov, "Harmonic generation by a one-dimensional conductor: exact results," Phys. Rev. B **50**, 3473–3476 (1994).
3. R.-B. Liu and B.-F. Zhu, "High-order THz-sideband generation in semiconductors," AIP Conf. Proc. **893**, 1455–1456 (2007).
4. D. Golde, T. Meier, and S. W. Koch, "High harmonics generated in semiconductor nanostructures by the coupled dynamics of optical inter- and intraband excitations," Phys. Rev. B **77**, 075330 (2008).
5. J.-Y. Yan, "Theory of excitonic high-order sideband generation in semiconductors under a strong terahertz field," Phys. Rev. B **78**, 075204 (2008).
6. S. Ghimire, A. D. DiChiara, E. Sistrunk, P. Agostini, L. F. DiMauro, and D. A. Reis, "Observation of high-order harmonic generation in a bulk crystal," Nat. Phys. **7**, 138–141 (2011).
7. B. Zaks, R. B. Liu, and M. S. Sherwin, "Experimental observation of electron-hole recollisions," Nature **483**, 580–583 (2012).
8. O. Schubert, M. Hohenleutner, F. Langer, B. Urbanek, C. Lange, U. Huttner, D. Golde, T. Meier, M. Kira, S. W. Koch, and R. Huber, "Sub-cycle control of terahertz high-harmonic generation by dynamical Bloch oscillations," Nat. Photonics **8**, 119–123 (2014).
9. M. Hohenleutner, F. Langer, O. Schubert, M. Knorr, U. Huttner, S. W. Koch, M. Kira, and R. Huber, "Real-time observation of interfering crystal electrons in high-harmonic generation," Nature **523**, 572–575 (2015).
10. T. T. Luu, M. Garg, S. Y. Kruchinin, A. Moulet, M. T. Hassan, and E. Goulielmakis, "Extreme ultraviolet high-harmonic spectroscopy of solids," Nature **521**, 498–502 (2015).
11. M. Garg, M. Zhan, T. T. Luu, H. Lakhotia, T. Klostermann, A. Guggenmos, and E. Goulielmakis, "Multi-petahertz electronic metrology," Nature **538**, 359–363 (2016).
12. G. Vampa, T. J. Hammond, N. Thiré, B. E. Schmidt, F. Légaré, C. R. McDonald, T. Brabec, and P. B. Corkum, "Linking high harmonics from gases and solids," Nature **522**, 462–464 (2015).
13. G. Vampa, T. J. Hammond, N. Thiré, B. E. Schmidt, F. Légaré, C. R. McDonald, T. Brabec, D. D. Klug, and P. B. Corkum, "All-optical reconstruction of crystal band structure," Phys. Rev. Lett. **115**, 193603 (2015).
14. H. Liu, Y. Li, Y. S. You, S. Ghimire, T. F. Heinz, and D. A. Reis, "High-harmonic generation from an atomically thin semiconductor," Nat. Phys. **13**, 262–265 (2016).
15. Y. S. You, D. A. Reis, and S. Ghimire, "Anisotropic high-harmonic generation in bulk crystals," Nat. Phys. **13**, 345–349 (2017).
16. H. B. Banks, Q. Wu, D. C. Valovcin, S. Mack, A. C. Gossard, L. Pfeiffer, R.-B. Liu, and M. S. Sherwin, "Dynamical birefringence: electron-hole recollisions as probes of Berry curvature," Phys. Rev. X **7**, 041042 (2017).
17. T. T. Luu and H. J. Wörner, "Measurement of the Berry curvature of solids using high-harmonic spectroscopy," Nat. Commun. **9**, 916 (2018).
18. A. J. Uzan, G. Orenstein, Á. Jiménez-Galán, C. McDonald, R. E. F. Silva, B. D. Bruner, N. D. Klimkin, V. Blanchet, T. Arusi-Parpar, M. Krüger, A. N. Rubtsov, O. Smirnova, M. Ivanov, B. Yan, T. Brabec, and N. Dudovich, "Attosecond spectral singularities in solid-state high-harmonic generation," Nat. Photonics **14**, 183–187 (2020).
19. G. Nbadashimiye, S. Ghimire, M. Wu, D. A. Browne, K. J. Schafer, M. B. Gaarde, and D. A. Reis, "Solid-state harmonics beyond the atomic limit," Nature **534**, 520–523 (2016).
20. M. Schultze, K. Ramasesha, C. Pemmaraju, S. Sato, D. Whitmore, A. Gandman, J. S. Prell, L. J. Borja, D. Prendergast, K. Yabana, D. M. Neumark, and S. R. Leone, "Attosecond band-gap dynamics in silicon," Science **346**, 1348–1352 (2014).
21. M. Schultze, E. M. Bothschafter, A. Sommer, S. Holzner, W. Schweinberger, M. Fiess, M. Hofstetter, R. Kienberger, V. Apalkov, V. S. Yakovlev, M. I. Stockman, and F. Krausz, "Controlling dielectrics with the electric field of light," Nature **493**, 75–78 (2013).
22. S. Neppl, R. Ernstorfer, E. M. Bothschafter, A. L. Cavalieri, D. Menzel, J. V. Barth, F. Krausz, R. Kienberger, and P. Feulner, "Attosecond time-resolved photoemission from core and valence states of magnesium," Phys. Rev. Lett. **109**, 087401 (2012).
23. S. Ghimire, G. Ndabashimiye, A. D. DiChiara, E. Sistrunk, M. I. Stockman, P. Agostini, L. F. DiMauro, and D. A. Reis, "Strong-field and attosecond physics in solids," J. Phys. B **47**, 204030 (2014).
24. A. L. Cavalieri, N. Müller, T. Uphues, V. S. Yakovlev, A. Baltuška, B. Horvath, B. Schmidt, L. Blümel, R. Holzwarth, S. Hendel, M. Drescher, U. Kleineberg, P. M. Echenique, R. Kienberger, F. Krausz, and U. Heinzmann, "Attosecond spectroscopy in condensed matter," Nature **449**, 1029–1032 (2007).
25. S. Neppl, R. Ernstorfer, A. L. Cavalieri, C. Lemell, G. Wachter, E. Magerl, E. M. Bothschafter, M. Jobst, M. Hofstetter, U. Kleineberg, J. V. Barth, D. Menzel, J. Burgdörfer, P. Feulner, F. Krausz, and R. Kienberger, "Direct observation of electron propagation and dielectric screening on the atomic length scale," Nature **517**, 342–346 (2015).
26. S. Y. Kruchinin, F. Krausz, and V. S. Yakovlev, "Colloquium: strong-field phenomena in periodic systems," Rev. Mod. Phys. **90**, 021002 (2018).
27. S. Ghimire and D. A. Reis, "High-harmonic generation from solids," Nat. Phys. **15**, 10–16 (2019).
28. J. Li, J. Lu, A. Chew, S. Han, J. Li, Y. Wu, H. Wang, S. Ghimire, and Z. Chang, "Attosecond science based on high harmonic generation from gases and solids," Nat. Commun. **11**, 2748 (2020).
29. M. Kira and S. W. Koch, *Semiconductor Quantum Optics* (Cambridge University, 2011).
30. G. Vampa, C. R. McDonald, G. Orlando, D. D. Klug, P. B. Corkum, and T. Brabec, "Theoretical analysis of high-harmonic generation in solids," Phys. Rev. Lett. **113**, 073901 (2014).
31. P. G. Hawkins and M. Y. Ivanov, "Role of subcycle transition dynamics in high-order-harmonic generation in periodic structures," Phys. Rev. A **87**, 063842 (2013).
32. P. G. Hawkins, M. Y. Ivanov, and V. S. Yakovlev, "Effect of multiple conduction bands on high-harmonic emission from dielectrics," Phys. Rev. A **91**, 013405 (2015).
33. T. T. Luu and H. J. Wörner, "High-order harmonic generation in solids: a unifying approach," Phys. Rev. B **94**, 115164 (2016).
34. N. Tancogne-Dejean, O. D. Mücke, F. X. Kärtner, and A. Rubio, "Ellipticity dependence of high-harmonic generation in solids originating from coupled intraband and interband dynamics," Nat. Commun. **8**, 745 (2017).
35. M. Wu, Y. You, S. Ghimire, D. A. Reis, D. A. Browne, K. J. Schafer, and M. B. Gaarde, "Orientation dependence of temporal and spectral

properties of high-order harmonics in solids," Phys. Rev. A **96**, 063412 (2017).
36. S. Jiang, J. Chen, H. Wei, C. Yu, R. Lu, and C. D. Lin, "Role of the transition dipole amplitude and phase on the generation of odd and even high-order harmonics in crystals," Phys. Rev. Lett. **120**, 253201 (2018).
37. M. S. Mrudul, A. Pattanayak, M. Ivanov, and G. Dixit, "Direct numerical observation of real-space recollision in high-order harmonic generation from solids," Phys. Rev. A **100**, 043420 (2019).
38. L. Li, P. Lan, X. Zhu, T. Huang, Q. Zhang, M. Lein, and P. Lu, "Reciprocal-space-trajectory perspective on high-harmonic generation in solids," Phys. Rev. Lett. **122**, 193901 (2019).
39. C. Yu, S. Jiang, and R. Lu, "High order harmonic generation in solids: a review on recent numerical methods," Adv. Phys. X **4**, 1562982 (2019).
40. M. Lewenstein, P. Balcou, M. Y. Ivanov, A. L'Huillier, and P. B. Corkum, "Theory of high-harmonic generation by low-frequency laser fields," Phys. Rev. A **49**, 2117–2132 (1994).
41. L. Keldysh, "Ionization in the field of a strong electromagnetic wave," Sov. Phys. JETP **20**, 1307–1314 (1965).
42. G. Vampa, C. R. McDonald, G. Orlando, P. B. Corkum, and T. Brabec, "Semiclassical analysis of high harmonic generation in bulk crystals," Phys. Rev. B **91**, 064302 (2015).
43. L. Yue and M. B. Gaarde, "Imperfect recollisions in high-harmonic generation in solids," Phys. Rev. Lett. **124**, 153204 (2020).
44. J. Li, X. Zhang, S. Fu, Y. Feng, B. Hu, and H. Du, "Phase invariance of the semiconductor Bloch equations," Phys. Rev. A **100**, 043404 (2019).
45. A. Chacón, D. Kim, W. Zhu, S. P. Kelly, A. Dauphin, E. Pisanty, A. S. Maxwell, A. Picón, M. F. Ciappina, D. E. Kim, C. Ticknor, A. Saxena, and M. Lewenstein, "Circular dichroism in higher-order harmonic generation: heralding topological phases and transitions in Chern insulators," Phys. Rev. B **102**, 134115 (2020).
46. E. N. Osika, A. Chacón, L. Ortmann, N. Suárez, J. A. Pérez-Hernández, B. Szafran, M. F. Ciappina, F. Sols, A. S. Landsman, and M. Lewenstein, "Wannier-Bloch approach to localization in high-harmonics generation in solids," Phys. Rev. X **7**, 021017 (2017).
47. R. E. F. Silva, F. Martín, and M. Ivanov, "High harmonic generation in crystals using maximally localized Wannier functions," Phys. Rev. B **100**, 195201 (2019).
48. N. Marzari, A. A. Mostofi, J. R. Yates, I. Souza, and D. Vanderbilt, "Maximally localized Wannier functions: theory and applications," Rev. Mod. Phys. **84**, 1419–1475 (2012).
49. S. Jiang, H. Wei, J. Chen, C. Yu, R. Lu, and C. D. Lin, "Effect of transition dipole phase on high-order-harmonic generation in solid materials," Phys. Rev. A **96**, 053850 (2017).
50. S. Datta, *Electronic Transport in Mesoscopic Systems* (Cambridge University, 1997).
51. M. Ludwig, G. Aguirregabiria, F. Ritzkowsky, T. Rybka, D. C. Marinica, J. Aizpurua, A. G. Borisov, A. Leitenstorfer, and D. Brida, "Sub-femtosecond electron transport in a nanoscale gap," Nat. Phys. **16**, 341–345 (2019).
52. M. J. Stevens, R. D. R. Bhat, X. Y. Pan, H. M. van Driel, J. E. Sipe, and A. L. Smirl, "Enhanced coherent control of carrier and spin density in a zinc-blende semiconductor by cascaded second-harmonic generation," J. Appl. Phys. **97**, 093709 (2005).
53. R. A. Muniz and J. E. Sipe, "Coherent control of optical injection of spin and currents in topological insulators," Phys. Rev. B **89**, 205113 (2014).
54. E. I. Blount, "Formalisms of band theory," in *Solid State Physics* (Elsevier, 1962), Vol. **13**, pp. 305–373.
55. H. Haug and S. W. Koch, *Quantum Theory of the Optical and Electronic Properties of Semiconductors*, 5th ed. (World Scientific, 2009).
56. W. Kohn, "Analytic properties of Bloch waves and Wannier functions," Phys. Rev. **115**, 809–821 (1959).
57. A. A. Mostofi, J. R. Yates, G. Pizzi, Y. Lee, I. Souza, D. Vanderbilt, and N. Marzari, "An updated version of wannier90: a tool for obtaining maximally-localised Wannier functions," Comput. Phys. Commun. **185**, 2309–2310 (2014).
58. Y. Zhao, S.-Y. Ma, S.-C. Jiang, Y.-J. Yang, X. Zhao, and J.-G. Chen, "All-optical reconstruction of k-dependent transition dipole moment by solid harmonic spectra from ultrashort laser pulses," Opt. Express **27**, 34392–34404 (2019).

5.3 Strong Field Dynamics and Spatial Correlations in a Maximally Localized Wannier Basis

In the following, we present a submitted but yet unpublished paper where I conducted all the calculations, reproduced the semi-classical model from the previous paper but for a different crystal, and authored the complete article.

In this paper, we utilize the Wannier picture along with the semi-classical model to delve into the three essential steps of interband harmonic generation in solids: ionization, propagation, and recombination. We also highlight the significance of the Wannier-Stark ladder in comprehending this process.

We demonstrate that the ionization asymmetry unveiled by the semi-classical model can be rapidly estimated by calculating the tunneling time for the peak field and the dipole. A competition between these two terms arises: a larger spatial step at ionization leads to a lower energy barrier and thus a shorter tunneling time due to the Wannier-Stark ladder. However, a larger spatial step results in a lower dipole owing to the reduced overlap between Wannier states. It is the competition of these two terms that creates an optimal ionization distance.

Concerning the propagation step, we unveil the trajectories by projecting the total wavefunction onto Wannier states:

$$\hat{T}(\Delta l) = \sum_{l} |\psi_{v,l}\rangle \langle \psi_{c,l+\Delta l}| \tag{5.7}$$

Finally, for the recombination step, we identify scenarios where recombination is not dominantly occurring when the electron and hole are on the same lattice site and possess maximum overlap. It seems to always be relevant for harmonics beyond the cut-off of the plateau. Also, lateral recombinations exhibit a distinct energy-time structure due to the Wannier-Stark ladder which was also demonstrated in [59].

Strong Field Dynamics and Spatial Correlations in a Maximally Localized Wannier Basis

Guilmot Ernotte,* Marco Taucer, and Paul B. Corkum
Joint Attosecond Science Laboratory, National Research Council of Canada and University of Ottawa, Ottawa, Ontario K1A 0R6, Canada

Andrew M. Parks, A Thorpe, Chris R. McDonald, and Thomas Brabec
Department of Physics, University of Ottawa, Ottawa, ON K1N 6N5, Canada
(Dated: July 22, 2023)

We investigate theoretically high harmonic generation in solids using a basis of maximally localized Wannier states. We develop a semi-classical model for interband generation which is in quantitative agreement with the full quantum simulation. Our semi-classical expression reveals a complete picture of the mechanisms shaping high harmonic generation. Both the ionization and recombination events are altered by real-space processes that are intuitively explained by the Wannier-Stark ladder. We show that the electron-hole pair correlations in this basis reveal the recolliding trajectories in solids. Finally, we show situations with a full quantum approach where recombination across lattice sites dominates high harmonic emission. This demonstrates that spatial dynamics are essential in all aspects of high harmonic generation in solids.

I. INTRODUCTION

The interaction of a strong laser field with matter can drive extremely nonlinear polarizations at petahertz frequencies [1, 2], leading to the emission of high harmonics of the driving field in the XUV region. Spectroscopy of this radiation gives information on the sub-cycle charge dynamics [3]. The discovery of high harmonic generation (HHG) in solids has extended this spectroscopy to condensed matter [4], opening a wide range of new applications. Recent work includes the observation of dynamical Bloch oscillations [5, 6], excitons [7], electron-hole dynamics [8, 9], tomography of the band structure [10, 11] and the Berry phase [12] as well as recent discussions of topological effects [13, 14].

Although most experiments can be reasonably well explained by the current numerical model [15–19], the understanding of the mechanisms underlying HHG is still incomplete. They fail to capture real-space motion like lateral tunneling ionization. Real-motion has been demonstrated theoretically in correlated materials [20] but not for single particle system at low field. This inhibits progress in optimizing HHG as a radiation source or as a diagnostic tool, for example in situations where the dipole approximation fails [21].

The most common description of the underlying mechanism is made by using a Bloch basis framework which is by definition delocalized [4–11, 14, 22–24]. While this framework gives a comprehensive picture in momentum space, it poses challenges for a real space description. Semi-classical arguments point to a recollision picture which has been corroborated experimentally [9, 24]. Despite its merits, this Bloch semi-classical model misses any ionization or recombination events of electrons and holes at different lattice sites. The need for a quantum mechanical real-space picture has led to recent studies employing a basis of Wannier states. Similar to the Foster and Boys localized molecular orbitals [25], the Wannier states are localized wavefunctions centered on one unit cell [26].

The Wannier approach in its maximally localized form [27, 28] is not yet a widespread tool to explain HHG in solids. It has been used in a few theoretical studies [14, 29–32].

We have recently presented a complete real-space picture that combined the result of the full quantum treatment and a semi-classical model [33]. Both approaches showed strong quantitative agreement between each other.

In this work, we show not only that the real-space semi-classical model can be solved in the Wannier basis, but also that its meaning is readily understood in the simple picture that the Wannier-Stark ladder provides. Namely, the semi-classical model makes use of the localized nature of the Wannier states to decompose the ultrafast polarization into its spatial components. We interpret the results by finding the saddle point of the analytical polarization [34] and we identify new spatial terms. Then, we solve analytically the polarization integrals given these saddle points which allows to find the weight of all the trajectories as we have done in the past [33]. We now do it for a different crystal showing the robustness of the method. Specifically, the agreement captures the amplitude and energy-time dispersion of the simulated spectrum as well as the trajectories of the electron-hole pairs.

To reveal the latter in a full quantum framework, we identify a new operator employing the electron-hole correlation of Wannier states. The electron-hole trajectories naturally emerge from this operator and agree with our saddle point analysis.

Finally, we identify situations where electrons and

* gerno013@uottawa.ca

holes do not recombine when their wavefunctions maximally overlap. This idea has been proposed as a possible hypothesis to explain the energy-time dispersion of the harmonics in hexagonal boron nitride, but without a quantum analysis to prove it [35]. Here, we show a situation where this happens and prove it from a full quantum treatment. We then discuss the consequences of these lateral recollisions and where we could find them experimentally.

Our approach suggests that complex quantum models can be described by propagating trajectories. This is potentially relevant for a variety of applications in strong field physics, transport phenomena [36] and coherent control [37, 38].

II. THEORETICAL BACKGROUND

Wannier states are defined as

$$|\psi_{nl}\rangle = \sqrt{\frac{a_0}{2\pi}} \int_{BZ} dk\, \mathrm{e}^{-ikla_0} |\phi_{nk}\rangle, \tag{1}$$

where l denotes the lattice site, a_0 is the lattice constant, and $|\phi_{nk}\rangle$ is a Bloch state of the same band, n, with crystal momentum k.

The Wannier states of a given band are identical aside from a shift, $\psi_{n,l+\Delta l}(x) = \psi_{nl}(x - \Delta l a_0)$. There exists a structural gauge (in this case meaning a k-dependent phase [39]) which leads to maximally localized Wannier functions (MLWF) [27, 28]. In this work, we wish to conserve the band picture and we will limit the optimization of the MLWFs to within the subspace of a single band. These MLWFs provide the most localized states that can be created, and their simple relation to Bloch states makes them ideally suited for studying spatial dynamics in the strong-field regime.

Under such strong fields, an electron's dynamic in a crystal is described by the Hamiltonian $H = H_0 + F(t)x$, where H_0 is the Hamiltonian of the unperturbed crystal and $F(t)$ is the electric field in the dipole approximation and x the position operator. We find the time evolution of the electron's quantum state by using the time-dependant Schrödinger equation (TDSE). Then, we project over the Wannier basis: $|\Psi(t)\rangle = \sum_{n,l} c_{n,l}(t)\,|\psi_{nl}\rangle$. The time evolution of the coefficients $c_{nl}(t)$ are given by

$$\begin{aligned} i\dot{c}_{n,l}(t) = &\sum_{\Delta l} \epsilon_n^{(\Delta l)}\, c_{n,l+\Delta l}(t) + F(t) l a_0 c_{n,l}(t) \\ &+ F(t) \sum_{n',\Delta l} \xi_{n,n'}^{(\Delta l)} c_{n',l+\Delta l}(t), \end{aligned} \tag{2}$$

where $\epsilon_n^{\Delta l}$ and $\xi_{n,n'}^{(\Delta l)}$ are the coefficients of the Fourier series of the energy bands $E_n(k) = \langle \phi_{n,k}|\, H_0\, |\phi_{n,k}\rangle$ and the dipoles $\Xi_{n,n'}(k) = \langle \phi_{n,k}|\, x\, |\phi_{n',k}\rangle$ respectively.

$$E_n(k) = \sum_{\Delta l} \epsilon_n^{(\Delta l)} \mathrm{e}^{ik\Delta l a_0}, \tag{3a}$$

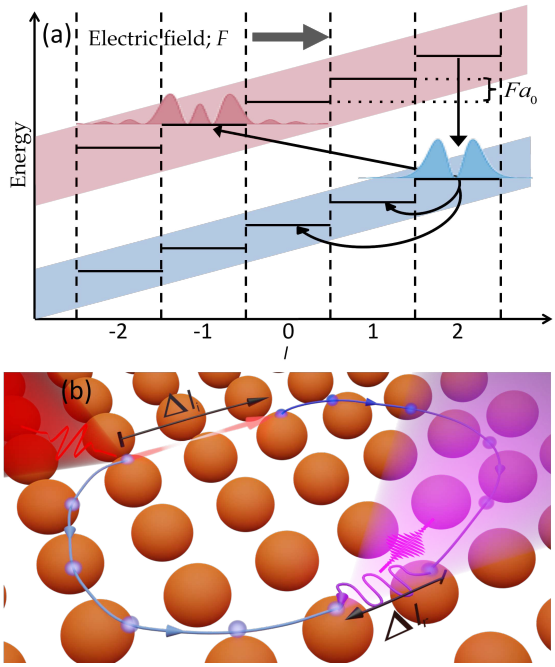

FIG. 1. (a) Energy of Wannier states as a function of lattice position. The absolute value squared of Wannier states are pictured for the valence band and l=2 (blue), and the conduction band and l=-1 (red). Under an electric field, Wannier states form a Wannier-Stark ladder. Arrows represent possible hopping between Wannier states. (b) Wannier quasi-classical model of HHG in solids. The electron-hole pair is born by tunnel-ionization Δl_i away, then is accelerated by the field, and finally recombines while they are Δl_r away .

$$\Xi_{n,n'}(k) = \sum_{\Delta l} \xi_{n,n'}^{(\Delta l)} \mathrm{e}^{ik\Delta l a_0}. \tag{3b}$$

The first term on the right-hand side (RHS) of Eq. 2 is a consequence of the crystal Hamiltonian H_0. It includes the on-site energy of the Wannier states ($\Delta l = 0$) and hopping between lattice sites of each band ($\Delta l \neq 0$), depicted as curved arrows in Fig. 1(a). The second and third terms are a consequence of the laser field. The second term expresses the l-dependent Stark shift of each Wannier state. This leads to the formation of the energy ladder of Fig. 1(a), with an energy step equal to the Bloch frequency, $\omega_B = Fa_0$, known as the Wannier-Stark ladder. Finally, the third term accounts for Berry connection and interband transitions, shown as straight arrows. The Berry connection in real space is simply a shift of the center of mass of the wavefunction within the lattice. In this paper, we will not discuss further the effect of the Berry connection and will assume that it is zero which is justifiable if the system is time and spatial symmetric with respect to the inversion operator.

The electronic dynamics sketched by Eq. 2 are the following. First, an electron in a Wannier state, which

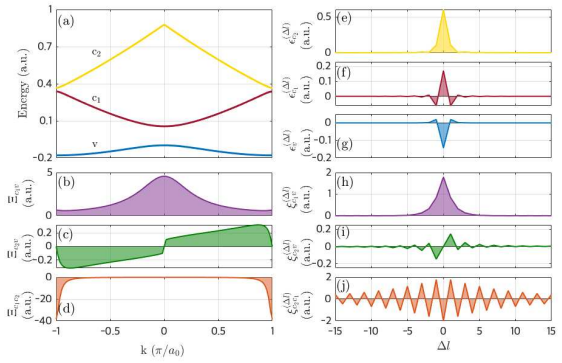

FIG. 2. (a) Valence band and first two conduction bands of the Mathieu potential. (b-d) Dipole functions between these bands. (b)&(d) are real functions while (c) is imaginary. (e-f) Coefficients of the Fourier series of the three bands. (h-j) Coefficients of the Fourier series of the dipole functions. These coefficients are used to compute intraband (e-g) and interband (h-j) coupling between different Wannier states.

is centered on one lattice position, may jump to another Wannier state in the same band without the assistance of an electric field and the probability of that jump is related to the quantity $\epsilon^{(\Delta l)}$. Second, if that jump occurs while an electric field is present the electron will emit a photon associated with the energy of that jump as depicted by the Wannier-Stark ladder in Fig. 1 (a). As long as the band is not completely filled, this is the source of what is called intraband currents and can lead to the emission of high harmonics as shown in [30] and will not be discussed further here. Third, an electron may also jump from one band to another due to the electric field and the distance of that jump is weighted by the quantity $\xi^{(\Delta l)}_{n,n'}$. This last type of transition leads to interband dipoles which are a source of high harmonic generation. We will derive later that the energy of that emission is a sum of the instantaneous band energy and the Wannier-Stark ladder.

The crystal quantities of Eqs. 3 are presented in Fig. 2 for a Mathieu potential, $V(x) = -V_0[1 - \cos(2\pi x/a_0)]$ with $V_0 = 0.37$ and $a_0 = 8$ the same parameters as [17], resulting in a semiconductor with a bandgap of 0.15. The left column sub-figures (a-d) are expressed in the well-known Bloch basis or, equivalently, as a function of k while the right column sub-figures (e-j) are the reciprocal of these quantities in a Wannier basis or equivalently as a function of Δl, the lattice separation. Because of the symmetry constraints on Bloch states [40], Wannier quantities can always be expressed as purely real functions as long as a MLWFs gauge has been chosen. Moreover, they are exponentially decreasing function in their absolute value, and hence transitions across lattice sites will decay with increasing step size due to the reduced overlap between states.

The movement of the electrons and holes in real-space means that an accelerating dipole is formed and consequently electromagnetic radiation will be emitted. The spectrum S of this radiation can be computed by taking the Fourier transform, with respect to time, of the acceleration of the dipole. For the purpose of this discussion we will only consider the interband part of this accelerated dipole [41]:

$$\begin{aligned} S_{ter}(\omega) &= \sum_{l,\Delta l} \sum_{n,n' \neq n} \\ &\mathcal{F}\left\{ \frac{d^2}{dt^2} \langle \Psi(t) | \psi_{n,l} \rangle \langle \psi_{n,l} | x | \psi_{n',l+\Delta l} \rangle \langle \psi_{n',l+\Delta l} | \Psi(t) \rangle \right\} \\ S_{ter}(\omega) &= -\omega^2 \sum_{l,\Delta l} \sum_{n,n' \neq n} \xi^{(\Delta l)}_{n,n'} \mathcal{F}\left\{ c^*_{n,l}(t)\, c_{n',l+\Delta l}(t) \right\} \end{aligned} \tag{4}$$

For the time being, we will restrict ourselves to a two-band problem ($n = v, n' = c$) and we then apply the frozen valence band approximation to find an integral expression similar to [24], but expanding all k-dependent quantities in their Fourier components and relating them to the Wannier states.

$$\begin{aligned} S_{ter}(\omega) = -\omega^2 \sum_{\Delta l_i, \Delta l_r} \xi^{(\Delta l_r)}_{vc} \xi^{(\Delta l_i)}_{vc} \int_{-\infty}^{\infty} dt \int_{\mathrm{BZ}} dk_0 \\ \times \int_{-\infty}^{t} dt' F(t') \mathrm{e}^{i\phi^{(\Delta l_i, \Delta l_r)}_{\mathrm{ter}}} + \mathrm{c.c.}, \end{aligned} \tag{5}$$

Compared to the usual expressions derived in the Bloch basis, Eq. 5 contain information relating to the spatial steps at ionization, Δl_i, and recombination, Δl_r as pictured in Fig 1(b). This spatial information is also reflected in the phases,

$$\begin{aligned} \phi^{(\Delta l_i, \Delta l_r)}_{\mathrm{ter}} = -\int_{t'}^{t} E_g(k(\tau)) d\tau \\ + \left[k(t) \Delta l_r - k(t') \Delta l_i \right] a_0 + \omega t, \end{aligned} \tag{6}$$

where $E_g(k) = E_c(k) - E_v(k)$ is the bandgap energy, $k(t) = k_0 + A(t)$ is the accelerated crystal momentum and $A(t)$ the vector potential defined such that $-dA(t)/dt = F(t)$.

To gain more insight into the spatial processes underlying harmonic emission, we solve the integral of Eq. 5 by saddle point analysis including the spatial character of transitions.

The three saddle points reveal conditions that define the dominant semi-classical dynamics,

$$E_g(k(t')) + F(t') \Delta l_i a_0 = 0, \tag{7a}$$

$$\Delta x_c - \Delta x_v + (\Delta l_i - \Delta l_r) a_0 = 0, \tag{7b}$$

$$E_g(k(t)) + F(t) \Delta l_r a_0 = \omega. \tag{7c}$$

The first saddle point, Eq. 7a, shows that the ionization process at the birth time t' can include a spatial step of Δl_i. The usual treatment of ionization, in

atoms and solids, does not include this spatial dependence and therefore has no real roots because the energy gap, $E_g(k)$, is always positive. We see here that for large fields and large ionization steps, real roots appear due to the Wannier-Stark ladder. Even in the case where they do not (that is when $F\Delta l_i a_0 < E_g(0)$), a spatial asymmetry is apparent as the imaginary time associated with ionization is reduced for $F\Delta l_i < 0$. In the extreme case, when $F = E_g/a_0$, ionization between nearest-neighbours is resonant and becomes the dominant mechanism for ionization, consistent with the interpretation of previous experiments on wide bandgap dielectrics [32, 42, 43].

The second saddle point condition, Eq. 7b, requires that the electron and hole re-encounter one another after their semi-classical trajectories (which travel Δx_c and Δx_v, respectively). Here, the condition is modified by the possibility of ionizing or recombining across lattice sites. The situation is pictured in Fig. 1(b)

The third saddle point, Eq. 7c, determines the energy emitted upon recombination at time t which can include a spatial step of Δl_r. That is, the electron-hole pair were Δl_r lattice sites apart just before recombination. The associated energy emitted is composed of two terms, a k-dependent bandgap energy and an extra term proportional to the electric field due to the Wannier-Stark ladder pictured in Fig. 1(a).

We then analytically solve the integral expression of the interband current at the saddle point of Eqs. 7 ($t = t_r$, $t' = t_i + i\delta$, $k_0 = -A(t_i)$). Then, the phase ϕ_{ter} is expanded to second-order and the resulting multivariate Gaussian integral is evaluated. A more detailed analysis of this approach can be found in [33].

$$S_{ter}(\omega) = \sum_{\Delta l_i, \Delta l_r} \xi_{v,c}^{(\Delta l_r)} \xi_{v,c}^{(\Delta l_i)} T_{i,r}(\omega) + \text{c.c.} \tag{8a}$$

$$T_{i,r}(\omega) = \sum_{[t_i,t_r](\omega, \Delta l_i, \Delta l_r)} g(t_i + i\delta, t_r)\, e^{-t_x}\, e^{i\phi_{ter}^{(\Delta l_i, \Delta l_r)}(t_i,t_r) + i\pi/4} \tag{8b}$$

$$t_x = \mathrm{Im}[\phi_{ter}^{(\Delta l_i, \Delta l_r)}(t_i + i\delta)] \approx \sqrt{\frac{2(E_g(0) + F(t_i)\Delta l_i)^3}{\frac{d^2 E_g}{dk^2}(0) F(t_i)^2}} \tag{8c}$$

where $g = \omega^2 F(t_i)(2\pi)^{3/2}/\sqrt{|H|}$ and H is the Hessian matrix of the phase ϕ_{ter} with respect to the saddle point variables. In essence, this semi-classical approach allows us to calculate all the semi-classical trajectories — that is, ionization and recombination time — leading to a fixed harmonic order including all possible spatial lateral transitions Δl_i and Δl_r as shown in Fig. 1(b). The trajectories are first weighted at ionization depending on their Wannier dipole, $\xi_{c,v}^{(\Delta l_i)}$, and tunneling time t_x. Then they accumulate a phase $\phi_{ter}^{(\Delta l_i, \Delta l_r)}(t_i, t_r)$ due to propagation and a factor g coming from the quadratic expansion of the phase around the saddle point. Finally, the trajectories are weighted by their recombination Wannier dipole matrix element, $\xi_{v,c}^{(\Delta l_r)}$ and coherently summed. The result corresponds to the spectral component of the interband current at the fixed harmonic order.

In the following sections, we will explore how these new spatial displacements affect the ionization, the propagation and recombination step.

III. IONIZATION

To demonstrate the capability of this method, we build a simulation based on the Mathieu potential whose important characteristics are presented in Fig. 2. For the moment, we limit ourselves to a two-band system. We choose a vector potential of $n_c = 50$ cycles with a $\cos^4$ envelope, $A(t) = A_0 \cos^4(\omega_0 t/2n_c)\cos(\omega_0 t)$ with $\omega_0 = 0.014$ a.u. and $A_0 = 0.22$ a.u. corresponding to a pulse of 3.2 μm and peak electric field of 0.17 V/Å. The long pulse was chosen to approach the continuous wave limit. The starting condition is a filled valence band. Finally, we solve the semiconductor Bloch equation (SBE) with a dephasing time $T_2 = \pi/\omega_0$ like in [24] to limit trajectories to one cycle. The very short T_2 is justified to compensate mesoscopic effects such as phasematching and integration of the electric field intensity distribution [44]. We then project the final results in the Wannier basis. For the semi-classical model, the introduction of T_2 means that that ϕ_{ter} gets an extra term equal to $i(t_r - t_i)/T_2$.

The results of the simulation are presented in Fig. 3(a) together with the semi-classical model of Eq. 8. The simulated spectrum is reduced to only the odd harmonics by summing all the spectral component inside one harmonic order ($n\omega_0 \pm 0.5\omega_0$). The semi-classical model matches the simulated spectrum quantitatively well, within a factor of 3 for almost all data points. The accuracy of the semi-classical model justifies the real-space picture of trajectories illustrated in Fig. 1 (b). Electrons and holes follow semi-classical trajectories modified by discrete spatial steps at birth and recombination. Figure 3(b) presents the magnitude of each of these pathways $|\xi_{v,c}^{(\Delta l_r)} \xi_{v,c}^{(\Delta l_i)} T_{i,r}(\omega)|$ for harmonic order 27 as a function of displacement at birth and recombination. It can easily be seen that for our system, the dominant recombination path is the one where electrons and holes are on the same lattice site ($\Delta l_r = 0$) consistent with the current understanding of HHG in solids. However, a recent study hinted with qualitative arguments to the possibility of recombination up to 6 lattices away in special systems like hexagonal boron nitride for the cut-off harmonics [35].

Our interpretation diverges from the current model of HHG regarding the dominant ionization path; it is not the path where the electron and hole are born on the same lattice position. Instead, the electron prefers to tunnel ionize by moving laterally. This displacement is more favorable as the Wannier-Stark ladder reduces the tunneling barrier, as shown in Fig. 1(a), but at the cost of a

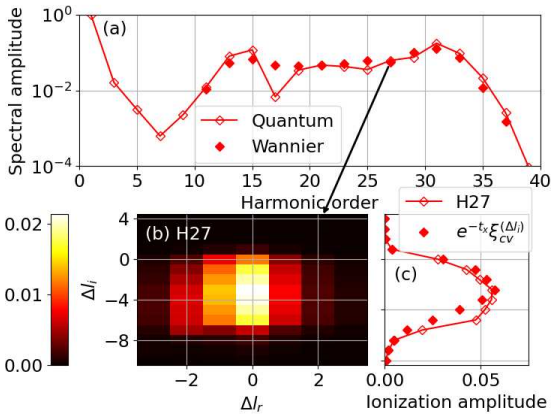

FIG. 3. (a) Interband harmonic yield as a function of harmonic order. The solid curve with open diamonds corresponds to the quantum simulation and the filled diamonds correspond to the semi-classical model. (b) Decomposition of the harmonic 27's pathways $|P_{i,r}|$ as a function of displacement at ionization and recombination for a half-cycle. (c) Ionization amplitude of the harmonic 27th as a function of displacement at ionization. The solid curve with open diamond corresponds to the integral of (b) along Δl_r and the filled diamond is the product of tunneling time and Wannier dipole. Most of the ionization structure is an interplay between lower bandgap thanks to the Wannier-Stark ladder and diminishing overlap between the wavefunctions.

weaker dipole matrix element shown in Fig. 2(h).For our system, the trade-off between these two competing factors leads to a maximum contribution from trajectories ionizing across three lattice sites, $\Delta l_i = -3$. In Fig. 3(c) we show that we can get a good estimate of this trade-off without calculating all the trajectories amplitude by comparing the product $\xi_{cv}^{(\Delta l_i)} e^{-t_x}$ versus the projection of Fig. 3(b) on the Δl_i axis. Most of the ionization structure of Fig. 3(b) is captured by the interplay of the tunneling time t_x and the Wannier dipole decomposition $\xi_{cv}^{(\Delta l_i)}$. The structure in Fig. 3(b) is not symmetric with respect to Δl_i=0 because only the trajectories occurring within the positive half-cycle are considered. The magnitude of the trajectories in the subsequent half-cycle shows the same structure but mirrored with respect to Δl_i=0 and Δl_r=0 which is consistent with the oscillating Wannier-Stark ladder interpretation, *i.e.* when the field switches polarity, the ladder also switches direction.

IV. PROPAGATION

Real-space trajectories can be retrieved from the full quantum mechanical treatment by projecting it in Wannier space. The difficulty in identifying recolliding trajectories in previous works stems from the fact that, for an initially filled valence band, the charge density associated with each band is spatially uniform throughout the light-matter interaction. Unlike in the case of atoms, there is no notion of trajectories in terms of charge densities or electron wavepackets. Nonetheless, when we consider a filled valence band, a two-body operator represents the spatial correlation between an electron in the conduction band and a hole in the valence band, as has been discussed elsewhere [7, 45]. Remarkably, in the case of non-interacting electrons, this operator is identical to a single-particle operator that is succinctly expressed in the Wannier basis as

$$\hat{T}(\Delta l) = \sum_l |\psi_{v,l}\rangle\langle\psi_{c,l+\Delta l}|. \tag{9}$$

The absolute value squared of the expected value of this operator is presented in Fig. 4(a). It shows the electron-hole separation (vertical axis) as a function of time (horizontal axis). We recognize the typical oscillations of electron density for the atomic or molecular case but this time for a solid calculation. The stripes in the electron density come from the interference between different birth times. The electronic density fades away because of the decoherence time T_2 introduced in the calculation. Mathematically, these trajectories are nothing more than the Fourier transform along k of the off-axis element of the density matrix of the system, also known as the coherence of the system, or equivalently the polarization terms of the SBE.

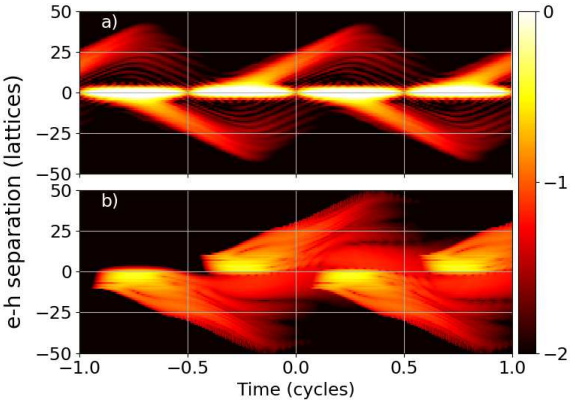

FIG. 4. Log scale color map of the correlation between electrons in the conduction band and holes in the valence band from (a) the full simulation (first term of Eq. 9) and (b) the semi-classical model (Eq. 8b weighted by $\xi_{v,c}^{(\Delta l_i)}$). Trajectories are revealed by the correlation term.

We compare these trajectories to the result from the semi-classical model by computing $T_{i,r}$ and weighting it by the correct ionization amplitude $\xi_{vc}^{(\Delta l_i)}$. The absolute value squared of this function is plotted in Fig. 4(b). There is good qualitative agreement between the two pictures of spatial dynamics. Electron-hole pairs

are born asymmetrically at each half cycle. In the full quantum calculation, the asymmetric ionization step is somewhat obscured by a large virtual population centered at $\Delta l = 0$. This virtual population is absent from the semi-classical picture; since they cannot satisfy the saddle point conditions. Fourier transforming the line $\Delta l_r = 0$, when electron and hole recombine at the same lattice site, leads to a good approximation of the harmonic spectrum. This is the case because the harmonic spectrum is dominated by electron-hole pairs recombining when their overlap is maximum as we have shown in Fig. 3(b).

V. RECOMBINATION

In contrast to the example considered in the previous section, there are situations where the harmonic spectrum is not dominated by same-site recombination. To demonstrate such a situation, we simulate the interband harmonic spectrum from the same model as before but with two differences. First, the second conduction band is reintroduced making it a three-band calculation. Second, to allow transitions from valence band to the first conduction band, then to the second conduction band, and finally recombining with the hole, the decoherence time T_2 is increased to an infinite value. Similar results can be obtained with a longer and finite $T_2 = 4\pi/\omega_0$ but we chose the former to have a flatter plateau and less sharp harmonics for readability. The resulting harmonic spectrum is shown in Fig. 5. It exhibits a previously discussed double-plateau structure [16, 17, 41, 46, 47] associated with transitions back to the valence band from the first conduction band or second conduction band. Here, we decomposed the interband spectrum into on-site ($\Delta l_r = 0$), on-site and nearest-neighbour ($|\Delta l_r| \leq 1$), and on-site to next-nearest neighbour ($|\Delta l_r| \leq 2$) recombinations. This decomposition is accomplished by limiting the sum over Δl in Eq. 4 to only these specific terms.

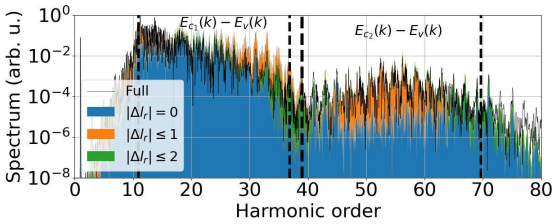

FIG. 5. Simulation of high harmonic generation for the Mathieu potential with 3 bands. Total interband spectrum and its decomposition into different spatial terms which is accomplished by considering only the terms with $|\Delta l_r| \leq 0$, 1, or 2. The dashed line represents the energy difference between the valence band and the first and second conduction bands. The first plateau is dominated by on-site recombination and the second plateau by nearest-neighbour. Harmonics beyond the cutoff are generated by large displacement at recombination.

We see that the first plateau is dominated by on-site recombinations consistent with the two-band calculation and semi-classical model shown in Fig. 3(b). However, the second plateau is surprisingly dominated by nearest-neighbour recombination. This second plateau arises from the recombination from the second conduction band to the valence band. We can see in Fig. 2(i) that the dipole in Wannier basis is precisely zero for same-site transitions. This can be counter-intuitive at first look as this is when the two wavefunctions have the maximum overlap, but this zero is a consequence of the symmetries of the wavefunctions. The valence band and second conduction band Wannier wavefunctions are both odd and therefore dipole transition is forbidden by symmetry. However, if the center of symmetry of one of these two wavefunctions is shifted by one lattice site, then the symmetry restriction is lifted. We expect that effect to be present even in real 3D solids for very high harmonics when higher bands are probed like in experiments where special caustic favors this type of transition [48].

Another piece of information we get from Fig. 5 is that harmonics beyond the cutoff seem to be generated by recombination from latice sites $\Delta l_r > 1$. Indeed, the Wannier-Stark ladder offers the opportunity to emit extra energy depending on the field strength at the time of recombination according to Eq. 7c.

To test this aspect of our model, specifically in the second plateau, we do a Gabor transformation of the interband polarization only including $\Delta l_r = \{1, 0, -1\}$, the sliding Gaussian window size is 1/4th of a cycle ($1/e^2$). The result of this transformation is presented in Fig. 6(a-c). Only a few cycles before the peak of the envelope are presented because the field needs to be strong enough to allow populations to be transferred to the second conduction band but also since there is no decoherence decay only early cycles can be studied before interference coming from previous cycles wash out the information. The nearest-neighbour recombination paths exhibit the typical recollision behaviour with a characteristic time-energy bell-curve shape that peaks around the zero of the field. Meanwhile, the on-site recombination has a flat time-energy pattern appearing at the peak of the field because recollision is forbidden by symmetry argument and most of its amplitude comes from ultrafast oscillations in the conduction band population which happens at the peak of the field.

While the difference between the nearest-neighbour and on-site recombination is obvious, the difference between the recombination from the left or the right is more subtle. The difference is maximized at the peaks of field because of the Wannier-Stark ladder. To highlight this effect, we look at the harmonics emitted at two successive peaks of the field. We label these times t_1 for the positive peak (solid line), and t_2 for the negative peak (dashed line). These line-outs are shown in Fig. 6(d), and we see that left (yellow) recombination at t_1 behaves similarly to the right (cyan) recombination at t_2 and vice-versa. That is recombining to the left is equivalent to recom-

bining to the right when you change the polarity of the field, consistent with the Wannier-Stark ladder interpretation. Moreover, the difference of the emitted energy between two successive half-cycles, for a given direction of recombination, is approximately $2F(t_1)a_0$ as shown by the solid black line and arrow, and predicted by Eq. 7c. In the first half-cycle the Wannier-Stark ladder gives a bit more energy but in the following half-cycle it removes the same amount. We expect the difference between the left and right recombination (and ionization) to be even more pronounced in non-centrosymmetric material, in these materials we get $\xi^{(\Delta l)}_{n,n'} \neq \xi^{(-\Delta l)}_{n,n'}$.

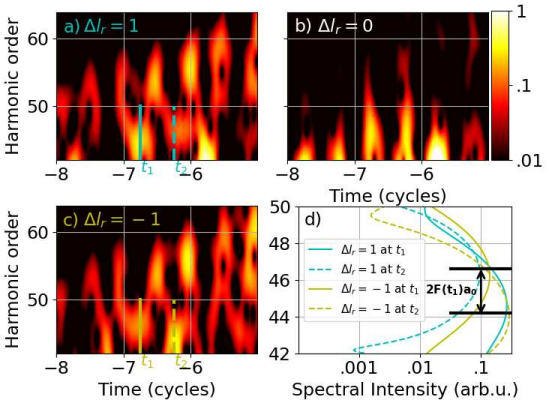

FIG. 6. Log scale color map of the Gabor transformation of the polarization with a 1/15th cycle window. Only the polarization between electron-hole pair separated by 1 (a), 0 (b) or -1 (c) is calculated. Nearest-neighbour polarizations show recollision behaviour while (b) is ionization dominated. The subtle differences between right (cyan) and left (yellow) recollisions are highlighted for positive (solid line) and negative (dashed line) peak field (d). At low energy, the Wannier-Stark ladder energy difference between two successive half-cycles can be seen.

VI. CONCLUSION

In conclusion, our real-space analysis of high-harmonic generation in solids elucidates new spatial processes, many of which do not exist in the analogous atomic case. Ionization, propagation, recombination, and emission all have a real-space character associated with transitions between lattice sites, which are frequently neglected in semi-classical model. Electron-hole correlations reveal recolliding trajectories and allowed recombination pathways. Remarkably, these correlations develop even in the absence of electron-electron interactions. Our semi-classical model also reveals the recolliding trajectories but furthermore allows us to identify the dominant pathway. Interestingly, tunnel ionization favors a lateral displacement of the generated electron-hole pair due to a reduced tunneling barrier which is a consequence of the Wannier-Stark ladder. The preferred lattice transition at ionization becomes a compromise between this reduced energy barrier and the exponentially decreasing Wannier dipole matrix element.

The Wannier semi-classical model and the electron-hole correlation in the Wannier basis provide new tools for rigorous studies of recollision in solids, which we expect to have broad implications for phenomena such as anisotropic harmonic generation [49], ellipticity-dependence of HHG[4, 15], and even suggest the possibility of tomography of electron and hole orbitals [50]. These tools should be readily applicable to strongly correlated materials [20, 51] and can be easily expanded to include Coulomb interactions between coherently created carriers. This will shed new light on problems of recent interest that inherently involve real-space processes: HHG in the presence of impurities or quantum wells, as well as nano-plasmonics where effects beyond the dipole approximation are required.

ACKNOWLEDGMENTS

G.E and M.T contributed equally to this Letter. For helpful discussions and comments, we would like to thank our colleagues A. Staudte. This research was supported by the Vanier Canada Graduate Scholarship program (G.E.), by the National Research Council's New Beginnings Fund and the United States Air Force Office of Scientific Research (award #: FA9550-16-1-0109) with contributions from the Canada Research Chairs program, Canada's Natural Sciences and Engineering Research Council and the National Research Council of Canada.

[1] M. Schultze, E. M. Bothschafter, A. Sommer, S. Holzner, W. Schweinberger, M. Fiess, M. Hofstetter, R. Kienberger, V. Apalkov, V. S. Yakovlev, M. I. Stockman, and F. Krausz, Controlling dielectrics with the electric field of light, Nature **493**, 75 (2013).

[2] A. Sommer, E. M. Bothschafter, S. A. Sato, C. Jakubeit, T. Latka, O. Razskazovskaya, H. Fattahi, M. Jobst, W. Schweinberger, V. Shirvanyan, V. S. Yakovlev, R. Kienberger, K. Yabana, M. Schultze, and F. Krausz, Attosecond real time observation of the nonlinear polarization and energy transfer in dielectrics, Nature **534**, 86 (2016).

[3] N. Dudovich, O. Smirnova, J. Levesque, Y. Mairesse, M. Y. Ivanov, D. Villeneuve, and P. B. Corkum, Measuring and controlling the birth of attosecond xuv pulses, Nature physics **2**, 781 (2006).

[4] S. Ghimire, A. D. DiChiara, E. Sistrunk, P. Agostini, L. F. DiMauro, and D. A. Reis, Observation of high-order harmonic generation in a bulk crystal, Nature Physics **7**, 138 (2011).

[5] O. Schubert, M. Hohenleutner, F. Langer, B. Urbanek, C. Lange, U. Huttner, D. Golde, T. Meier, M. Kira, S. W. Koch, and R. Huber, Sub-cycle control of terahertz high-harmonic generation by dynamical Bloch oscillations, Nature Photonics **8**, 119 (2014).

[6] T. T. Luu, M. Garg, S. Y. Kruchinin, A. Moulet, M. T. Hassan, and E. Goulielmakis, Extreme ultraviolet high-harmonic spectroscopy of solids., Nature **521**, 498 (2015).

[7] F. Langer, M. Hohenleutner, C. P. Schmid, C. Poellmann, P. Nagler, T. Korn, C. Schüller, M. S. Sherwin, U. Huttner, J. T. Steiner, S. W. Koch, M. Kira, and R. Huber, Lightwave-driven quasiparticle collisions on a subcycle timescale, Nature **533**, 225 (2016).

[8] M. Hohenleutner, F. Langer, O. Schubert, M. Knorr, U. Huttner, S. W. Koch, M. Kira, and R. Huber, Real-time observation of interfering crystal electrons in high-harmonic generation., Nature (2015).

[9] G. Vampa, T. J. Hammond, N. Thire, B. E. Schmidt, F. Legare, C. R. McDonald, T. Brabec, and P. B. Corkum, Linking high harmonics from gases and solids, Nature **522**, 462 (2015).

[10] G. Vampa, T. J. Hammond, N. Thiré, B. E. Schmidt, F. Légaré, C. R. McDonald, T. Brabec, D. D. Klug, and P. B. Corkum, All-Optical Reconstruction of Crystal Band Structure, Physical Review Letters **115**, 1 (2015).

[11] A. A. Lanin, E. A. Stepanov, A. B. Fedotov, and A. M. Zheltikov, Mapping the electron band structure by intraband high-harmonic generation in solids, Optica **4**, 516 (2017).

[12] T. T. Luu and H. J. Wörner, Measurement of the Berry curvature of solids using high-harmonic spectroscopy, Nature Communications **9**, 916 (2018).

[13] D. Bauer and K. K. Hansen, High-Harmonic Generation in Solids with and without Topological Edge States, Physical Review Letters **120**, 177401 (2018), 1711.05783.

[14] R. E. Silva, Jiménez-Galán, B. Amorim, O. Smirnova, and M. Ivanov, Topological strong-field physics on sub-laser-cycle timescale, Nature Photonics **13**, 10.1038/s41566-019-0516-1 (2019), 1806.11232.

[15] N. Tancogne-Dejean, O. D. Mücke, F. X. Kärtner, and A. Rubio, Ellipticity dependence of high-harmonic generation in solids originating from coupled intraband and interband dynamics, Nature communications **8**, 745 (2017).

[16] M. Wu, S. Ghimire, D. A. Reis, K. J. Schafer, and M. B. Gaarde, High-harmonic generation from bloch electrons in solids, Physical Review A **91**, 043839 (2015).

[17] M. Wu, D. A. Browne, K. J. Schafer, and M. B. Gaarde, Multilevel perspective on high-order harmonic generation in solids, Physical Review A **94**, 063403 (2016).

[18] S. Jiang, J. Chen, H. Wei, C. Yu, R. Lu, and C. Lin, Role of the transition dipole amplitude and phase on the generation of odd and even high-order harmonics in crystals, Physical review letters **120**, 253201 (2018).

[19] L. Li, P. Lan, X. Zhu, T. Huang, Q. Zhang, M. Lein, and P. Lu, Reciprocal-space-trajectory perspective on high-harmonic generation in solids, Physical review letters **122**, 193901 (2019).

[20] Y. Murakami, M. Eckstein, and P. Werner, High-harmonic generation in mott insulators, Physical review letters **121**, 057405 (2018).

[21] G. Vampa, B. Ghamsari, S. S. Mousavi, T. Hammond, A. Olivieri, E. Lisicka-Skrek, A. Y. Naumov, D. Villeneuve, A. Staudte, P. Berini, *et al.*, Plasmon-enhanced high-harmonic generation from silicon, Nature Physics **13**, 659 (2017).

[22] D. Golde, T. Meier, and S. W. Koch, High harmonics generated in semiconductor nanostructures by the coupled dynamics of optical inter-and intraband excitations, Physical Review B **77**, 075330 (2008).

[23] D. Golde, M. Kira, T. Meier, and S. W. Koch, Microscopic theory of the extremely nonlinear terahertz response of semiconductors, physica status solidi (b) **248**, 863 (2011).

[24] G. Vampa, C. R. McDonald, G. Orlando, P. B. Corkum, and T. Brabec, Semiclassical analysis of high harmonic generation in bulk crystals, Physical Review B **91**, 064302 (2015).

[25] J. M. Foster and S. F. Boys, Canonical Configurational Interaction Procedure, Reviews of Modern Physics **32**, 300 (1960).

[26] G. H. Wannier, The Structure of Electronic Excitation Levels in Insulating Crystals, Physical Review **52**, 191 (1937).

[27] N. Marzari, I. Souza, and D. Vanderbilt, An Introduction to Maximally-Localized Wannier Functions, Psi-k Newsletter **57** (2003).

[28] N. Marzari, A. A. Mostofi, J. R. Yates, I. Souza, and D. Vanderbilt, Maximally localized Wannier functions: Theory and applications, Reviews of Modern Physics **84**, 1419 (2012).

[29] E. N. Osika, A. Chacón, L. Ortmann, N. Suárez, J. A. Pérez-Hernández, B. Szafran, M. F. Ciappina, F. Sols, A. S. Landsman, and M. Lewenstein, Wannier-bloch approach to localization in high-harmonics generation in solids, Physical Review X **7**, 1 (2017).

[30] F. Catoire, H. Bachau, Z. Wang, C. Blaga, P. Agostini, and L. F. DiMauro, Wannier Representation of Intraband High-Order Harmonic Generation, Physical Review Letters **121**, 143902 (2018).

[31] L. Liu, J. Zhao, W. Dong, J. Liu, Y. Huang, and Z. Zhao, Spatial coherence in high-order-harmonic generation from periodic solid structures, Physical Review A **96**, 10.1103/PhysRevA.96.053403 (2017).

[32] T. Higuchi, M. I. Stockman, and P. Hommelhoff, Strong-field perspective on high-harmonic radiation from bulk solids, Physical Review Letters **113**, 213901 (2014).

[33] A. M. Parks, G. Ernotte, A. Thorpe, C. R. McDonald, P. B. Corkum, M. Taucer, and T. Brabec, Wannier quasiclassical approach to high harmonic generation in semiconductors, Optica **7**, 1764 (2020).

[34] M. Lewenstein, P. Balcou, M. Y. Ivanov, A. L'Huillier, and P. B. Corkum, Theory of high-harmonic generation by low-frequency laser fields, Physical Review A **49**, 2117 (1994), 1106.1603.

[35] L. Yue and M. B. Gaarde, Imperfect recollisions in high-harmonic generation in solids, Physical Review Letters **124**, 153204 (2020).

[36] S. Datta, *Electronic transport in mesoscopic systems* (Cambridge university press, 1997).

[37] M. J. Stevens, R. Bhat, X. Pan, H. van Driel, J. Sipe, and A. L. Smirl, Enhanced coherent control of carrier and spin density in a zinc-blende semiconductor by cascaded second-harmonic generation, Journal of applied physics **97**, 093709 (2005).

[38] R. A. Muniz and J. Sipe, Coherent control of optical injection of spin and currents in topological insulators, Physical Review B **89**, 205113 (2014).

[39] L. Yue and M. B. Gaarde, Structure gauges and laser gauges for the semiconductor bloch equations in high-order harmonic generation in solids, Physical Review A **101**, 053411 (2020).

[40] S. Jiang, H. Wei, J. Chen, C. Yu, R. Lu, and C. D. Lin, Effect of transition dipole phase on high-order-harmonic generation in solid materials, Physical Review A **96**, 1 (2017).

[41] G. Ernotte, T. J. Hammond, and M. Taucer, A Gauge Invariant Formulation of Interband and Intraband Currents in Solids, Physical Review B **98**, 235202 (2018).

[42] A. Schiffrin, T. Paasch-Colberg, N. Karpowicz, V. Apalkov, D. Gerster, S. Mühlbrandt, M. Korbman, J. Reichert, M. Schultze, S. Holzner, J. V. Barth, R. Kienberger, R. Ernstorfer, V. S. Yakovlev, M. I. Stockman, and F. Krausz, Optical-field-induced current in dielectrics., Nature **493**, 70 (2013).

[43] T. Oka, N. Konno, R. Arita, and H. Aoki, Breakdown of an electric-field driven system: A mapping to a quantum walk, Phys. Rev. Lett. **94**, 100602 (2005).

[44] I. Floss, C. Lemell, G. Wachter, V. Smejkal, S. A. Sato, X.-M. Tong, K. Yabana, and J. Burgdörfer, Ab initio multiscale simulation of high-order harmonic generation in solids, Phys. Rev. A **97**, 011401 (2018).

[45] M. Kira and S. W. Koch, *Semiconductor Quantum Optics* (Cambridge University Press, 2011).

[46] G. Ndabashimiye, S. Ghimire, M. Wu, D. A. Browne, K. J. Schafer, M. B. Gaarde, and D. A. Reis, Solid-state harmonics beyond the atomic limit, Nature **534**, 520 (2016).

[47] N. Yoshikawa, K. Nagai, K. Uchida, Y. Takaguchi, S. Sasaki, Y. Miyata, and K. Tanaka, Interband resonant high-harmonic generation by valley polarized electron–hole pairs, Nature Communications **10**, 1 (2019).

[48] A. J. Uzan, G. Orenstein, Á. Jiménez-Galán, C. McDonald, R. E. Silva, B. D. Bruner, N. D. Klimkin, V. Blanchet, T. Arusi-Parpar, M. Krüger, *et al.*, Attosecond spectral singularities in solid-state high-harmonic generation, Nature Photonics **14**, 183 (2020).

[49] Y. S. You, D. A. Reis, and S. Ghimire, Anisotropic high-harmonic generation in bulk crystals, Nature physics **13**, 345 (2017).

[50] J. Itatani, J. Levesque, D. Zeidler, H. Niikura, H. Pépin, J.-C. Kieffer, P. B. Corkum, and D. M. Villeneuve, Tomographic imaging of molecular orbitals, Nature **432**, 867 (2004).

[51] R. Silva, I. V. Blinov, A. N. Rubtsov, O. Smirnova, and M. Ivanov, High-harmonic spectroscopy of ultrafast many-body dynamics in strongly correlated systems, Nature Photonics **12**, 266 (2018).

5.4 Conclusion

The limitations of the previous Bloch model can be attributed to the assumption that the dipole varies slowly (or not at all) and can be neglected within the integral. The introduction of the Wannier approach transformed the dipole, expressing it as a Fourier series that captures its varying component within the rapidly oscillating phase of the integrand. Although this introduced more saddle points, these new points are easily interpretable as spatial displacements due to the localized nature of Wannier states. Significantly, these spatial steps play a critical role in enhancing the quantitative accuracy of the model. Furthermore, the projection of numerical simulation results onto Wannier states enabled the visualization of trajectories predicted by the Bloch model. This projection also unveiled that harmonics emitted beyond the plateau cutoff stem from recombination between different lattices. The Wannier ladder introduces additional energy quanta beyond the simple energy difference between bands.

Although this model aligns well with TDSE predictions, the next steps involve experimental confirmation. A notable prediction of the model is the significant lateral step during ionization. An interesting approach to validate this prediction could be an $\omega - 2\omega$ experiment, which uses harmonic phase to reconstruct the initial position and velocity of ionized electrons [60]. While the model accurately predicts harmonic amplitude, preliminary testing has revealed discrepancies in harmonic

phase. This outcome is not entirely unexpected, considering that the model only assumes the ionization process involves complex variables, specifically an imaginary time for tunnel ionization. A more comprehensive approach would involve treating all three saddle points as complex variables and evaluating integrals at these new values. This adjustment would allow electrons to possess a non-zero velocity at birth, potentially ionizing at points other than the Gamma point. Such an extension is crucial for predicting harmonic phase accurately and testing the model in a laboratory setting.

CHAPTER 6 Experimental Demonstration

6.1 Introduction

The subsequent articles underscore the significance of adopting a real-space perspective for a more profound comprehension of high harmonic generation (HHG) in solids. The first article presents an experiment conducted on ReS_2, a solid characterized by weak bonding between layers and atoms, as well as a band structure with closely spaced multiple bands. In this context, the utilization of Maximally Localized Wannier Functions (MLWFs) proves to be a more effective projection tool than Bloch wavefunctions. The second paper is an experimental study wherein high harmonics are generated from nanoantennas, introducing spatial variations in the electric field and necessitating a real-space interpretation.

6.2 Orbital Perspective of High Harmonic Generation in ReS_2

In this submitted paper, I did not develop the theoretical model. My contribution primarily pertained to the experimental aspect, involving the collection of harmonic spectra as a function of sample orientation. I also made a limited contribution to the manuscript writing.

In this paper, we scrutinize the harmonics produced by ReS_2, a ma-

terial characterized by low symmetry and feeble bonding between layers. In comparison to more symmetric crystals, each harmonic exhibits distinct patterns with respect to the crystal orientation, sometimes displaying elliptical polarization. Traditionally, harmonic signals polarization can be correlated with the crystal's high symmetry lines, with their polarization either aligned parallel or perpendicular. Moreover, ReS_2 manifests a strong intensity dependence, varying according to the crystal's orientation. Our theoretical model showcases a quantitative agreement with experimental observations.

Unlike the rest of this thesis, the theoretical model employs MLWFs as the Wannier states. These states, constructed from multiple bands, exhibit excellent localization on individual Re and S atoms. This characteristic facilitates the projection between different atoms and aids in identifying the most significant transition. Intriguingly, the answer to this question is highly contingent on the laser intensity.

Orbital perspective on high-harmonic generation from solids

Álvaro Jiménez-Galán[1,2], Chandler Bossaer[1], Guilmot Ernotte[1], Andrew M. Parks[3], Rui E.F. Silva[4], David M. Villeneuve[1], André Staudte[1], Thomas Brabec[3], Adina Luican-Mayer[3] and Giulio Vampa[1].

[1]*Joint Attosecond Science Laboratory, National Research Council of Canada and University of Ottawa, Ottawa, ON K1A 0R6, Canada.*

[2]*Max-Born-Institute, Max-Born Strasse 2A, D-12489, Berlin, Germany.*

[3]*Department of Physics, University of Ottawa, Ottawa, ON K1N 6N5, Canada.*

[4]*Instituto de Ciencia de Materiales de Madrid (ICMM), Consejo Superior de Investigaciones Científicas (CSIC), Sor Juana Inés de la Cruz 3, 28049 Madrid, Spain.*

High-harmonic generation in solids allows probing and controlling electron dynamics in crystals on few femtosecond timescales, paving the way to lightwave electronics. In the spatial domain, recent advances in the real-space interpretation of high-harmonic emission in solids allows imaging the field-free, static, potential of the valence electrons with picometer resolution. The combination of such extreme spatial and temporal resolutions to measure and control strong-field dynamics in solids at the atomic scale is poised to unlock a new frontier of lightwave electronics. Here, we report a strong intensity-dependent anisotropy in the high-harmonic generation from ReS_2 that we attribute to angle-dependent interference of currents from the different atoms in the unit cell. Furthermore, we demonstrate how the

laser parameters control the relative contribution of these atoms to the high-harmonic emission. Our findings provide an unprecedented atomic perspective on strong-field dynamics in crystals and suggest that crystals with a large number of atoms in the unit cell are not necessarily more efficient harmonic emitters than those with fewer atoms.

The foundational concept underpinning attosecond physics, and high-harmonic generation in gas-phase atoms and molecules in particular, is the energetic recollision of an electron ionized and accelerated by a strong laser field with the parent ion [1–4]. This dynamic real-space framework is instrumental to link the characteristics of the emitted harmonic radiation (amplitudes, phases and polarization) to sub-laser-cycle dynamics of atomic and molecular orbitals [5–9]. In solids, high-harmonic generation (HHG) is understood using a similar framework, albeit exchanging the real-space perspective for one in reciprocal space, where electron-hole pairs accelerate and recombine across energy bands in the Brillouin zone of the crystal [10–13]. This reciprocal-space approach has been paramount in virtually all investigations of solid-state high-harmonics: from revealing the role of electron-hole recollisions in the emission process [14], to reconstructing the band structure of a ZnO crystal [15], to explaining the multiple plateaus observed in the HHG spectrum [16] and to map regions of crystal momenta where the electron-hole velocity vanishes [17], among others [18–24].

Despite the success of the reciprocal-space picture, a real-space approach offers a more intuitive framework, in particular in complex materials with many narrowly spaced and overlapping bands. The advantages of using a real-space perspective to understand HHG from solids are quickly starting to become apparent [25–27], for example, in interpreting spatially-displaced electron-

hole recollision processes [27,28] or as means to directly reconstruct the field-free (static) valence electron potential at the picometer scale [29]. The possibility to link features of the high-harmonic spectrum to *dynamics* occurring at specific orbitals in the lattice remains, however, largely unexplored. Here, we demonstrate this possibility through angle-resolved measurements of HHG in ReS_2. We measure a strong, intensity-dependent anisotropy of the HHG emission and trace it back to the interplay between the currents generated by each individual atom in the unit cell. Simulating the laser-matter interaction using a basis constructed from maximally-localized Wannier orbitals, we show that by changing the laser parameters (intensity and polarization), one can activate or suppress the contribution of specific atoms to the HHG emission and interfere the atomic currents differently, increasing or decreasing the high-harmonic emission efficiency.

ReS_2 is a layered semiconductor that crystallizes in a distorted octahedral (T) phase [30,32–34]. Figure **1a** illustrates the unit cell of the monolayer, formed by 4 rhenium atoms and 8 sulfur atoms. The 4 Re clusters are linked in a chain oriented along $\theta = 120^\circ$ (see panel a). While the anisotropy of the crystal structure is clear (the crystal symmetry group is *P-1*), the band structure is similar along different angles and is very dense (see Figure **1b** and Supplementary Note 1), and with a density of states near the Fermi energy significantly higher than other prototypical materials used in HHG spectroscopy, such as MgO or ZnO [35]. Going from the monolayer limit to bulk, these features remain, and the band structure changes only slightly [30,31]. In such dense band diagram, associating an individual harmonic with reciprocal space trajectories of charge carriers in a particular set of bands, according to the reciprocal-space method, is hardly straightforward (see circular markers in Fig. **1b-d**), and is unlikely to provide much insight into the carrier dynamics. On the other hand,

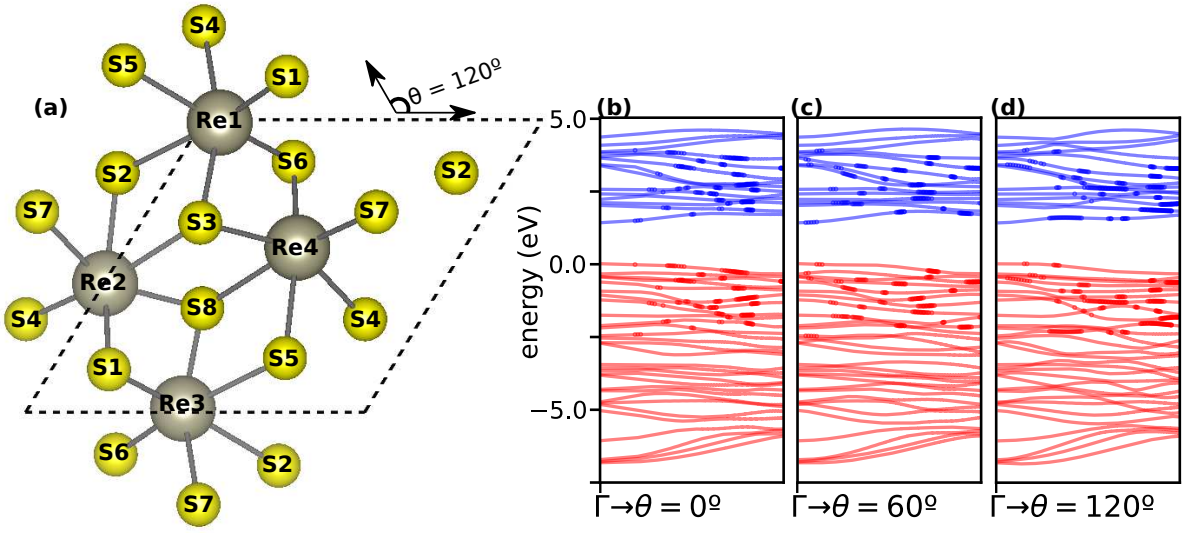

Figure 1: **Monolayer ReS_2.** (a) Crystal structure, composed of 4 rhenium atoms and 8 sulfur atoms in a distorted octohedral structure. The unit cell is delimited by the parallelogram. (b-d) Band structure of the monolayer along (a) $\theta = 0°$, (b) $\theta = 60°$ and (c) $\theta = 120°$ (see panel a for definition of θ). Circular markers across the bands in panels (b-d) highlight vertical transitions resonant with the 11th harmonic (H11). Monolayer and bulk (not shown) forms of ReS_2 are both inversion symmetric and display a very similar electronic band structure, with a nearly identical direct band gap of 1.4eV at the Γ point [30,31].

the small bandwidth indicates that the electrons are very localized in the individual atoms of the lattice, making it ideally suited for a real-space or orbital-based framework.

The first question we want to address is if high harmonics generated from ReS_2 reflect the strong anisotropy apparent in real space or rather the weak angular dependence of its band structure. We generate high harmonics from bulk ReS_2 with a linearly-polarized mid-infrared pulse with a duration of 80 fs and a center wavelength of 3.5 μm (see Methods). Figure **2a** shows the high-harmonic spectrum measured for a laser intensity of 0.64 TW/cm^2 and polarization along θ = 120° (see inset). We observe odd harmonics extending up to the 13$^{\text{th}}$ order, while even harmonics are absent as expected from the inversion symmetry of ReS_2. We measure the orientation dependence of the harmonics by rotating the polarization of the linear pulse with respect to the crystal. The results, shown in Figure **2b-d**, display a clear anisotropy for all harmonic orders. Furthermore, the anisotropy depends strongly on the laser intensity.

In order to understand the origin of this anisotropy, we perform time-dependent simulations in a basis constructed from 44 maximally-localized Wannier orbitals (see Methods for details) [36]. The similarity between the monolayer and bulk forms in the case of ReS_2 [30,31], allows us to reduce the computational complexity and simulate the monolayer system. The orientation dependence of H9 and H11 obtained from the numerical simulations is shown in Figure **3a,b**. While the uncertainty of the experimental intensities and the differences between the monolayer and bulk forms do not allow for a quantitative experiment-theory comparison (e.g., of the exact position of the harmonic maxima), our simulations clearly display the strong intensity-dependent anisotropy

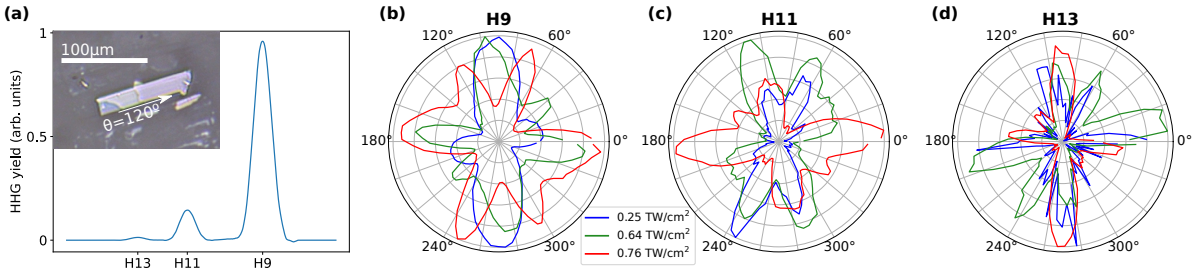

Figure 2: **Measured orientation-dependent HHG from ReS_2.** (a) High-harmonic spectrum for a laser intensity of 0.64 TW/cm^2 and polarization along $\theta = 120°$ (parallel to the rhenium chains). The inset shows an optical micrograph of the bulk ReS_2 flake using a CMOS camera and white-light illumination, with the longest edge corresponding to the rhenium chains. (b-d) Orientation dependence of (b) H9, (c) H11 and (d) H13 for three different intensities: 0.25 TW/cm^2 (blue), 0.64 TW/cm^2 (green) and 0.76 TW/cm^2 (red).

observed in the experiment. As a result, the simulations in monolayer ReS_2 can provide valuable insight for the origin of this effect.

The high-harmonic spectrum is given by the Fourier components of the time-dependent current that is generated by the laser-induced oscillating dipole of the medium (see Methods),

$$I(\omega) = \sum_{\alpha} \left| \mathcal{F}[J_\alpha(t)](\omega) \right|^2 , \tag{1}$$

where $J_\alpha(t)$ is the total current along direction $\alpha = (\parallel, \perp)$, corresponding to the components parallel and perpendicular to the electric field, respectively. The total current can be expressed as a sum of currents from all the orbitals in the lattice, $J_\alpha(t) = \sum_n^{N_{\text{orb}}} J_{n,\alpha}^{(\text{W})}(t)$, where $J_{n,\alpha}^{(\text{W})}(t)$ represents the contribution to the total current of the changing population of orbital n and its coherence with all other orbitals (see Methods). The subscript (W) indicates that such orbital currents are defined

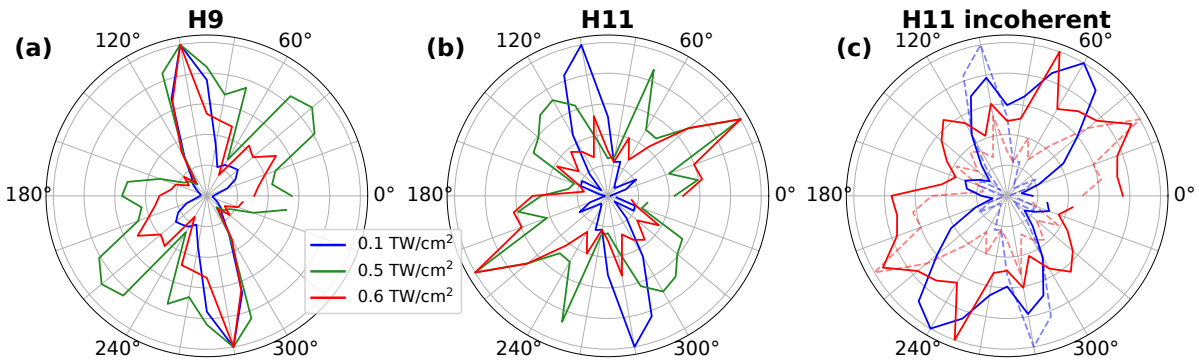

Figure 3: **Calculated orientation-dependent HHG from ReS_2.** (a,b) Full calculation of harmonics (a) H9 and (b) H11 for different intensities: 0.1 TW/cm^2 (blue), 0.5 TW/cm^2 (green) and 0.6 TW/cm^2 (red). (c) Calculation neglecting the Fourier phase (solid lines) φ_n of the orbital current for H11 for 0.1 TW/cm^2 (blue) and 0.6 TW/cm^2 (red). For comparison, the full calculation curves of panel (b) are shown in (c) with dashed, faint lines.

in the Wannier gauge and, even if they are not observable, provide a unique real-space perspective into the HHG process. Expressed in terms of the individual orbital currents, the high-harmonic spectrum is

$$I_\alpha(\omega) = \left| \sum_n^{N_{\text{orb}}} \mathcal{F}[J_{n,\alpha}^{(W)}(t)](\omega) \right|^2 = \sum_n^{N_{\text{orb}}} \left[|A_{n,\alpha}(\omega)|^2 + |A_{n,\alpha}(\omega)| \sum_{m \neq n} |A_{m,\alpha}(\omega)| \cos(\varphi_{m,\alpha}(\omega) - \varphi_{n,\alpha}(\omega)) \right], \tag{2}$$

where $A_{n,\alpha}$ and $\varphi_{n,\alpha}$ are, respectively, the spectral amplitude and phase of the current of orbital n along direction α.

Equation 2 allows us to distinguish features that arise from the interference of different orbital currents. The incoherent sum of the individual currents, $I_\alpha^{\text{incoh}}(\omega) = \sum_n^{N_{\text{orb}}} \left| \mathcal{F}[J_{n,\alpha}^{(W)}(t)](\omega) \right|^2$, will be absent of such interference. In Figure **3c** we compare the angle-dependent harmonic yield of

H11 for I_α^{incoh} (solid lines) and the observable signal I_α (faint dashed lines). A similar analysis for H9 is made in Supplementary Note 2. The angular variation is stronger for I_α, with near-complete suppression of various secondary maxima that are present in I_α^{incoh} (most notably near 60°), strongly modifying the orientation dependence. Thus, orbital phase interference is an important factor determining the orientation dependence.

Since the electrons are well localized on each atomic site (see Extended Data), we can group together the currents of the m orbitals belonging to the same atom A into an atomic current, $J^{(\text{W})}_{A,\alpha}(t) = \sum_m J^{(\text{W})}_{m,\alpha}(t)$. Furthermore, due to the inversion symmetry of ReS_2, each atom is related to one other by an inversion operation, for example, Re_1 and Re_3 or S_1 and S_6 (see Fig. **1a**). Both of the atoms in the pair give rise to the same Fourier amplitudes and phases, so that the total harmonic spectrum in Eq. 2 reduces to the sum of the Fourier amplitudes and phases of six atomic (inversion-related) pairs.

Figures **4a,b** show the Fourier amplitudes and phases of the six atomic pairs, indicated with different colors, for H11 along $\alpha = \parallel$ and for two intensities: 0.1 TW/cm^2 and 0.6 TW/cm^2. At both low and high intensities (Figure **4a-b** respectively) emission is spread over a wide range of phases at any given angle. For the lowest intensity (Figure **4a**), every atomic pair contributes a similar amplitude to the emission near $\theta = 40 - 60°$, but their phases are spread equally over π rad, thus leading to the near-perfect destructive interference seen in Fig. **3b** (blue curve) at these angles. On the other hand, for angles close to $\theta = 100°$, the Fourier phases from the different atomic sites are similar, leading to constructive interference in Eq. 2 and therefore to the peak observed in

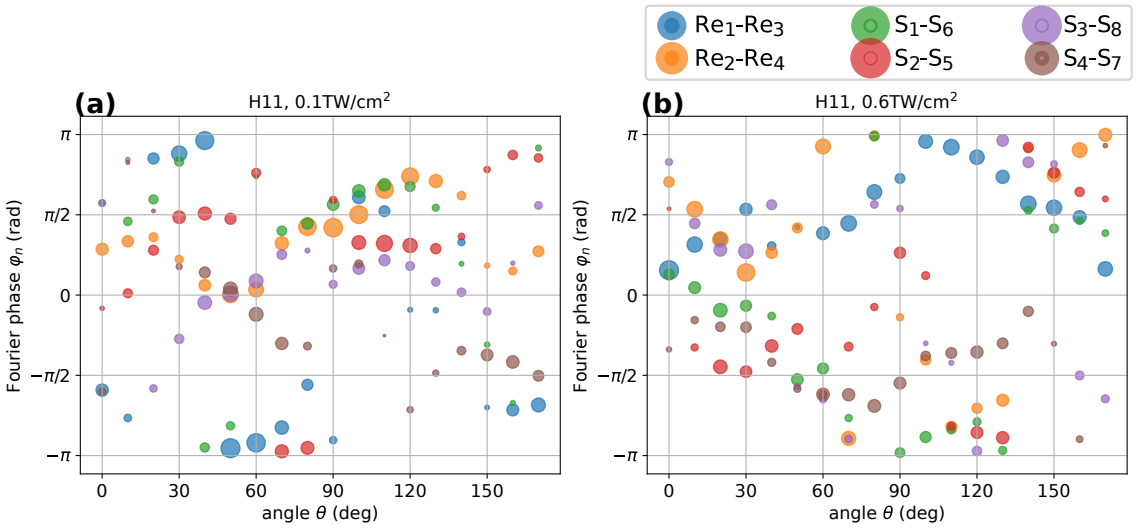

Figure 4: **Atomic contributions to harmonic emission in ReS_2.** The circle colors represent the six different atomic pairs, the size of the circle is proportional to the Fourier amplitude $|A_n|$ and the Fourier phase φ_n is given in the vertical axis. The panels display the Fourier amplitudes $|A_n|$ and phases φ_n of the six atomic pairs (inversion-symmetric partners) as a function of the laser polarization angle for H11. Two driver intensities are shown: (a) 0.1TW/cm^2 and (b) 0.6 TW/cm^2. The results shown are for the harmonic polarization α that is parallel to the electric field.

Figure **3b** (blue curve). At θ = 100°, the atomic pair Re_2-Re_4, which contributes the most to H11 at low intensity, is largely suppressed at large intensity (compare size of orange circle in Figure **4a,b**). This analysis shows that atoms that do not contribute to the generation of a particular harmonic order for one driver intensity, can be activated for other intensities, and vice versa, suggesting that laser intensity could be used as a mechanism to control the relative weight of atomic orbitals in HHG. An analogous analysis can be made for the rest of harmonic orders, along both $\alpha = \parallel, \perp$ directions, and is left for Supplementary Note 2.

In conclusion, we identify how the nonlinear currents residing on each of the twelve atoms in the unit cell of a ReS_2 crystal are responsible for the strongly anisotropic and intensity-dependent emission of high-order harmonics. Our orbital analysis based on maximally localized Wannier functions reveals that each atomic contribution depends strongly on the polarization angle and intensity of the driving field, paving the way to characterizing and controlling electron dynamics at the picometer-scale in solids on sub-laser-cycle timescales. Moreover, we show that interference between atoms in the unit cell of a crystal is key to determine the macroscopic high-harmonic emission, a critical factor to consider in the route towards developing efficient harmonic emitters.

Methods

Experimental methods ReS_2 flakes were mechanically exfoliated from an extracted section of a bulk sample using tape, then dispersed across the tape by folding over itself to reduce thickness and produce generally flat flakes. The ReS_2 crystal was transferred from the tape to a PDMS stamp,

then transferred from the stamp to the substrate at 80°. The substrate consists of a two-side polished, 10x10x0.5mm, (100)-cut MgO single crystal that is cleaned with acetone and isopropanol. The PDMS stamp was peeled off to leave the bulk ReS_2 flakes on the MgO substrate.

The sample is imaged in-situ with a white-light source as well as the laser source, allowing sample areas of interest to be located and crystallographic orientation to be measured.

The laser source consists of a YB:KGW laser (LightConversion Carbide CB3) delivering 200fs pulses at a center wavelength of 1030nm with a repetition rate of 100kHz and average power of 80W. A portion of this power (60W) pumps a commercial optical parametric amplifier (LightConversion Orpheus-MIR), generating 60fs mid-infrared pulses at a wavelength of 3.5μm. An Ag off-axis parabolic mirror focuses the mid-infrared beam onto the sample, producing high harmonics. The generated high harmonics are collected in transmission geometry and focused on the input slit of a Princeton Instruments IsoPlane spectrometer with an Al spherical mirror of 15cm focal length. A half-wave plate is positioned between the parabolic mirror and the sample to rotate the linear laser polarization with respect to the crystal axis.

Numerical methods The field-free Hamiltonian and dipole couplings of monolayer ReS_2 were calculated with the electronic structure code Quantum Espresso [37] on a Monkhorst-Pack (MP) grid of 12x12x1 points using a norm-conserving Perdew-Burke-Ernzerhof (PBE) exchange correlation functional. The field-free Hamiltonian used in the time-dependent propagation was constructed by projecting the Bloch states onto a set of maximally-localized Wannier functions using the Wannier90 code [36]. In particular, we projected onto the d orbitals of the four rhenium atoms and the

158 p orbitals of the six sulfur atoms, totalling 44 bands. The Hamiltonian in the basis constructed
159 from Wannier functions was then propagated in the presence of the electric field using the density
160 matrix formalism with the code described in Ref. [26]. The large size of the unit cell allowed us to
161 obtain convergence with a modest MP grid of 50x50 k-points along the b_1 and b_2 reciprocal lattice
162 vectors. The time step was set to 0.2 a.u. and the dephasing time was chosen to be T_2 = 10 fs.

163 The time-dependent current along direction α, used to extract the high harmonic spectrum,
164 is defined as

$$J_\alpha(t) = -\frac{|e|}{N_k} \sum_{\mathbf{k}} \mathrm{Tr}\left[\hat{\mathbf{v}}_\alpha(\mathbf{k}) \cdot \rho(\mathbf{k}, t)\right]. \tag{3}$$

165 Above, e is the electron charge, N_k is the number of crystal momenta included in the calculation, $\hat{\mathbf{v}}$
166 is the velocity operator, and ρ is the density matrix. In the Wannier gauge, the density matrix $\rho^{(\mathrm{W})}$
167 contains the orbital populations and coherences in its diagonal and off-diagonal terms, respectively.
168 In the Wannier gauge, we may define a (real) current from an individual orbital n along direction
169 α as

$$J^{(\mathrm{W})}_{n,\alpha}(t) = -\frac{|e|}{N_k} \mathrm{Re}\{\sum_{\mathbf{k}} \sum_{m}^{N_{\mathrm{orb}}} \left[\hat{v}^{(\mathrm{W})}_{nm,\alpha} \cdot \rho^{(\mathrm{W})}_{mn}\right]\}, \tag{4}$$

170 such that the sum of the currents from all orbitals equals the total current,

$$J_\alpha(t) = \sum_{n}^{N_{\mathrm{orb}}} J^{(\mathrm{W})}_{n,\alpha}(t). \tag{5}$$

171 For clarity, we give an example for a two-orbital model, although we point out that our
172 analysis is only relevant for multi-orbital crystals as the one presented in this work. In the two-

orbital case,

$$J_{1,\alpha}(t) = \mathrm{Re}(\{v_{11,\alpha}\rho_{11} + v_{12,\alpha}\rho_{21}\}$$
$$J_{2,\alpha}(t) = \mathrm{Re}\{v_{22,\alpha}\rho_{22} + v_{21,\alpha}\rho_{12}\}, \tag{6}$$

where the subscripts 1 and 2 identify the orbital and $\alpha = \parallel, \perp$ the direction of current emission. Since both the velocity and density matrices are hermitian, the current of an individual orbital is composed of a term associated to the population change of that orbital, plus exactly half of the contribution of the coherence between that orbital and the rest. Thus, this approach offers a way of quantifying the contribution of individual orbitals, and their interference, to the high-harmonic generation.

Data availability The data that support the plots within this paper and other findings of this study are available from the corresponding author upon reasonable request.

References

1. Corkum, P. B. Plasma Perspective on Strong-Field Multiphoton Ionization. *Phys. Rev. Lett.* **71**, 1994–1997 (1993).

2. Krause, J. L., Schafer, K. J. & Kulander, K. C. High-order harmonic generation from atoms and ions in the high intensity regime. *Phys. Rev. Lett.* **68**, 3535–3538 (1992). URL https://link.aps.org/doi/10.1103/PhysRevLett.68.3535.

3. Lewenstein, M., Balcou, P., Ivanov, M. Y., L'Huillier, A. & Corkum, P. B. Theory of high-harmonic generation by low-frequency laser fields. *Physical Review A* **49** (1994). URL

https://link.aps.org/doi/10.1103/PhysRevA.49.2117.

4. Krausz, F. & Ivanov, M. Attosecond physics. *Rev. Mod. Phys.* **81**, 163–234 (2009). URL http://link.aps.org/doi/10.1103/RevModPhys.81.163.

5. Levesque, J., Zeidler, D., Marangos, J. P., Corkum, P. B. & Villeneuve, D. M. High Harmonic Generation and the Role of Atomic Orbital Wave Functions. *Phys. Rev. Lett.* **98**, 183903 (2007). URL https://link.aps.org/doi/10.1103/PhysRevLett.98.183903.

6. Smirnova, O. *et al.* High harmonic interferometry of multi-electron dynamics in molecules. *Nature* **460**, 972–977 (2009). URL http://dx.doi.org/10.1038/nature08253. arXiv:1304.2413v1.

7. Wörner, H. J., Bertrand, J. B., Kartashov, D. V., Corkum, P. B. & Villeneuve, D. M. Following a chemical reaction using high-harmonic interferometry. *Nature* **466**, 604–607 (2010). URL http://www.nature.com/doifinder/10.1038/nature09185.

8. Cireasa, R. *et al.* Probing molecular chirality on a sub-femtosecond timescale. *Nat. Phys.* **11** (2015). URL http://dx.doi.org/10.1038/nphys3369.

9. Kraus, P. M., Zürch, M., Cushing, S. K., Neumark, D. M. & Leone, S. R. The ultrafast X-ray spectroscopic revolution in chemical dynamics. *Nature Reviews Chemistry* **2**, 82–94 (2018). URL https://doi.org/10.1038/s41570-018-0008-8.

10. Vampa, G. *et al.* Linking high harmonics from gases and solids. *Nature* **522** (2015). URL http://dx.doi.org/10.1038/nature14517.

211 11. Kruchinin, S. Y., Krausz, F. & Yakovlev, V. S. Colloquium: Strong-field
212 phenomena in periodic systems. *Rev. Mod. Phys.* **90**, 21002 (2018). URL
213 https://link.aps.org/doi/10.1103/RevModPhys.90.021002.

214 12. Yue, L. & Gaarde, M. B. Introduction to theory of high-harmonic genera-
215 tion in solids: tutorial. *J. Opt. Soc. Am. B* **39**, 535–555 (2022). URL
216 https://opg.optica.org/josab/abstract.cfm?URI=josab-39-2-535.

217 13. Goulielmakis, E. & Brabec, T. High harmonic generation in condensed matter. *Nature Photon-*
218 *ics* **16**, 411–421 (2022). URL https://doi.org/10.1038/s41566-022-00988-y.

219 14. Vampa, G. *et al.* Theoretical Analysis of High-Harmonic Genera-
220 tion in Solids. *Physical Review Letters* **113**, 73901 (2014). URL
221 https://link.aps.org/doi/10.1103/PhysRevLett.113.073901.

222 15. Vampa, G. *et al.* All-Optical Reconstruction of Crystal Band
223 Structure. *Phys. Rev. Lett.* **115**, 193603 (2015). URL
224 https://link.aps.org/doi/10.1103/PhysRevLett.115.193603.

225 16. Ndabashimiye, G. *et al.* Solid-state harmonics beyond the atomic limit. *Nature* **534**, 520–523
226 (2016). URL http://dx.doi.org/10.1038/nature17660.

227 17. Uzan, A. J. *et al.* Attosecond spectral singularities in solid-state high-
228 harmonic generation. *Nature Photonics* **14**, 183–187 (2020). URL
229 https://doi.org/10.1038/s41566-019-0574-4.

230 18. Liu, H. *et al.* High-harmonic generation from an atomically thin semiconductor. *Nature*
231 *Physics* **13**, 262–265 (2017). URL https://doi.org/10.1038/nphys3946.

232 19. Bauer, D. & Hansen, K. K. High-harmonic generation in solids with and with-
233 out topological edge states. *Phys. Rev. Lett.* **120**, 177401 (2018). URL
234 https://link.aps.org/doi/10.1103/PhysRevLett.120.177401.

235 20. Luu, T. T. *et al.* Extreme ultraviolet high-harmonic spectroscopy of solids. *Nature* **521**, 498–
236 502 (2015).

237 21. Langer, F. *et al.* Lightwave-driven quasiparticle collisions on a subcycle timescale.
238 *Nature* **533**, 225 (2016). URL https://doi.org/10.1038/nature17958
239 http://10.0.4.14/nature17958.

240 22. Jiménez-Galán, Á., Silva, R. E. F., Smirnova, O. & Ivanov, M.
241 Sub-cycle valleytronics: control of valley polarization using few-
242 cycle linearly polarized pulses. *Optica* **8**, 277–280 (2021). URL
243 http://www.osapublishing.org/optica/abstract.cfm?URI=optica-8-3-277.

244 23. Amini, K. *et al.* Symphony on strong field approximation. *Reports on Progress in Physics* **82**,
245 116001 (2019). URL https://dx.doi.org/10.1088/1361-6633/ab2bb1.

246 24. Franz, D. *et al.* All semiconductor enhanced high-harmonic generation from
247 a single nanostructured cone. *Scientific Reports* **9**, 5663 (2019). URL
248 https://doi.org/10.1038/s41598-019-41642-y.

249 25. Osika, E. N. *et al.* Wannier-bloch approach to localization in high-
250 harmonics generation in solids. *Phys. Rev. X* **7**, 021017 (2017). URL
251 https://link.aps.org/doi/10.1103/PhysRevX.7.021017.

252 26. Silva, R. E. F., Martín, F. & Ivanov, M. High harmonic generation in crystals us-
253 ing maximally localized Wannier functions. *Phys. Rev. B* **100**, 195201 (2019). URL
254 https://link.aps.org/doi/10.1103/PhysRevB.100.195201.

255 27. Parks, A. M. *et al.* Wannier quasi-classical approach to high har-
256 monic generation in semiconductors. *Optica* **7**, 1764–1772 (2020). URL
257 http://www.osapublishing.org/optica/abstract.cfm?URI=optica-7-12-1764.

258 28. Yue, L. & Gaarde, M. B. Imperfect recollisions in high-harmonic
259 generation in solids. *Phys. Rev. Lett.* **124**, 153204 (2020). URL
260 https://link.aps.org/doi/10.1103/PhysRevLett.124.153204.

261 29. Lakhotia, H. *et al.* Laser picoscopy of valence electrons in solids. *Nature* **583**, 55–59 (2020).
262 URL https://doi.org/10.1038/s41586-020-2429-z.

263 30. Tongay, S. *et al.* Monolayer behaviour in bulk ReS2 due to electronic
264 and vibrational decoupling. *Nature Communications* **5**, 3252 (2014). URL
265 https://doi.org/10.1038/ncomms4252.

266 31. Gehlmann, M. *et al.* Direct Observation of the Band Gap Transition
267 in Atomically Thin ReS2. *Nano Letters* **17**, 5187–5192 (2017). URL
268 https://doi.org/10.1021/acs.nanolett.7b00627.

269 32. Wolverson, D., Crampin, S., Kazemi, A. S., Ilie, A. & Bending, S. J. Raman Spectra of
270 Monolayer, Few-Layer, and Bulk ReSe2: An Anisotropic Layered Semiconductor. *ACS Nano*
271 **8**, 11154–11164 (2014). URL https://doi.org/10.1021/nn5053926.

272 33. Lin, Y.-C. *et al.* Single-Layer ReS2: Two-Dimensional Semiconductor with
273 Tunable In-Plane Anisotropy. *ACS Nano* **9**, 11249–11257 (2015). URL
274 https://doi.org/10.1021/acsnano.5b04851.

275 34. Plumadore, R. *et al.* Prevalence of oxygen defects in an in-plane anisotropic
276 transition metal dichalcogenide. *Phys. Rev. B* **102**, 205408 (2020). URL
277 https://link.aps.org/doi/10.1103/PhysRevB.102.205408.

278 35. For a comparison of the density of states near the Fermi energy of ReS_2, MgO
279 and ZnO, see https://materialsproject.org/materials/mp-572758,
280 https://materialsproject.org/materials/mp-1265 and
281 https://materialsproject.org/materials/mp-2133.

282 36. Marzari, N., Mostofi, A. A., Yates, J. R., Souza, I. & Vanderbilt, D. Maximally localized
283 Wannier functions: Theory and applications. *Rev. Mod. Phys.* **84**, 1419–1475 (2012). URL
284 https://link.aps.org/doi/10.1103/RevModPhys.84.1419.

285 37. Giannozzi, P. *et al.* QUANTUM ESPRESSO: a modular and open-source software project for
286 quantum simulations of materials. *Journal of Physics: Condensed Matter* **21**, 395502 (2009).
287 URL http://stacks.iop.org/0953-8984/21/i=39/a=395502.

288 **Acknowledgements** We thank David Crane, Ryan Kroeker and Andrei Naumov for continued
289 technical support. A. J. G. acknowledges support from the European Union's Horizon 2020 re-
290 search and innovation program under the Marie Skłodowska-Curie Grant Agreement No. 101028938
291 and the Joint Center for Extreme Photonics. G. V. acknowledges support from the Joint Center for
292 Extreme Photonics and the National Research Council's Quantum Sensing program. D.V. ac-
293 knowledges support from the Joint Center for Extreme Photonics. R.E.F.S. acknowledges support
294 from the fellowship LCF/BQ/PR21/11840008 from "La Caixa" Foundation (ID 100010434).

295 **Authors contribution** C. B. and G. E. performed the experiments; A. J. G. performed the nu-
296 merical analysis and calculations; A. P. and R.E.F.S. performed ancillary calculations; R.E.F.S.
297 developed the numerical code; D. M. V., A. S., T. B., A. L. M. and G. V. supervised the work. A.
298 J. G. and G. V. wrote the manuscript with contributions from all co-authors.

299 **Corresponding authors** please address all correspondence to G. V. (gvampa@uottawa.ca).

300 **Competing interests** The authors declare no competing interests.

6.3 Controlling the Polarization and Phase of High-Order Harmonics with a Plasmonic Metasurface

In this paper, my involvement was primarily in the experimental aspect. I developped a new laser line for HHG in solids. While I did not contribute to the sample preparation or the collection of the final harmonic spectra, I played a significant role in upstream experiments and in the composing the manuscript.

Although this article does not delve into Wannier states, it presents an HHG experiment in solids involving nanoantennas. The objective of the experiment was to generate circularly polarized light. The nanoantennas were strategically designed to resonate with the driving laser, thereby amplifying the electric field in the silicon substrate. The experiment entailed the creation of a pair of nanoantennas oriented perpendicularly to each other, with the driving laser being circularly polarized. Alternatively, the circularly polarized laser can be conceptualized as two linearly polarized driving laser fields, each having perpendicular polarization and a quarter-cycle delay. The phase of the emitted harmonics is linearly related to the phase of the driving field ($\phi_n = n\phi_1$). Within the context of these nanoantennas, this implies that odd harmonics will be emitted with $\pm$ quarter-cycle phase differences between the two pairs of nanoantennas. Consequently, the emitted harmonics will exhibit circular polarization. Generating circularly polarized harmonics is crucial for probing ultrafast magnetic processes, a challenge that has historically

been daunting due to the requirement of electron-hole recollision. However, the unique degrees of freedom offered by solid targets, as opposed to conventional gas targets, have now made this possible.

Research Article Vol. 9, No. 9 / September 2022 / Optica 987

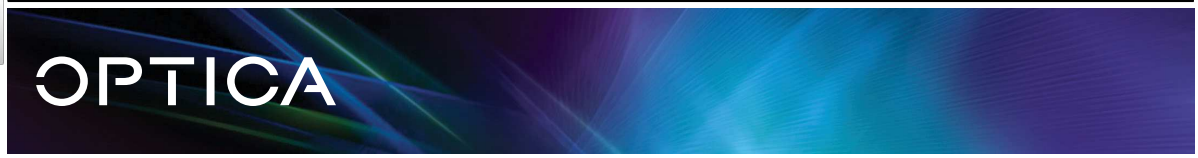

Controlling the polarization and phase of high-order harmonics with a plasmonic metasurface

Sohail A. Jalil,[1] Kashif M. Awan,[2] Idriss A. Ali,[1] Sabaa Rashid,[3] Joshua Baxter,[3,4] Aleksey Korobenko,[1] Guilmot Ernotte,[1] Andrei Naumov,[1] David M. Villeneuve,[1] André Staudte,[1] Pierre Berini,[3,4,5] Lora Ramunno,[3,4] and Giulio Vampa[1,*]

[1]Joint Attosecond Science Laboratory, National Research Council of Canada and University of Ottawa, Ottawa, Ontario K1N 0R6, Canada
[2]Stewart Blusson Quantum Matter Institute, University of British Columbia, Vancouver, British Columbia V6T 1Z4, Canada
[3]Centre for Research in Photonics, University of Ottawa, 25 Templeton Street, Ottawa, Ontario K1N 6N5, Canada
[4]Department of Physics, University of Ottawa, 150 Louis Pasteur, Ottawa, Ontario K1N 6N5, Canada
[5]School of Electrical Engineering and Computer Science, University of Ottawa, 800 King Edward Avenue, Ottawa, Ontario K1N 6N5, Canada
*Corresponding author: gvampa@uottawa.ca

Received 18 May 2022; revised 5 August 2022; accepted 6 August 2022; published 24 August 2022

Nanostructured surfaces, or metasurfaces, allow exquisite control of linear and nonlinear optical processes by reshaping the amplitude, phase, and polarization of electric and magnetic fields near wavelength-scale heterogeneities. Recently, metasurfaces have broken new ground in high-field attosecond science where they have been utilized to amplify the emission of high-order harmonics of femtosecond infrared laser pulses, a notoriously inefficient process, by enhancing the incident field, and to shape the emitted high harmonics in space. Here we show control of the polarization and phase of high harmonics with a plasmonic metasurface. We design and fabricate perpendicularly aligned rectangular gold antennas on a silicon crystal that generate circularly polarized deep-ultraviolet high harmonics, from a circularly polarized infrared driver, providing a simple path for achieving circular emission from patterned crystals. Our metasurface enhances the circularly polarized harmonics up to ∼43 times when compared to the unpatterned surface, where harmonics are quenched. Looking forward, circularly polarized high harmonics will be useful tools for sensing chiral laser–matter interactions and magnetic materials. Our approach paves the way for polarization control at even shorter, extreme ultraviolet, wavelengths.

https://doi.org/10.1364/OPTICA.464445

1. INTRODUCTION

High-harmonic generation (HHG) is an extremely nonlinear optical process that converts low-energy photons into high-energy ones during interaction with gases [1], liquids [2], and solids [3]. Solid-state HHG has been reported from high-density bulk dielectrics [4,5], semiconductors [3,6], single crystal metals [7], and 2D materials [8], as well as from nanostructured surfaces [9–18]. The latter showcases the flexibility of tailoring the nonlinear optical properties with nano-structuring, opening new research opportunities at the confluence of attosecond science and nanophotonics [19–21].

The effect of nanostructures on solid-state HHG is twofold. First, each individual nanoscale feature enhances the laser electric field and thereby the local HHG efficiency. Such nanostructures have been shown to enhance HHG from sapphire–metal nanocones [9], ZnO cones and ridges [10], plasmonic Au antennas on Si [11], GaP antennas [15], Fano-resonance structures [12], metasurfaces supporting optical bound states in the continuum [16], and epsilon near zero material [13]. Second, far-field emission profiles of the high harmonics can be controlled by arranging the location of individual nanostructures [10]. For instance, focusing harmonics to the diffraction limit has been achieved with Fresnel zone plates [10,17]. More recently, controlled diffraction of extreme ultraviolet (XUV) high harmonics at a photon energy of 11 eV has been achieved with a nanostructured MgO surface [18]. We note that the aforementioned experiments generated linearly polarized harmonics in the UV or XUV regime.

On the other hand, circularly polarized high harmonics are a promising tool for probing magnetic properties of solids [22,23] and chirality-sensitive laser–matter interaction [24,25]. However, a circularly polarized driver cannot produce circularly polarized high harmonics from a gas target because the electrons cannot recollide with the parent ion [26]. More sophisticated engineered optical fields can avoid this problem [27–30]. Some crystals can also produce circularly polarized high harmonics [5,31]. An alternative approach to control polarization of emitted harmonics is using nanostructured metasurfaces. Metasurfaces have been utilized to shape the polarization of low-order perturbative harmonics in the visible and infrared spectral regions [32–35]. In this context, the Pancharatnam–Berry phase, or *geometric* phase, method allows a continuous variation of the nonlinear phase, and thus of

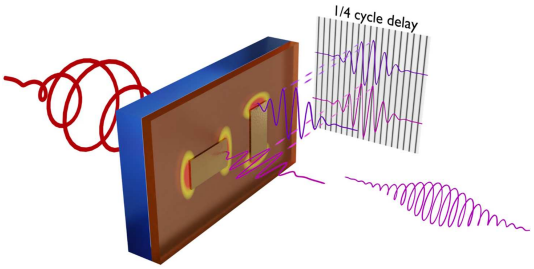

Fig. 1. Concept of the experiment: each antenna resonates for the linear component of the incident circularly polarized driving field that aligns parallel to the antenna's major axis, thereby emitting linearly polarized odd-order high-harmonic radiation with half-cycle multiples of one quarter-cycle delay. Interference of pairs of antennas' emission results in circularly polarized high harmonics upon diffraction. The experiments are performed in reflection; however, transmission geometry is shown for clarity.

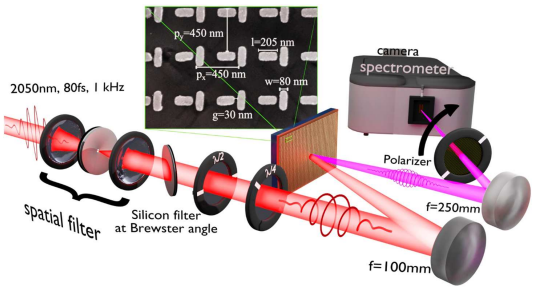

Fig. 2. Experimental setup and scanning electron microscope image (SEM): femtosecond laser pulses with center wavelength of 2050 nm, 80 fs pulse duration at a 1 kHz repetition rate are spatially filtered and focused with a spherical mirror ($f = 100$ mm) on an array of gold antennas fabricated on silicon crystal. A combination of wave plates [half- ($\lambda/2$) and quarter-wave plates ($\lambda/4$)] is utilized to control the laser polarization onto the sample. The polarization of the harmonics generated from the antenna arrays is analyzed using a polarizer suitable for the harmonic wavelengths. High harmonics are collected in reflection geometry and focused with a 250 mm spherical mirror on the slit of the spectrometer (Princeton Instruments Isoplane 320). The inset shows a high-resolution SEM image of perpendicular antennas. The horizontal antenna's major axis is aligned along the [110] direction of the Si crystal. The length, width, gap, pitch, and height of the arrays determine the resonant wavelength.

the polarization, across the metasurface by simply rotating the individual nanoscale elements [36].

Here we merge the metasurface approach with non-perturbative HHG. Inspired by the geometric phase approach, and by the sensitivity of plasmonic rectangular nano-antennas to the orientation of incident linear polarization relative to the antennas' major axes [11], we design a plasmonic metasurface that controls the polarization of emitted HHG in space. Specifically, we generate circularly polarized harmonics by shining a circularly polarized driver on an array of pairs of rectangular antennas fabricated on a Si substrate, with the major axis of each antenna in the pairs aligned perpendicularly to one another. As sketched in Fig. 1, each antenna couples to the component of the driver's electric field that aligns with the antenna's major axis, effectively linearizing the driver's polarization in each antenna's hotspot and resulting in efficient, enhanced, local high-harmonic emission. Crucially, each antenna emission is synchronized with the driving laser but with a relative phase of $n\pi/2$ ("n" is the harmonic order), determined by the relative orientation of the two antennas. The circularly polarized driver guarantees efficient coupling to both antennas. Therefore, overlapping the linear high-harmonic emissions from the two perpendicular antennas in the far-field results in circularly polarized odd-order harmonics. A similar scheme for bow-tie antennas was proposed in [37].

2. HIGH-HARMONIC GENERATION, DETECTION, AND CHARACTERIZATION

The optical setup for generating and detecting high harmonics is shown in Fig. 2. A titanium sapphire femtosecond regenerative amplifier (Coherent Legend) pumps an optical parametric amplifier (OPA TOPAS, Light Conversion) with an energy of 1.3 mJ/pulse. The OPA delivers signal (1.31 μm wavelength) and idler (2.05 μm wavelength) infrared laser pulses of 80 fs duration at 1 kHz repetition rate. The idler beam, with an energy of ∼200 μJ, is spatially filtered with a diamond pinhole of 100 μm diameter, collimated with a CaF_2 lens, and refocused onto the sample with a spherical focusing mirror of 100 mm focal length. The beam waist on the sample is measured with knife-edge method and is found to be comparable to the size of a patterned nano-antenna array (70 μm). We estimate that a total of ∼20,000 antennas are illuminated simultaneously. A silicon filter is used at the Brewster angle to remove any spurious wavelength coming from the OPA. An iris placed before the spatial filter attenuates and controls the average power of the laser system. A zero-order half-wave plate ($\lambda/4$) converts the linear polarization to circular polarization. The angle between the incident beam and sample is kept less than ~ 5 degrees to maximize the resonance.

The sample consists of Au nano-antennas deposited on a single crystal Si film epitaxially grown on a sapphire substrate, R-plane. The inset shows a high-resolution scanning electron image of the rectangular antennas, which are fabricated by electron-beam lithography (see Supplement 1 for details on the fabrication). The nano-antennas are designed to resonate at the laser wavelength (see Supplement 1 for resonance plots and field enhancement), using commercially available finite difference time-domain software from Lumerical. The horizontal nano-antennas are patterned parallel to the [110] direction of the silicon crystal.

The harmonics are measured in reflection to avoid the birefringence of sapphire. The harmonics reflected from the sample are collected and refocused using a spherical mirror (250 mm focal length) onto the slit of a commercial UV-VIS spectrometer (Princeton Instruments Isoplane 320, equipped with a PI-MAX4 ICCD camera). The circularity of the emitted harmonics from antennas and bulk was characterized by rotating an ultra-broadband wire-grid polarizer (250–4000 nm) placed after the sample.

3. RESULTS

Figure 3 shows a comparison between the high-harmonic spectrum produced by nano-antennas and by unpatterned (bulk) Si using circularly polarized (a) and horizontal linearly polarized (b) incident light. The emission extends from the fifth to ninth harmonics

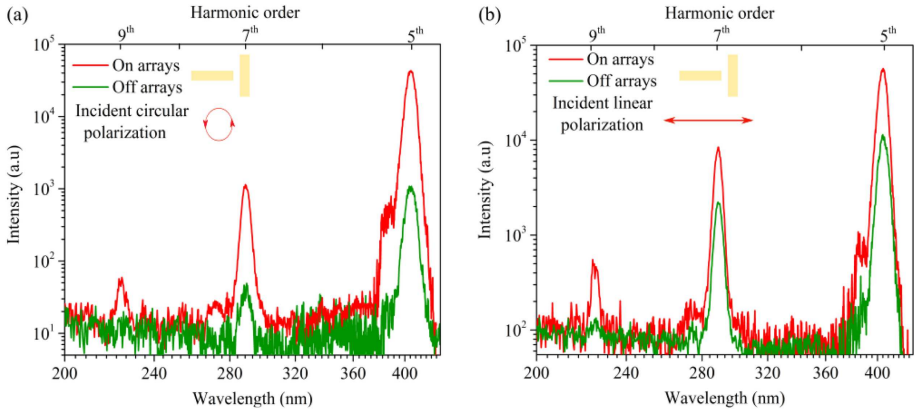

Fig. 3. High-harmonic spectrum with circular and linearly polarized infrared driving field: (a) odd-order high-harmonic generation extending up to the ninth harmonic, when bulk (off arrays, green line) and antennas (on arrays, red line) are driven with a circular polarization at the vacuum intensity of 2.5×10^{10} W cm^{-2}. All the harmonics from arrays are significantly enhanced compared to unpatterned material. (b) A comparison of high-harmonic generation from patterned arrays and unpatterned silicon when the incident polarization is linear and parallel to the major axis of the horizontal antenna (inset). The on/off array contrast is much lower as compared to the circular driving field because bulk emission is significantly suppressed for circular polarization.

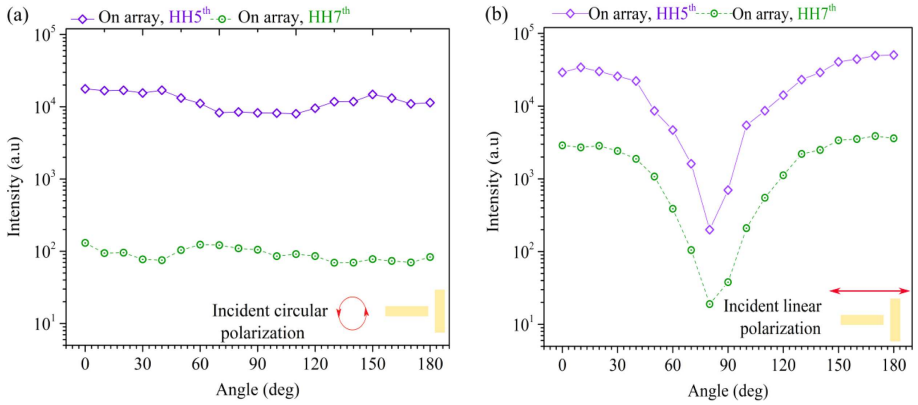

Fig. 4. Polarization analysis of high harmonics illuminated with circularly and linearly polarized infrared driving fields: both panels show harmonic power as a function of the rotation angle of the polarizer. (a) Characterization of harmonics when the array is driven with circular polarization. Fifth and seventh harmonics show little variation, suggesting that the harmonic polarization is circular. (b) Characterization of fifth and seventh harmonics when the array is driven with linear polarization. Harmonic power shows a strong minimum, indicating that the harmonics are linearly polarized.

for an incident intensity (in vacuum) of 2.5×10^{10} W cm^{-2}. The 11th harmonic, at 185 nm, lies beyond the detectable spectral range of our experimental setup. For circular incident polarization, harmonic power from the nano-antennas (red line) is ∼43 and ∼20 times stronger than from unpatterned Si (green line) at the fifth and seventh harmonics, respectively. This large contrast is due primarily to the quenching of bulk emission from Si with circular input polarization, as can be seen comparing the green lines in (a) and (b). It is known that gas-phase high harmonics are suppressed with circular input polarization because electron trajectories miss the parent ion for re-collision [26]. Many solids behave similarly to gases [3]. Emission from the antennas, on the other hand, remains strong, largely irrespective of the input polarization. This suggests that the polarization inside the plasmonic hotspot is linearized, which keeps high-harmonic emission active. Enhancement from the array using linearly polarized light is 20%–30% weaker than we measured previously [11], largely because of the wider unit cell. Fabrication imperfections may also contribute to the difference.

To confirm that the nano-antennas generate circularly polarized high harmonics in the far field, we analyze their polarization state with a polarizer placed after the sample. Figure 4(a) shows the harmonic power from the nano-antenna arrays, as a function of the polarizer rotation angle, when the polarization of the driving field is kept circular. Clearly, the fifth and seventh harmonics appear to be circularly polarized. On the contrary, when the polarization of the driver is linear and horizontal [Fig. 4(b)], the harmonics show a strong minimum for vertical polarization, indicating that they are horizontally linearly polarized, like the driver. This also confirms that the harmonics have a defined polarization (i.e., they are not unpolarized). Further proof that the harmonics are polarized is shown in Supplement 1 (for the fifth harmonic).

4. DISCUSSION

In conclusion, we demonstrated a plasmonic metasurface that emits circularly polarized high harmonics by exploiting the relative delay between the resonance of two perpendicularly aligned rectangular nano-antennas and the selective enhancement of specific driver polarization states. Adding phase and polarization control to high-harmonic emission from nanostructured surfaces completes previous demonstrations of field-enhanced high-harmonic emission from sub-wavelength nano-structures with the addition of the temporal aspect that is so crucial to all attosecond and high-field phenomena.

Control of the polarization occurs *in situ*, while the high harmonics are being generated, without requiring external optical elements, whose dispersion is a hurdle to the synthesis of femtosecond deep-UV pulses, or tailored light fields. This advantage becomes paramount at even shorter wavelengths, such as for XUV harmonics that can be generated from dielectric crystals, where polarization optics perform poorly or are nonexistent altogether. With the recent demonstration of high-harmonic emission from ceramic plasmonic metals at laser intensities comparable to the damage threshold of dielectrics [7], we foresee the integration of plasmonic metasurfaces on dielectric substrates, for the generation and control, in both amplitude and polarization, of XUV harmonics, and even their extension to frequency combs for ever more precise metrology.

Finally, our metasurface approach provides the opportunity to integrate other functionalities, such as *in situ* focusing of the circularly polarized harmonics [38], and structuring of the polarization in space. With such control in a small-scale deep-UV focus, one can envision revealing magnetic and chiral anisotropy on chemisorbed molecules for catalysis and other energy technologies, where specific chemical bonds can be accessed with deep- and vacuum-UV harmonics.

Funding. SiEPIC Fab; Advanced Nanofab Facility of the Stewart Blusson Quantum Matter Institute, University of British Columbia; Joint Center for Extreme Photonics.

Acknowledgment. The authors thank David Crane and Ryan Kroeker for providing continuing technical support. G. Vampa and S.A. Jalil acknowledge financial support from the Joint Centre for Extreme Photonics. K.M. Awan acknowledges the support of the Advanced Nanofab Facility of the Stewart Blusson Quantum Matter Institute and SiEPIC Fab for fabrication of the plasmonic array sample.

G.V. conceived the experiments, S.A.J., I.A.A., and J.B. performed the simulations, and K.M.A. and S.R. fabricated the sample. G.V., A.K., and G.E. assisted in building the setup and optical measurements, S.A.J. and I.A.A. performed the optical measurements, and S.A.J., G.V., and I.A. analyzed the data. G.V., D.M.V., A.S., A.N., L.R., and P.B. supervised the project, and all authors contributed to the paper.

Disclosures. The authors declare no conflicts of interest.

Data availability. Data underlying the results presented in this paper are not publicly available at this time but may be obtained from the authors upon reasonable request.

Supplemental document. See Supplement 1 for supporting content.

REFERENCES

1. M. Ferray, A. L'Huillier, X. Li, L. Lompre, G. Mainfray, and C. Manus, "Multiple-harmonic conversion of 1064 nm radiation in rare gases," J. Phys. B **21**, L31–L35 (1988).
2. T. T. Luu, Z. Yin, A. Jain, T. Gaumnitz, Y. Pertot, J. Ma, and H. J. Wörner, "Extreme–ultraviolet high–harmonic generation in liquids," Nat. Commun. **9**, 3723 (2018).
3. S. Ghimire, A. D. DiChiara, E. Sistrunk, P. Agostini, L. F. DiMauro, and D. A. Reis, "Observation of high-order harmonic generation in a bulk crystal," Nat. Phys. **7**, 138–141 (2011).
4. T. T. Luu, M. Garg, S. Y. Kruchinin, A. Moulet, M. T. Hassan, and E. Goulielmakis, "Extreme ultraviolet high-harmonic spectroscopy of solids," Nature **521**, 498–502 (2015).
5. Y. S. You, D. A. Reis, and S. Ghimire, "Anisotropic high-harmonic generation in bulk crystals," Nat. Phys. **13**, 345–349 (2017).
6. M. Hohenleutner, F. Langer, O. Schubert, M. Knorr, U. Huttner, S. W. Koch, M. Kira, and R. Huber, "Real-time observation of interfering crystal electrons in high-harmonic generation," Nature **523**, 572–575 (2015).
7. A. Korobenko, S. Saha, A. T. Godfrey, M. Gertsvolf, A. Y. Naumov, D. M. Villeneuve, A. Boltasseva, V. M. Shalaev, and P. B. Corkum, "High-harmonic generation in metallic titanium nitride," Nat. Commun. **12**, 4981 (2021).
8. H. Liu, Y. Li, Y. S. You, S. Ghimire, T. F. Heinz, and D. A. Reis, "High-harmonic generation from an atomically thin semiconductor," Nat. Phys. **13**, 262–265 (2017).
9. S. Han, H. Kim, Y. W. Kim, Y.-J. Kim, S. Kim, I.-Y. Park, and S.-W. Kim, "High-harmonic generation by field enhanced femtosecond pulses in metal-sapphire nanostructure," Nat. Commun. **7**, 13105 (2016).
10. M. Sivis, M. Taucer, G. Vampa, K. Johnston, A. Staudte, A. Y. Naumov, D. Villeneuve, C. Ropers, and P. Corkum, "Tailored semiconductors for high-harmonic optoelectronics," Science **357**, 303–306 (2017).
11. G. Vampa, B. Ghamsari, S. Mousavi Siadat, T. Hammond, A. Olivieri, E. Lisicka-Skrek, A. Y. Naumov, D. Villeneuve, A. Staudte, and P. Berini, "Plasmon-enhanced high-harmonic generation from silicon," Nat. Phys. **13**, 659–662 (2017).
12. H. Liu, C. Guo, G. Vampa, J. L. Zhang, T. Sarmiento, M. Xiao, P. H. Bucksbaum, J. Vučković, S. Fan, and D. A. Reis, "Enhanced high-harmonic generation from an all-dielectric metasurface," Nat. Phys. **14**, 1006–1010 (2018).
13. Y. Yang, J. Lu, A. Manjavacas, T. S. Luk, H. Liu, K. Kelley, J.-P. Maria, E. L. Runnerstrom, M. B. Sinclair, and S. Ghimire, "High-harmonic generation from an epsilon-near-zero material," Nat. Phys. **15**, 1022–1026 (2019).
14. H. Liu, G. Vampa, J. L. Zhang, Y. Shi, S. Buddhiraju, S. Fan, J. Vuckovic, P. H. Bucksbaum, and D. A. Reis, "Beating absorption in solid-state high harmonics," Commun. Phys. **3**, 1–6 (2020).
15. M. R. Shcherbakov, H. Zhang, M. Tripepi, G. Sartorello, N. Talisa, A. AlShafey, Z. Fan, J. Twardowski, L. A. Krivitsky, and A. I. Kuznetsov, "Generation of even and odd high harmonics in resonant metasurfaces using single and multiple ultra-intense laser pulses," Nat. Commun. **12**, 4185 (2021).
16. G. Zograf, K. Koshelev, A. Zalogina, V. Korolev, R. Hollinger, D.-Y. Choi, M. Zuerch, C. Spielmann, B. Luther-Davies, and D. Kartashov, "High-harmonic generation from resonant dielectric metasurfaces empowered by bound states in the continuum," ACS Photon. **9**, 567–574 (2022).
17. D. Gauthier, S. Kaassamani, D. Franz, R. Nicolas, J.-T. Gomes, L. Lavoute, D. Gaponov, S. Février, G. Jargot, and M. Hanna, "Orbital angular momentum from semiconductor high-order harmonics," Opt. Lett. **44**, 546–549 (2019).
18. A. Korobenko, S. Rashid, C. Heide, A. Y. Naumov, D. Reis, P. Berini, P. Corkum, and G. Vampa, "Generation of structured coherent extreme ultraviolet beams from an MgO crystal," Opt. Express **29**, 24161–24168 (2021).
19. N. Yu, P. Genevet, M. A. Kats, F. Aieta, J.-P. Tetienne, F. Capasso, and Z. Gaburro, "Light propagation with phase discontinuities: generalized laws of reflection and refraction," Science **334**, 333–337 (2011).
20. X. Ni, N. K. Emani, A. V. Kildishev, A. Boltasseva, and V. M. Shalaev, "Broadband light bending with plasmonic nanoantennas," Science **335**, 427 (2012).
21. N. Yu and F. Capasso, "Flat optics with designer metasurfaces," Nat. Mater. **13**, 139–150 (2014).
22. J. Stöhr, Y. Wu, B. Hermsmeier, M. Samant, G. Harp, S. Koranda, D. Dunham, and B. Tonner, "Element-specific magnetic microscopy with circularly polarized x-rays," Science **259**, 658–661 (1993).
23. S. Zayko, O. Kfir, M. Heigl, M. Lohmann, M. Sivis, M. Albrecht, and C. Ropers, "Ultrafast high-harmonic nanoscopy of magnetization dynamics," Nat. Commun. **12**, 6337 (2021).
24. N. Böwering, T. Lischke, B. Schmidtke, N. Müller, T. Khalil, and U. Heinzmann, "Asymmetry in photoelectron emission from chiral molecules induced by circularly polarized light," Phys. Rev. Lett. **86**, 1187–1190 (2001).

25. T. Heinrich, M. Taucer, O. Kfir, P. Corkum, A. Staudte, C. Ropers, and M. Sivis, "Chiral high-harmonic generation and spectroscopy on solid surfaces using polarization-tailored strong fields," Nat. Commun. **12**, 3723 (2021).
26. K. Budil, P. Salières, A. L'Huillier, T. Ditmire, and M. Perry, "Influence of ellipticity on harmonic generation," Phys. Rev. A **48**, R3437–R3440 (1993).
27. D. B. Milošević, W. Becker, and R. Kopold, "Generation of circularly polarized high-order harmonics by two-color coplanar field mixing," Phys. Rev. A **61**, 063403 (2000).
28. O. Kfir, P. Grychtol, E. Turgut, R. Knut, D. Zusin, D. Popmintchev, T. Popmintchev, H. Nembach, J. M. Shaw, and A. Fleischer, "Generation of bright phase-matched circularly-polarized extreme ultraviolet high harmonics," Nat. Photonics **9**, 99–105 (2015).
29. D. D. Hickstein, F. J. Dollar, P. Grychtol, J. L. Ellis, R. Knut, C. Hernández-García, D. Zusin, C. Gentry, J. M. Shaw, and T. Fan, "Non-collinear generation of angularly isolated circularly polarized high harmonics," Nat. Photonics **9**, 743–750 (2015).
30. L. Hareli, G. Lerner, O. Cohen, and A. Bahabad, "Circularly polarized high harmonic generation through virtual circular birefringence," Appl. Phys. Lett. **118**, 221106 (2021).
31. D. Baykusheva, A. Chacón, J. Lu, T. P. Bailey, J. A. Sobota, H. Soifer, P. S. Kirchmann, C. Rotundu, C. Uher, and T. F. Heinz, "All-optical probe of three-dimensional topological insulators based on high-harmonic generation by circularly polarized laser fields," Nano Lett. **21**, 8970–8978 (2021).
32. M. Tymchenko, J. S. Gomez-Diaz, J. Lee, N. Nookala, M. A. Belkin, and A. Alù, "Gradient nonlinear Pancharatnam-Berry metasurfaces," Phys. Rev. Lett. **115**, 207403 (2015).
33. G. Li, S. Chen, N. Pholchai, B. Reineke, P. W. H. Wong, E. Y. B. Pun, K. W. Cheah, T. Zentgraf, and S. Zhang, "Continuous control of the nonlinearity phase for harmonic generations," Nat. Mater. **14**, 607–612 (2015).
34. R. Camacho-Morales, M. Rahmani, S. Kruk, L. Wang, L. Xu, D. A. Smirnova, A. S. Solntsev, A. Miroshnichenko, H. H. Tan, and F. Karouta, "Nonlinear generation of vector beams from AlGaAs nanoantennas," Nano Lett. **16**, 7191–7197 (2016).
35. G. Li, S. Zhang, and T. Zentgraf, "Nonlinear photonic metasurfaces," Nat. Rev. Mater. **2**, 17010 (2017).
36. A. Karnieli, Y. Li, and A. Arie, "The geometric phase in nonlinear frequency conversion," Front. Phys. **17**, 1–31 (2022).
37. A. Husakou, F. Kelkensberg, J. Herrmann, and M. Vrakking, "Polarization gating and circularly-polarized high harmonic generation using plasmonic enhancement in metal nanostructures," Opt. Express **19**, 25346–25354 (2011).
38. N. Segal, S. Keren-Zur, N. Hendler, and T. Ellenbogen, "Controlling light with metamaterial-based nonlinear photonic crystals," Nat. Photonics **9**, 180–184 (2015).

Part IV

CONCLUSION

CHAPTER 7 CONCLUSION

In this thesis, I presented a novel perspective for analyzing high harmonic generation (HHG) in solids. While not intended to replace existing models, this perspective offers new insights and, in some cases, offers a fresh lens through which to view previously established models. Such a new viewpoint often leads to innovative intuitions and understandings.

My first task was to rigorously define the separation of intraband and interband currents for both common gauges used in expressing electromagnetic potential. Throughout this thesis, I consistently used the length gauge to eliminate confusion. The choice of a rigorously defined gauge, particularly a structural gauge, proved crucial for the subsequent introduction of Wannier states.

The introduction of Wannier states, Fourier transforms of Bloch states, proved pivotal. Just as phase-locking is essential in ultrashort pulse generation to align multiple frequency components, careful consideration of the phase of each Bloch state is crucial for generating well-localized Wannier states. Although multiple bands can be incorporated into Wannier states, I predominantly adhered to a single-band approach to maintain a clear parallel with the Bloch model. The ease with which Bloch quantities, such as the dipole, can be reexpressed in a Wannier basis further underscores the utility of this approach.

The incorporation of these Wannier states led to a reevaluation of harmonic integrals, revealing new saddle points. These saddle points, while reminiscent of those identified by the Bloch model, now account for spatial separation between electrons and holes at both ionization and recombination stages. This extension yielded a semi-classical model that not only provides qualitative insights but also quantitative predictions. The Wannier-Stark ladder emerged as a vital concept, shedding light on lateral ionization and recombination processes. A lateral ionization can be understood as a balance between bandgap reduction and dipole amplitude diminishment, while lateral recombination invokes the Wannier-Stark ladder to introduce additional energy quanta beyond the simple bandgap difference, contributing to high-energy harmonics.

Finally, the experimental demonstrations highlighted the necessity of a real-space perspective in understanding HHG in solids. The unique characteristics of materials or devices, such as ReS_2 with its low symmetry and nanoantennas altering the electric field spatially, were best elucidated through this lens.

CHAPTER 8 Limitations and Future Research

While the model has shown remarkable success in uncovering new insights into HHG in solids, it relies on certain assumptions and approximations that impose limitations. Specifically, the model is best suited for semiconductors with wider band widths compared to bandgaps. It does not accurately account for situations involving elliptically polarized lasers [16, 25, 61], where the electron's initial velocity is crucial. Additionally, the spectral integrals were not mathematically solved rigorously, and certain parameters like the initial crystal momentum and return time were assumed real. This assumption implies that the electron is always born with zero velocity, limiting its applicability.

The incorporation of fully complex saddle points, which would allow for the inclusion of initial electron velocities, could potentially provide a more accurate prediction of the harmonic spectrum's phase and allow for verification through experimental spectrograms in a $\omega - 2\omega$ setup [60].

Another important next step would be the expansion to higher spatial dimensions. The biggest changes are to be expected from going to 1D to 2D compared to 2D to 3D. In 2D, the wavepackets can start expanding in direction perpendicular to the laser field. As a first trivial prediction, we can expect that long trajectories will have a weaker recombination overlap and T_2 should take value closer to experimental value. A big differences with gas HHG, will be the possibility for the hole to also diffuse

in the perpendicular direction. I do not expect perpendicular ionization to the laser field to contribute significantly to the harmonic spectrum as there is a dot product between the field and the dipole at the ionization step, as well as the effect of the Wannier-Starck ladder being not present perpendicularly. At recombination, the perpendicular motion is possible but there I suspect that the electron-hole overlap would favor same site recombination. This would obviously be different for slightly eliptical field or for material with Berry connection (it introduces a perpendicular motion to the field, ie. a permanent dipole).

Another theoretical development that would be very helpful is the ability to evaluate the dipole across all $\mathbf{k}$ from the bandstructure. We saw in chapter 4 that a 2-band calculation in the length gauge needs the two band structure and the dipole between them over all $\mathbf{k}$ while a velocity gauge calculation only needs the energy difference between a lot more bands at $\mathbf{k_0}$ only and their momentum transition element. If that $\mathbf{k_0}$ is a high symmetry point then it can be evaluated easily from the curvature of the band with $\mathbf{k} \cdot \mathbf{p}$ perturbation. In other words, a velocity gauge calculation could only need the bandstructure which is an information more reliably available in the literature than the dipole or the momentum transition element. Since, velocity and length gauge calculation gives equivalent results to a TDSE for observable like harmonic spectrum, one should be able to construct the magnitude of the dipole from just the band structure.

As the field of HHG in solids continues to advance, the need for ac-

curate models becomes paramount. Over the past decade, HHG in solids has become prominent tool to probe for ultrafast phenomena in solids as the understanding HHG is the understanding the ultrafast motion of electrons and holes in a nondestructive way. More accurate models are necessary to push our control of natural processes on such ultrafast timescales for signal processing [5, 6], electronic transport, topological [62, 63] or strongly correlated materials [64, 65], *etc.* These models will need to predict accurately the behaviour of the electrons both in position and momentum space as engineering of these applications will most likely depart from the uniform infinite crystal approximation.

REFERENCES

[1] T. Hahn and J. A. Aragón-Correa, "Toward cognitive plurality on corporate sustainability in organizations: The role of organizational factors," *Organization & Environment*, vol. 28, no. 3, pp. 255–263, 2015.

[2] A. H. Zewail, "Femtochemistry: Atomic-scale dynamics of the chemical bond," *The Journal of Physical Chemistry A*, vol. 104, no. 24, pp. 5660–5694, 2000.

[3] C. V. Shank, "Investigation of ultrafast phenomena in the femtosecond time domain," *Science*, vol. 233, no. 4770, pp. 1276–1280, 1986.

[4] J.-C. Diels and W. Rudolph, *Ultrashort laser pulse phenomena*. Elsevier, 2006.

[5] M. Schultze, E. M. Bothschafter, A. Sommer, S. Holzner, W. Schweinberger, M. Fiess, M. Hofstetter, R. Kienberger, V. Apalkov, V. S. Yakovlev, M. I. Stockman, and F. Krausz, "Controlling dielectrics with the electric field of light," *Nature*, vol. 493, no. 7430, pp. 75–78, 2013.

[6] A. Sommer, E. M. Bothschafter, S. A. Sato, C. Jakubeit, T. Latka, O. Razskazovskaya, H. Fattahi, M. Jobst, W. Schweinberger, V. Shirvanyan, V. S. Yakovlev, R. Kienberger, K. Yabana, M. Schultze, and F. Krausz, "Attosecond real time observation of

the nonlinear polarization and energy transfer in dielectrics," *Nature*, vol. 534, no. 7605, pp. 86–90, 2016.

[7] N. Dudovich, O. Smirnova, J. Levesque, Y. Mairesse, M. Y. Ivanov, D. Villeneuve, and P. B. Corkum, "Measuring and controlling the birth of attosecond xuv pulses," *Nature physics*, vol. 2, no. 11, p. 781, 2006.

[8] P. á. Corkum and F. Krausz, "Attosecond science," *Nature physics*, vol. 3, no. 6, pp. 381–387, 2007.

[9] M. Hentschel, R. Kienberger, C. Spielmann, G. A. Reider, N. Milosevic, T. Brabec, P. Corkum, U. Heinzmann, M. Drescher, and F. Krausz, "Attosecond metrology," *Nature*, vol. 414, no. 6863, pp. 509–513, 2001.

[10] P. B. Corkum, "Plasma perspective on strong field multiphoton ionization," *Physical review letters*, vol. 71, no. 13, p. 1994, 1993.

[11] H. J. Wörner, J. B. Bertrand, D. V. Kartashov, P. B. Corkum, and D. M. Villeneuve, "Following a chemical reaction using high-harmonic interferometry," *Nature*, vol. 466, no. 7306, pp. 604–607, 2010.

[12] W. Li, X. Zhou, R. Lock, S. Patchkovskii, A. Stolow, H. C. Kapteyn, and M. M. Murnane, "Time-resolved dynamics in n2o4 probed using high harmonic generation," *Science*, vol. 322, no. 5905, pp. 1207–1211, 2008.

[13] B. K. McFarland, J. P. Farrell, P. H. Bucksbaum, and M. Guhr, "High harmonic generation from multiple orbitals in n2," *Science*, vol. 322, no. 5905, pp. 1232–1235, 2008.

[14] O. Smirnova, Y. Mairesse, S. Patchkovskii, N. Dudovich, D. Villeneuve, P. Corkum, and M. Y. Ivanov, "High harmonic interferometry of multi-electron dynamics in molecules," *Nature*, vol. 460, no. 7258, pp. 972–977, 2009.

[15] J. Itatani, J. Levesque, D. Zeidler, H. Niikura, H. Pépin, J.-C. Kieffer, P. B. Corkum, and D. M. Villeneuve, "Tomographic imaging of molecular orbitals," *Nature*, vol. 432, no. 7019, p. 867, 2004.

[16] S. Ghimire, A. D. DiChiara, E. Sistrunk, P. Agostini, L. F. DiMauro, and D. A. Reis, "Observation of high-order harmonic generation in a bulk crystal," *Nature Physics*, vol. 7, p. 138, 2011.

[17] O. Schubert, M. Hohenleutner, F. Langer, B. Urbanek, C. Lange, U. Huttner, D. Golde, T. Meier, M. Kira, S. W. Koch, and R. Huber, "Sub-cycle control of terahertz high-harmonic generation by dynamical Bloch oscillations," *Nature Photonics*, vol. 8, no. 2, pp. 119–123, 2014.

[18] T. T. Luu, M. Garg, S. Y. Kruchinin, A. Moulet, M. T. Hassan, and E. Goulielmakis, "Extreme ultraviolet high-harmonic spectroscopy of solids." *Nature*, vol. 521, no. 7553, pp. 498–502, 2015.

[19] F. Langer, M. Hohenleutner, C. P. Schmid, C. Poellmann, P. Nagler, T. Korn, C. Schüller, M. S. Sherwin, U. Huttner, J. T. Steiner,

S. W. Koch, M. Kira, and R. Huber, "Lightwave-driven quasiparticle collisions on a subcycle timescale," *Nature*, vol. 533, no. 7602, pp. 225–229, 2016.

[20] M. Hohenleutner, F. Langer, O. Schubert, M. Knorr, U. Huttner, S. W. Koch, M. Kira, and R. Huber, "Real-time observation of interfering crystal electrons in high-harmonic generation." *Nature*, 2015.

[21] G. Vampa, T. J. Hammond, N. Thiré, B. E. Schmidt, F. Légaré, C. R. McDonald, T. Brabec, D. D. Klug, and P. B. Corkum, "All-Optical Reconstruction of Crystal Band Structure," *Physical Review Letters*, vol. 115, no. 19, pp. 1–5, 2015.

[22] A. A. Lanin, E. A. Stepanov, A. B. Fedotov, and A. M. Zheltikov, "Mapping the electron band structure by intraband high-harmonic generation in solids," *Optica*, vol. 4, no. 5, p. 516, 2017.

[23] T. T. Luu and H. J. Wörner, "Measurement of the Berry curvature of solids using high-harmonic spectroscopy," *Nature Communications*, vol. 9, no. 1, p. 916, 2018.

[24] E. N. Osika, A. Chacón, L. Ortmann, N. Suárez, J. A. Pérez-Hernández, B. Szafran, M. F. Ciappina, F. Sols, A. S. Landsman, and M. Lewenstein, "Wannier-bloch approach to localization in high-harmonics generation in solids," *Physical Review X*, vol. 7, no. 2, pp. 1–14, 2017.

[25] N. Tancogne-Dejean, O. D. Mücke, F. X. Kärtner, and A. Rubio, "Ellipticity dependence of high-harmonic generation in solids orig-

inating from coupled intraband and interband dynamics," *Nature communications*, vol. 8, no. 1, p. 745, 2017.

[26] G. Vampa, C. R. McDonald, G. Orlando, P. B. Corkum, and T. Brabec, "Semiclassical analysis of high harmonic generation in bulk crystals," *Physical Review B*, vol. 91, no. 6, p. 064302, 2015.

[27] M. Wu, S. Ghimire, D. A. Reis, K. J. Schafer, and M. B. Gaarde, "High-harmonic generation from bloch electrons in solids," *Physical Review A*, vol. 91, no. 4, p. 043839, 2015.

[28] M. Wu, D. A. Browne, K. J. Schafer, and M. B. Gaarde, "Multilevel perspective on high-order harmonic generation in solids," *Physical Review A*, vol. 94, no. 6, p. 063403, 2016.

[29] S. Jiang, J. Chen, H. Wei, C. Yu, R. Lu, and C. Lin, "Role of the transition dipole amplitude and phase on the generation of odd and even high-order harmonics in crystals," *Physical review letters*, vol. 120, no. 25, p. 253201, 2018.

[30] L. Li, P. Lan, X. Zhu, T. Huang, Q. Zhang, M. Lein, and P. Lu, "Reciprocal-space-trajectory perspective on high-harmonic generation in solids," *Physical review letters*, vol. 122, no. 19, p. 193901, 2019.

[31] L. Yue and M. B. Gaarde, "Introduction to theory of high-harmonic generation in solids: tutorial," *JOSA B*, vol. 39, no. 2, pp. 535–555, 2022.

[32] G. Vampa, B. Ghamsari, S. Siadat Mousavi, T. Hammond, A. Olivieri, E. Lisicka-Skrek, A. Y. Naumov, D. Villeneuve, A. Staudte, P. Berini *et al.*, "Plasmon-enhanced high-harmonic generation from silicon," *Nature Physics*, vol. 13, no. 7, pp. 659–662, 2017.

[33] M. Sivis, M. Duwe, B. Abel, and C. Ropers, "Extreme-ultraviolet light generation in plasmonic nanostructures," *Nature Physics*, vol. 9, no. 5, pp. 304–309, 2013.

[34] S. A. Jalil, K. M. Awan, I. A. Ali, S. Rashid, J. Baxter, A. Korobenko, G. Ernotte, A. Naumov, D. M. Villeneuve, A. Staudte *et al.*, "Controlling the polarization and phase of high-order harmonics with a plasmonic metasurface," *Optica*, vol. 9, no. 9, pp. 987–991, 2022.

[35] Z.-Y. Chen and R. Qin, "High harmonic generation in graphene–boron nitride heterostructures," *Journal of Materials Chemistry C*, vol. 8, no. 35, pp. 12 085–12 091, 2020.

[36] M. Sivis, M. Taucer, K. Johnston, G. Vampa, A. Staudte, A. Naumov, D. Villeneuve, C. Ropers, and P. Corkum, "Localized high harmonic generation in semiconductor nanostructures," *Optics InfoBase Conference Papers*, p. 10, 2014.

[37] C. Yu, K. K. Hansen, and L. B. Madsen, "Enhanced high-order harmonic generation in donor-doped band-gap materials," *Physical Review A*, vol. 99, no. 1, p. 013435, 2019.

[38] O. Richardson and K. T. Compton, "The photoelectric effect," *Science*, vol. 35, no. 907, pp. 783–784, 1912.

[39] M. Göppert-Mayer, "Über elementarakte mit zwei quantensprüngen," *Annalen der Physik*, vol. 401, no. 3, pp. 273–294, 1931.

[40] G. S. He, L.-S. Tan, Q. Zheng, and P. N. Prasad, "Multiphoton absorbing materials: molecular designs, characterizations, and applications," *Chemical reviews*, vol. 108, no. 4, pp. 1245–1330, 2008.

[41] L. V. Keldysh, "Ionization in the field of a strong electromagnetic wave," *Zh. Eksperim. i Teor. Fiz.*, vol. 47, 1964.

[42] M. W. Walser, C. H. Keitel, A. Scrinzi, and T. Brabec, "High harmonic generation beyond the electric dipole approximation," *Physical Review Letters*, vol. 85, no. 24, p. 5082, 2000.

[43] D. M. Wolkow, "Über eine klasse von lösungen der diracschen gleichung," *Zeitschrift für Physik*, vol. 94, pp. 250–260, 1935. [Online]. Available: https://api.semanticscholar.org/CorpusID:123046147

[44] M. Lewenstein, P. Balcou, M. Y. Ivanov, A. L'huillier, and P. B. Corkum, "Theory of high-harmonic generation by low-frequency laser fields," *Physical Review A*, vol. 49, no. 3, p. 2117, 1994.

[45] M. Lewenstein, P. Salieres, and A. L'huillier, "Phase of the atomic polarization in high-order harmonic generation," *Physical Review A*, vol. 52, no. 6, p. 4747, 1995.

[46] K. Amini, J. Biegert, F. Calegari, A. Chacón, M. F. Ciappina, A. Dauphin, D. K. Efimov, C. F. de Morisson Faria, K. Giergiel, P. Gniewek *et al.*, "Symphony on strong field approximation," *Reports on Progress in Physics*, vol. 82, no. 11, p. 116001, 2019.

[47] S. Popruzhenko and D. Bauer, "Strong field approximation for systems with coulomb interaction," *Journal of Modern Optics*, vol. 55, no. 16, pp. 2573–2589, 2008.

[48] F. Bloch, "Über die quantenmechanik der elektronen in kristallgittern," *Zeitschrift für physik*, vol. 52, no. 7-8, pp. 555–600, 1929.

[49] P. Ehrenfest, "Bemerkung über die angenäherte gültigkeit der klassischen mechanik innerhalb der quantenmechanik," *Zeitschrift für physik*, vol. 45, no. 7-8, pp. 455–457, 1927.

[50] E. Noether, "Invariant variation problems," *Transport theory and statistical physics*, vol. 1, no. 3, pp. 186–207, 1971.

[51] E. Blount, "Formalisms of band theory," in *Solid state physics*. Elsevier, 1962, vol. 13, pp. 305–373.

[52] I. Floss, C. Lemell, G. Wachter, V. Smejkal, S. A. Sato, X.-M. Tong, K. Yabana, and J. Burgdörfer, "Ab initio multiscale simulation of high-order harmonic generation in solids," *Phys. Rev. A*, vol. 97, p. 011401, Jan 2018.

[53] G. Vampa, T. J. Hammond, N. Thire, B. E. Schmidt, F. Legare, C. R. McDonald, T. Brabec, and P. B. Corkum, "Linking high har-

monics from gases and solids," *Nature*, vol. 522, no. 7557, pp. 462–464, 2015.

[54] P. Földi, "Gauge invariance and interpretation of interband and intraband processes in high-order harmonic generation from bulk solids," *Physical Review B*, vol. 96, no. 3, p. 035112, 2017.

[55] G. H. Wannier, "The Structure of Electronic Excitation Levels in Insulating Crystals," *Physical Review*, vol. 52, p. 191, 1937.

[56] L. Yue and M. B. Gaarde, "Structure gauges and laser gauges for the semiconductor bloch equations in high-order harmonic generation in solids," *Physical Review A*, vol. 101, no. 5, p. 053411, 2020.

[57] N. Marzari, I. Souza, and D. Vanderbilt, "An Introduction to Maximally-Localized Wannier Functions," *Psi-k Newsletter*, vol. 57, 2003.

[58] N. Marzari, A. A. Mostofi, J. R. Yates, I. Souza, and D. Vanderbilt, "Maximally localized Wannier functions: Theory and applications," *Reviews of Modern Physics*, vol. 84, no. 4, pp. 1419–1475, 2012.

[59] L. Yue and M. B. Gaarde, "Imperfect recollisions in high-harmonic generation in solids," *Physical Review Letters*, vol. 124, no. 15, p. 153204, 2020.

[60] O. Pedatzur, G. Orenstein, V. Serbinenko, H. Soifer, B. Bruner, A. Uzan, D. Brambila, A. Harvey, L. Torlina, F. Morales *et al.*, "At-

tosecond tunnelling interferometry," *Nature Physics*, vol. 11, no. 10, pp. 815–819, 2015.

[61] L. Yue and M. B. Gaarde, "Expanded view of electron-hole recollisions in solid-state high-order harmonic generation: Full-brillouin-zone tunneling and imperfect recollisions," *Physical Review A*, vol. 103, no. 6, p. 063105, 2021.

[62] D. Bauer and K. K. Hansen, "High-Harmonic Generation in Solids with and without Topological Edge States," *Physical Review Letters*, vol. 120, no. 17, p. 177401, 2018.

[63] R. E. Silva, Jiménez-Galán, B. Amorim, O. Smirnova, and M. Ivanov, "Topological strong-field physics on sub-laser-cycle timescale," *Nature Photonics*, vol. 13, no. December, 2019.

[64] R. Silva, I. V. Blinov, A. N. Rubtsov, O. Smirnova, and M. Ivanov, "High-harmonic spectroscopy of ultrafast many-body dynamics in strongly correlated systems," *Nature Photonics*, vol. 12, no. 5, p. 266, 2018.

[65] Y. Murakami, M. Eckstein, and P. Werner, "High-harmonic generation in mott insulators," *Physical review letters*, vol. 121, no. 5, p. 057405, 2018.

APPENDIX A THE CLASSICAL THREE-STEP MODEL

The three-step recollision model in gases is based on the following assumptions:

1. An electron can be ionized at any time t_i with zero velocity.
2. The electron is accelerated like a free particle after ionization (no Coulomb interaction with the parent ion).
3. Upon returning to the same position as its parent ion at time t_r, the electron can return to its initial energy state. The difference in energy is emitted as a photon.

We will assume that the driving vector field is a sine wave:

$$A(t) = A_0 \sin(\omega_0 t). \tag{A.1}$$

As the electron is born without velocity, the initial momentum of the electron before the laser pulse is $-A(t_i)$, implying that the momentum of the electron in the continuum is given by:

$$p(t) = A(t) - A(t_i). \tag{A.2}$$

The kinetic energy of the electron at recombination is then:

$$K(t_r) = \frac{(A(t_r) - A(t_i))^2}{2}. \tag{A.3}$$

Finally, the condition that the electron returns to its original position can be expressed as:

$$\int_{t_i}^{t_r} p(\tau) d\tau = 0. \tag{A.4}$$

Solving these equations numerically yields the results shown in Fig. A.1 for an arbitrary A_0 and ω:

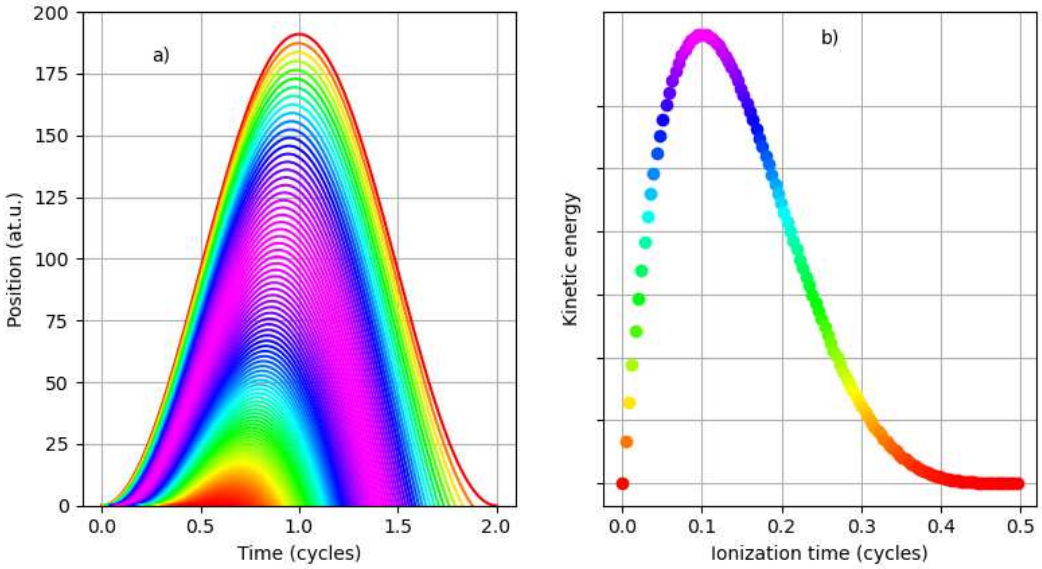

Figure A.1 [Short and long trajectories in HHG in gas]a) Position as a function of time. The color of the line is correlated to the kinetic energy at recombination. Red corresponds to the lowest energy, while purple corresponds to the highest, as shown in b) where kinetic energy is plotted as a function of birth time.

From Fig. A.1 b), we observe that a specific kinetic energy has two possible ionization times. There are two classes of trajectories that lead to the same final energy: short and long trajectories. Typically, in an experiment, only the short trajectories add up coherently to form

a well-collimated beam. The long trajectories tend to diverge more after generation due to the natural expansion of the returning electron wavepacket.

Only the ionization times of the first half-cycle of the vector potential are shown, as the system is symmetric with respect to each half-cycle. This symmetry also implies that only odd harmonics of the driving laser field will add up coherently, while even harmonics will completely interfere destructively.

APPENDIX B SADDLE POINT APPROXIMATION

The saddle point approximation is a mathematical technique used to compute integrals of the form:

$$I = \int_a^b g(z)\, \mathrm{e}^{f(z)} dz, \tag{B.1}$$

where $g(z)$ and $f(z) = u + iv$ are arbitrary complex functions. The imaginary part of $f(z)$ must vary rapidly compared to $g(z)$. When viewed through the lens of a Riemann sum, the integral destructively interferes due to the fast-evolving phase v. The dominant contribution to the integral arises when that phase slows down, i.e., $f'(z) = 0$. Thus, the first step is to identify the point z_0 where the phase becomes stationary. This point is a saddle point because the complex derivative satisfies the Cauchy-Riemann conditions ($z = x + iy$):

$$f'(z) = \frac{du}{dx} - \frac{dv}{dy} + i\frac{du}{dy} + i\frac{dv}{dx} = 0, \tag{B.2}$$

$$\frac{du}{dx} = \frac{dv}{dy} \qquad \frac{du}{dy} = -\frac{dv}{dx}. \tag{B.3}$$

This implies that v and u also satisfy the Laplace equation:

$$\frac{d^2v}{dx^2} + \frac{d^2v}{dy^2} = 0. \tag{B.4}$$

Consequently, $\frac{d^2v}{dx^2}$ and $\frac{d^2v}{dy^2}$ have opposite signs, confirming that z_0 is a saddle point.

The next step involves expanding around the saddle point:

$$f(z) \approx f(z_0) + \frac{1}{2}f''(z_0)(z - z_0)^2. \tag{B.5}$$

Subsequently, the integral can be evaluated using a complex Gaussian integral:

$$I \approx g(z_0)\,\mathrm{e}^{f(z_0)} \int_C \exp\left[\frac{1}{2}f''(z_0)(z - z_0)^2\right] dz, \tag{B.6}$$

where the path C passes through z_0 and ensures that the second derivative of f is negative (which is always possible for a saddle point). The appropriate path C is determined by rewriting the second derivative of f and z as $f''(z_0) = |f''(z_0)|\mathrm{e}^{i\theta}$ and $(z - z_0) = r\mathrm{e}^{i\phi}$. The correct path is achieved when $\phi = (\pi - \theta)/2$.

$$\begin{aligned} I &\approx g(z_0)\,\mathrm{e}^{f(z_0)}\,\mathrm{e}^{i\phi} \int_C \exp\left[-\frac{1}{2}|f''(z_0)|r^2\right] dr \\ &= \sqrt{\frac{2\pi}{|f''(z_0)|}}\, g(z_0)\,\mathrm{e}^{f(z_0)}\,\mathrm{e}^{i\phi}. \end{aligned} \tag{B.7}$$

For integrals with multiple saddle points, the correct approximation in-

volves summing over different saddle points:

$$I \approx \sum_{z_0} \sqrt{\frac{2\pi}{|f''(z_0)|}} g(z_0)\, \mathrm{e}^{f(z_0)}\, \mathrm{e}^{i\phi}. \tag{B.8}$$